Distribution Agreement

In presenting this thesis or dissertation as a partial fulfillment of the requirements for an advanced degree from Emory University, I hereby grant to Emory University and its agents the non-exclusive license to archive, make accessible, and display my thesis or dissertation in whole or in part in all forms of media, now or hereafter known, including display on the world wide web. I understand that I may select some access restrictions as part of the online submission of this thesis or dissertation. I retain all ownership rights to the copyright of the thesis or dissertation. I also retain the right to use in future works (such as articles or books) all or part of this thesis or dissertation.

Signature:

_____   _____

Brent Elliott Allman   Date

Within-host RNA virus evolution in the context of
cellular coinfection and genetic linkage

By

Brent Elliott Allman
Doctor of Philosophy

Population Biology, Ecology, and Evolution

Katia Koelle, Ph.D.
Advisor

Daniel Weissman, Ph.D.
Advisor

Anice Lowen, Ph.D.
Committee Member

Levi Morran, Ph.D.
Committee Member

Timothy Read, Ph.D.
Committee Member

Accepted:

Kimberly Jacob Arriola, Ph.D.
Dean of the James T. Laney School of Graduate Studies

Date

Within-host RNA virus evolution in the context of
cellular coinfection and genetic linkage

By

Brent Elliott Allman
B.A., Mathematics,
University of San Diego, 2015

Advisors: Katia Koelle, Ph.D.
and Daniel Weissman, Ph.D.

An abstract of
A dissertation submitted to the Faculty of the
James T. Laney School of Graduate Studies of Emory University
in partial fulfillment of the requirements for the degree of
Doctor of Philosophy
in Population Biology, Ecology, and Evolution
2022

Abstract

Within-host RNA virus evolution in the context of
cellular coinfection and genetic linkage
By Brent Elliott Allman

RNA viruses pose one of the greatest threats to public health, in part due to their rapid evolutionary patterns. As viruses infect individuals in a population they accrue mutations, some of which confer phenotypes that increase the virulence or transmissibility of the virus. While these phenotypes can have population-level consequences, the evolutionary forces that allow adaptive mutations to reach high frequency largely occur at the level of individual hosts. Further, the dynamics that ensue at the host-level are consequences of processes at the intra- and inter-cellular levels. I explore how the diversity of within-host viral populations is shaped, with particular considerations for cellular coinfection and genetic linkage. When viruses coinfect host cells, different parental genotypes produce protein products by hijacking host cell machinery and these proteins help to produce progeny virions. We ask what happens when proteins with differential fitness effects are treated as public goods. A key assumption of our models is that when coinfection occurs, the fitness of the viral progeny is a result of incomplete dominance from the parental genotypes. This results in fitness that is in between the most- and least-fit parents. We develop models and apply them to data to investigate the evolutionary phenomena that result from these within-host scenarios. Using simulations, we show that coinfection weakens the efficacy of selection, approaching the neutral selection limit. So as rates of coinfection increase, so do rates of deleterious mutation accumulation. We also develop deterministic models of wild-type and mutant virus evolution within-host. We show that a beneficial mutant is fixed less readily when we increase rates of coinfection. We then use Markov chain Monte Carlo to infer the relative fitness of a viral mutation that occurred in an animal model of influenza infection. These contributions are significant because we know that coinfection occurs within-host, and our work shows that models that infer fitness without considering coinfection are likely underestimating the magnitude of fitness coefficients. Our results may help to explain slower fixation of adaptive variants at the epidemiological level. Next, we identify intra-host single nucleotide variants (iSNVs) in immunocompromised patients with chronic SARS-CoV-2 infections. Experimental collaborators show that some of these iSNVs confer immune escape induced by monoclonal antibody treatment. Finally, we investigate interpretations of within-host evolution with data from a focal patient. We show that iSNV data alone can lead to incomplete evolutionary narratives, but additional resolution can be obtained when genetic linkage through haplotype analysis is brought to the fore.

Within-host RNA virus evolution in the context of
cellular coinfection and genetic linkage

By

Brent Elliott Allman
B.A., Mathematics,
University of San Diego, 2015

Advisors: Katia Koelle, Ph.D.
and Daniel Weissman, Ph.D.

A dissertation submitted to the Faculty of the
James T. Laney School of Graduate Studies of Emory University
in partial fulfillment of the requirements for the degree of
Doctor of Philosophy
in Population Biology, Ecology, and Evolution
2022

them my colleague.

I want to thank my PBEE cohort. Coming into graduate school with such a special group of people made me excited to learn and contribute, in part because I admired their skills and contributions. I especially want to thank Connor Morozumi. Connor's friendship was instrumental in getting me through very challenging periods of graduate school. I can confidently say that it was through his presence that I was able to succeed professionally and, more importantly, articulate parts of my self that I didn't have words for or had minimal awareness of.

Last, I want to thank my therapist(s) for helping me to manage my mental health, and leave graduate school with a better understanding of how to maintain a life that I am happy to live in.

The work presented in this dissertation was largely conducted on the land of the Mvskoke (Muscogee) people. Europeans began colonizing their land in the early 1700's; land that would ultimately host hard-fought battles in the Civil War and the Civil Rights Movement.

Foreword

A vignette of identity-informed science
By Brent Elliott Allman

Science should be conducted without regard to identity or personal politics, some might say. The ideal scientific inquiry is unbiased and is independent from the researcher, some might say. Before I began graduate school, I may have agreed with these sentiments. However, after reflecting on my body of work from graduate school, I see how parts of my identity were unconsciously woven into the questions I addressed and the topics I took interest in. Particularly, the majority of my time during the PhD was spent thinking about the unique phenotypes that emerge when different genotypes produce progeny in concert with one another. (Later this is referred to as phenotypic hiding.) These unique phenotypes often do not match the genetic material that they house. I see parallels of my identity in this theme. Being born from parents of different races, I have both a phenotype and genotype that is unique from each of my parents − not squarely black or white. Like my assumptions around progeny that are produced by phenotypic hiding, my the internal locus of my identity isn't necessarily consistent with my (perceived) phenotype.

Whats more, I don't see this realization as a failure to be unbiased, or a failure to remove the personal from the professional. Instead, I see my work as a unique success that was colored by my experiences before and during graduate school. My affinity for the themes of my dissertation may have come from a desire to better understand these experiences and understand my self.

Contents

List of Figures

List of Tables

Chapter 1

Introduction

While RNA viruses are among the smallest biological units, they can have disastrous consequences on individuals, populations, and societies. As agents of infectious diseases, RNA viruses can impair or kill their hosts on large scales during pandemics both historically and presently. The 1918 influenza pandemic likely had its origins in avian and swine host populations, and a decade after the pandemic ended, phylogenetic evidence that the ancestor to the pandemic strain was found to be circulating in avian populations (Reid et al., 2004). Low estimates indicate the pandemic killed approximately 50 million people (Frost, 1920, Johnson and Mueller, 2002). Influenza had its most recent pandemic in 2009, when a virus circulating in birds infected commercial swine and created a genetically distinct reassortant virus that had huge adaptive potential in human hosts (Team, 2009). Most recently, severe acute respiratory syndrome coronavirus-2 (SARS-CoV-2), the virus responsible for COVID-19, has caused the modern ongoing pandemic and has killed over 6.2 million people estimated by the World Health Organization as of June 1, 2022 (World Health Organization, accessed 2022-06-02). The virus has also been shown to circulate in other mammalian hosts (Damas et al., 2020, Wu et al., 2020, Hossain et al., 2021). In order to maintain transmission chains and spread through their host populations, RNA viruses must

evolve to be transmissible among these host populations. In the absence of hosts, viruses cannot evolve, so any adaptation with population-level consequences must first evolve within individual hosts.

RNA viruses have a remarkable capacity to evolve within their hosts through several life-history features. Their high mutation rates on the order of 10^{-6} to 10^{-4} substitutions per nucleotide per replication cycle quickly generate massive amounts of diversity on which the force of natural selection can act (Sanjuán et al., 2010). The vast majority of mutations that are introduced into viral genomes will have deleterious fitness effects (Sanjuán et al., 2004), and negative selection will work to purge these from populations. Rare beneficial mutations will also be introduced into populations, and these will be positively selected for over viral generations.

While positive and negative selection act to shape the diversity of intrahost populations, this diversity is what is transmitted to secondary infections. Although the diversity within a single host may be vast, what becomes transmitted to the next host may not be a representative sample of this variation because of transmission bottlenecks. In the cases of respiratory viruses like IAV and SARS-CoV-2, narrow bottlenecks limit the scope of variation transmitted between hosts, which decreases the efficacy of selection at the between-host level via genetic drift (Ghafari et al., 2020, Popa et al., 2020, Martin and Koelle, 2021). But large changes to individual viral genomes can arise outside the scope of mutation to create the opportunity for adaptation.

In some viruses, recombination during replication allows for the exchange of long segments of genetic code within genomic segments. HIV, norovirus, and SARS-CoV-2 are examples of viruses that undergo this form of exchange. This can produce novel viral strains by introducing many mutations simultaneously onto a genetic backbone. RNA viruses also have genomic diversity, such that some virus genomes are organized in multiple discrete segments of RNA that encode one or more genes. Influenza is one

such virus, and reassortment between distinct lineages of IAV are what produced the pandemic H1N1 strain in 2009 (Smith et al., 2009). Other viruses such as multipartite viruses fail to package all of their gene segments into single viral particles. In order for these viruses to successfully progenerate, the full complement of gene segments must be delivered to their host's site of replication. This may seem disadvantageous, but it also allows for more flexible dosing of individual genes to host cells (Michalakis and Blanc, 2020), creating and additional layer of genetic diversity. To have evolutionary consequences, recombination, reassortment, and complementation all rely on genetically or genomically distinct viral particles coinfecting the same host cell.

To a first approximation, cellular coinfection events may seem rare because the entire host cell population far outnumbers an *in vivo* viral population. However, not all of these cells are available for the virus to infect. Once the first virions successfully infect a host cell, the number of cells that can be infected is limited because the viruses emerging from that host cell are locally dispersed. Spatial structure effectively reduces the host cell population size, driving up viral density and the probability of coinfection events (Gallagher et al., 2018).

As discussed above, the coinfection of genetically distinct viruses can have evolutionary consequences; among these, phenotypic hiding. When viruses infect a cell, they hijack the host cell machinery to produce viral proteins that facilitate the production of new viral genomes and viral particles. What happens when viruses contribute genetic material that encodes proteins with differential fitness? If these proteins are used together, the phenotypes of viral progeny represent contributions from more than one viral parent. These phenotypes may be entirely unique, and the genomes of the viral progeny emerging won't encode the information to reproduce these phenotypes if they were to go on to singly infect host cells. This phenomenon of novel viral phenotypes among discordant viral genotypes is called phenotypic hiding. In two of the following chapters, we explore the evolutionary significance of phenotypic hiding.

In particular, we first use an agent-based model to show that deleterious mutations accumulate more readily when phenotypic hiding is in effect. While this result is not particularly surprising given previous literature showing that natural selection is weakened by phenotypic hiding, we extend these results by incorporating cellular heterogeneity into the model. We do this first by stochastically modifying the contribution that fitness has on a cell's output of virus, and then by modifying the output of a cell in a multiplicity of infection-dependent manner. Each of these forms of stochasticity increase deleterious mutation accumulation. We show that these results are generalizable across fitness functions.

Next, we further model phenotypic hiding by considering the evolution of a single viral variant within a host. We fit our model to empirical data to show that estimates of variant fitness that consider coinfection differ in magnitude from estimates that assume variant fitness is independent of cellular coinfection.

We next move to a more applied setting where we consider the evolution of SARS-CoV-2 within immunocompromised patients. Using samples taken longitudinally from three chronically infected patients, we call intra-host single nucleotide variants (iSNVs). Experiments performed by collaborators show that some of the iSNVs that evolved over the course of the infections conferred immune escape. We further examine the data by determining genetically linked iSNVs, haplotypes, and describing how these data can be more informative than iSNV data alone.

Taken together, the work presented here reiterates the importance of understanding the evolutionary dynamics of viruses within their hosts because the diversity produced and maintained at this level is what gets transmitted to secondary hosts, and begets subsequent epidemics and pandemics.

Chapter 2

Heterogeneity in viral infections increases the rate of deleterious mutation accumulation

Brent Allman[*, 1], Katia Koelle[2], Daniel Weissman[2, 3]

[1,*]Graduate Program in Population Biology, Ecology, and Evolution, Emory University, Atlanta, Georgia 30322

[2]Department of Biology, Emory University, Atlanta, Georgia 30322

[3]Department of Physics, Emory University, Atlanta, Georgia 30322

[*]Corresponding author: Brent Allman. Emory University, Department of Biology, O. Wayne Rollins Research Center, 1510 Clifton Road NE, Atlanta, GA 30322. Phone: (619) 609-4925. Email: allmanbrent@gmail.com

2.1   Abstract

RNA viruses have high mutation rates, with the majority of mutations being deleterious. We examine patterns of deleterious mutation accumulation over multiple rounds of viral replication, with a focus on how cellular coinfection and heterogeneity in viral output affect these patterns. Specifically, using agent-based intercellular simulations we find, in agreement with previous studies, that coinfection of cells by viruses relaxes the strength of purifying selection, and thereby increases the rate of deleterious mutation accumulation. We further find that cellular heterogeneity in viral output exacerbates the rate of deleterious mutation accumulation, regardless of whether this heterogeneity in viral output is stochastic or is due to variation in cellular multiplicity of infection. These results highlight the need to consider the unique life histories of viruses and their population structure to better understand observed patterns of viral evolution.

2.2   Introduction

RNA viruses have high mutation rates and undergo frequent population bottlenecks, making them particularly prone to the accumulation of deleterious mutations. As such, these populations can experience deleterious mutation loads, which is the burden on fitness that recurrent and persistent mutations have on populations (Crow, 1958, Agrawal and Whitlock, 2012). Indeed, the accumulation of deleterious mutations in viruses has been repeatedly demonstrated using experimental evolution. In particular, experiments have demonstrated that serial population bottlenecks impact rates of deleterious mutation accumulation in viral populations (Chao, 1990, Clarke et al., 1993, Escarmís et al., 1996, Elena et al., 1998, Poon and Chao, 2004, García-Arriaza et al., 2005). Drugs that exploit this accumulation by increasing already high mutation rates can drive viral populations extinct (Anderson et al., 2004, Pauly and

Lauring, 2015, Bank et al., 2016). Experimental studies have also shown that cellular coinfection affects the rate of deleterious mutation accumulation in viral populations (Wilke and Novella, 2003a, Novella et al., 2004). In particular, cellular coinfection leads to slower purging of deleterious mutations because selection is relaxed: when multiple viral genomes are present in a cell, they all share their protein products (Zavada, 1976, Froissart et al., 2004). With multiple copies of the same gene that have differential fitness, phenotypes and genotypes of the offspring will not necessarily be matched. Cellular coinfection therefore allows for "phenotypic hiding" of deleterious mutations (Wilke and Novella, 2003a, Novella et al., 2004).

Several processes reduce the accumulation of deleterious mutations in RNA viruses. One such mechanism is through the evolution of higher fidelity polymerase proteins, thus reducing deleterious mutation rates (Pfeiffer and Kirkegaard, 2003, Coffey et al., 2011, Cheung et al., 2014). Recombination (and its segmented analogue, reassortment) also reduces the rate of deleterious mutation accumulation through the generation of high fitness viral genotypes via viral sex. By limiting cellular multiplicity of infection (MOI), superinfection exclusion (Turner et al., 1999, Schaller et al., 2007, Folimonova, 2012) also reduces the opportunity for phenotypic hiding. However, superinfection exclusion also limits the opportunity for viral sex to occur, and thus its net effect on the rate of deleterious mutation accumulation is unknown.

The effect of cellular MOI on the rate of deleterious mutation accumulation is particularly interesting to consider given its uniqueness to viral populations and that cellular coinfection is, in effect, a double-edged sword: providing an opportunity to purge deleterious mutations via viral sex, while relaxing selection on deleterious mutations by increasing the extent of phenotypic hiding. However, when phenotypic hiding dominates, the benefits of coinfection are greatly reduced for viruses that cannot recombine or reassort. Here, we develop a model to examine the effects of cellular coinfection on deleterious mutation accumulation in viral populations in the

context of these opposing effects. We first show that the simplest version of the model recapitulates previous findings in the literature (Wilke and Novella, 2003a, Novella et al., 2004) that indicate cellular coinfection, in the absence of genetic exchange, increases the accumulation of deleterious mutations. We then extend this model to include cellular heterogeneity in viral output, based on experimental findings that demonstrate extreme cellular heterogeneity in response to viral infection (Russell et al., 2018, Martin et al., 2020). We find that heterogeneity, whether due to variation in cellular MOI or intrinsic cellular variation, increases the rate of deleterious mutation accumulation. Our findings highlight how viral life history characteristics can impact deleterious mutation accumulation.

2.3   Model

2.3.1   Base model

We use a generalized Wright-Fisher model of the viral population (Fig. 2.1), with V virions infecting a host cell population of size C. Both V and C remain constant over time, yielding a constant average MOI of V/C. Each virion has g genes in its genome. These genes are distributed across y freely reassorting gene segments, with no recombination within segments. Deleterious mutations occur at a rate of U/g per gene per generation, such that the overall deleterious mutation rate occurs at a rate of U per genome per generation. In simulations of this model, we use $y \in \{1, 2, 4, 8\}$ to capture a range of reassortment potentials, with $y = 8$ reflective of influenza A virus genomes. For simplicity, we use $g = 8$ in all simulations so that genes can be evenly distributed across the considered numbers of segments. Within each gene, we adopt an infinite sites assumption. Thus each genome can be characterized simply by how many deleterious mutations it carries at each of its g genes.

At the beginning of each generation, the V virions are randomly assigned to the
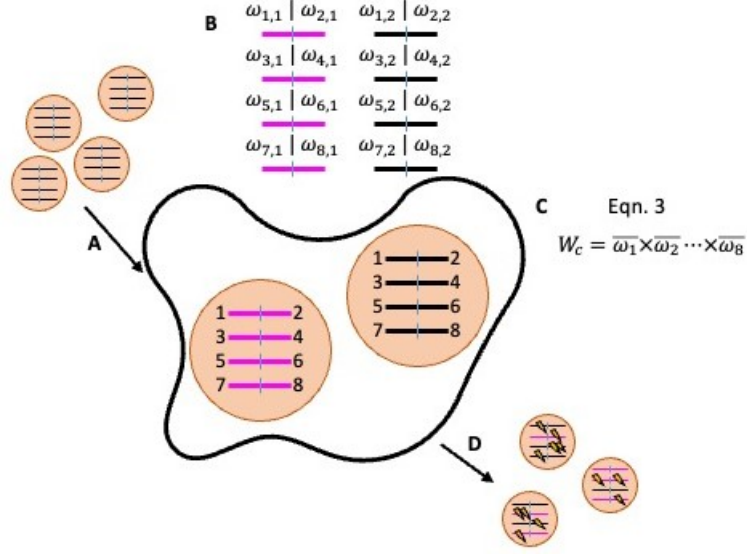
Figure 2.1: Schematic of the base model with a viral genome depicted over a single generation. Each generation consists of a series of steps A-D. (A) V virions infect C cells. Here, two virions infect the shown cell. The viral genomes each have $g = 8$ genes distributed across $y = 4$ gene segments. Each gene is labeled 1-8. (B) Within each cell, the fitnesses of individual gene copies are calculated using equation (2.1). These $\omega_{i,j}$ values are used to calculate the group fitness for each gene. (C) Cellular fitnesses are then calculated using equation (2.3). (D) V viral progeny are formed by selecting parental cells according to their cellular fitnesses, and then selecting gene segments at random from within the cell. Deleterious mutations (lightning bolts) are introduced during the formation of these viral progeny. Steps A-D are repeated for t generations.

C cells, resulting in a Poisson distribution of virions across cells. Once inside the cells, the numbers of mutations on each gene determine the aggregate fitness of the viral population within each cell. This aggregate fitness, which we call "cellular fitness," determines the relative contribution of each cell's virus population to the next generation of virions. To calculate cellular fitness, we first calculate the fitness of each gene that was delivered to a cell:

$$\omega_{i,j} = (1 - s)^{n_{i,j}} \tag{2.1}$$

where s is the constant fitness cost of a deleterious mutation and $n_{i,j}$ is the number of deleterious mutations on gene i delivered by virion j. For each gene i, we calculate

the mean fitness of the gene in a cell as

$$\overline{\omega}_i = \frac{1}{m} \sum_{j=1}^{m} \omega_{i,j} \tag{2.2}$$

where m is the multiplicity of infection of the host cell. Finally, we calculate the expected cellular fitness, W_c, as:

$$W_c = \prod_{i}^{g} \overline{\omega}_i \tag{2.3}$$

Equations $1-3$ make three key assumptions: (1) each mutation within a gene contributes multiplicatively to the fitness of that gene (Eqn. 2.1); (2) each copy of a gene i contributes equally to $\overline{\omega}_i$ via incomplete dominance (Eqn. 2.2); and (3) each gene segment is essential and equally important in its contribution to cellular fitness (Eqn. 2.3). We make these assumptions based on the idea that when multiple virions of differing genotypes infect a cell, the produced viral proteins are treated as common goods used in the generation of progeny virions.

At the end of each generation, we draw the V progeny virions for the next generation from across the set of infected cells. Each progeny virion is drawn independently, with the probability that the virion comes from cell c proportional to W_c. Given that the virion comes from cell c, each of its y gene segments is drawn randomly from the parental virions that infected the cell. As such, a high fitness gene segment is as likely to be drawn from a cell as a low fitness gene segment, reflecting our assumption that cellular fitness depends on the aggregate of shared viral proteins that have been produced in a cell. Once all parental gene segments have been chosen, the mutations are added as described above. We repeat this full process for t discrete generations.

2.3.2 Heterogeneous cellular output stemming from differences in cellular characteristics

Viral output from cells can be affected by host cell characteristics such as size, cell type, and cell cycle stage (Brooke et al., 2013, Schulte and Andino, 2014, Heldt et al., 2015, Golumbeanu et al., 2018, Leviyang and Griva, 2018, Russell et al., 2018, Xin et al., 2018, Phipps et al., 2020, Sun et al., 2020). To consider the effect of heterogeneity in virus output on deleterious mutation accumulation, we extend our base model described above by adapting an approach used by Lloyd-Smith et al. (2005) to describe population-level viral transmission heterogeneity (superspreading dynamics). Specifically, we introduce cellular heterogeneity by making a distinction between the *cellular output* W_c' and the cellular fitness W_c. We make this distinction because the amount of virus produced by a cell is no longer solely determined by the cellular fitness, but now also depends on stochastic factors. For each cell c, the cellular fitness W_c is still determined by the genes of the infecting viruses according to Eqn. 2.3 as above. But in the next generation, the probability that a viral progeny is drawn from c is no longer proportional to W_c, and is instead proportional to W_c', a gamma-distributed random variable with mean W_c and shape parameter k, i.e., probability density function:

$$p\left(W_c' = \omega | W_c\right) = \frac{1}{\Gamma(k)} \left(\frac{k}{W_c}\right)^k \omega^{k-1} e^{-k\omega/W_c}. \tag{2.4}$$

The parameter k controls the extent of cellular heterogeneity. As $k \to \infty$, heterogeneity driven by host cell characteristics becomes minimal and the probability that a progeny virion derives from cell c converges to its cellular fitness, $W_c' \to W_c$. In contrast, as $k \to 0$, the probability that a viral progeny derived from cell c becomes increasingly dependent on host cell characteristics and relatively less dependent on the fitness of viral genes delivered to a cell.

2.3.3 Heterogeneity in cellular output stemming from differences in cellular multiplicity of infection

Virus output from cells can also be affected by cellular multiplicity of infection, with higher cellular MOI having the potential to increase viral yield (Phipps et al., 2020, Martin et al., 2020). To consider the effect that this source of cellular heterogeneity in virus output may have on deleterious mutation accumulation, we extended the base model to allow cellular multiplicity of infection to impact cellular output. Specifically, we let cellular output of a cell with multiplicity of infection m_c be given by a linear relationship between cellular input and cellular fitness, $W_c' = m_c W_c$. While numerous other functional forms are possible, this is the simplest one that allows us to assess the qualitative effect of input-dependence on deleterious mutation accumulation.

2.3.4 Alternative fitness functions

To test the robustness of our results, we also consider alternative models for how cellular fitness depends on the genetic composition of the infecting virions. Above, we assume that the realized fitness of gene segment i is the arithmetic average of the fitnesses of the individual gene segments $i = 1, ..., m$. Here, we can instead consider the possibility that the fitness of gene segments depends on the fitness of the most or least fit infecting gene segment. That is, when calculating the fitness of a gene i, we take either $\omega_i = \max\{\omega_{i,1}, \ldots, \omega_{i,m}\}$ or $\omega_i = \min\{\omega_{i,1}, \ldots, \omega_{i,m}\}$ where m is the multiplicity of infection of the host cell. These are two limiting models for the "dominance" of viral mutations; together with the original fitness function, they span most of the biologically plausible parameter range. We proceed to calculate W_c as in Eqn. 2.3. We estimate the affects of these fitness functions under both the base model structure and with stochastic heterogeneity (Eqn. 2.4).

2.4   Results

In our results, we focus on presenting the mean number of deleterious mutations accumulated in a viral population by generation t. Unless otherwise specified, data shown are from the final generation of the simulated infection, $t = 20$ or $t = 150$. With a viral generation being approximately 5 hours long for viruses such as influenza (Baccam et al., 2006), this corresponds to approximately 4 days post-infection and 31 days post-infection, respectively. In addition to $t = 20$ and $t = 150$ conveniently approximating the number of generations over acute and more chronic infections, we choose these two endpoints due to substantial changes in rates of deleterious mutation accumulation over time. Roughly, $t = 20$ is the time to approach mutation-selection balance for many of our simulations, so changes in the number of accumulated mutations at this time reflect shifts in the mutation-selection balance distribution. At the later time $t = 150$, we can distinguish between populations with a slow-acting Muller's ratchet versus ones with a fast-acting Muller's ratchet.

2.4.1   Phenotypic hiding relaxes selection

We first show that our base model reproduces key findings on deleterious mutation accumulation from previous work using similar cellular coinfection modeling frameworks, in addition to classical population genetics. That is, we establish that the sizes of the virus and host cell populations influence the rate of genetic drift and the extent of phenotypic hiding in the context of cellular coinfection.

For simplicity, we begin by considering an unsegmented genome ($y = 1$), so there is no reassortment. One key finding from the field of population genetics is that reducing population size increases the rate of deleterious mutation accumulation due to an increased rate of genetic drift, particularly in asexual populations (Fisher, 1930, Wright, 1931, Kimura et al., 1963, Lynch et al., 1995). This effect has mostly been

studied under purely individual-level selection. This is a good approximation of our system at low MOI, where most infected cells are infected by only a single virion. Indeed simulations of our model reproduce this effect of population size at low MOI (Fig. 2.2A).
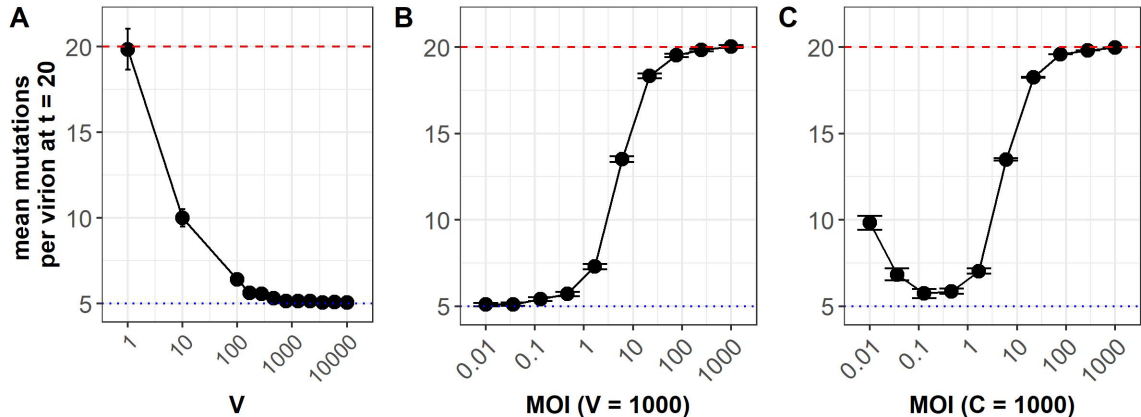
Figure 2.2: Simulated patterns of deleterious mutation accumulation without cellular heterogeneity. **(A)-(C)** Mean number of accumulated mutations at $t = 20$ generations. Each data point shown is the average across 20 replicate simulations with error bars showing the standard error, except for the three largest population sizes in subplot (C), which have only a single replicate shown due to computational limitations. Red dashed lines show the theoretical expectation of mutation accumulation at selective neutrality (Ut). Blue dotted lines show the expectation of mutation accumulation for an infinite viral population size at its mutation-selection balance (U/s). Parameter values are $V = 1000, C = 1000, U = 1, s = 0.2, g = 8, y = 1$ unless otherwise indicated. **(A)** MOI ($= V/C$) is kept constant at 0.1, such that cell population sizes scale linearly with viral population sizes. Higher viral population sizes have lower rates of deleterious mutation accumulation. Large viral populations reach their deterministic mutation-selection balance and have lower rates of deleterious mutation accumulation thereafter. **(B)** The virus population size is kept constant at $V = 1000$ and cell population size C is modified to change MOI. Here, increasing MOI increases phenotypic hiding and therefore deleterious mutation accumulation. **(C)** . The cell population size is kept constant at $C = 1000$ and the virus population size V is modified to change MOI. At low MOI, genetic drift, whose sole effects are shown in (A), dominates and mutation accumulation rates are high because of small viral population sizes. At high MOI, phenotypic hiding, whose effects are shown in (B), dominates and mutation accumulation rates are high because of high levels of cellular coinfection.

Previous work has shown that cellular coinfection and the sharing of viral proteins relaxes the strength of selection on individual virions, and thus allows deleterious mutations to accumulate at a faster rate in viral populations than otherwise

expected (Wilke and Novella, 2003a, Froissart et al., 2004, Novella et al., 2004). Our model recapitulates this "phenotypic hiding" in simulations where the viral population size is kept constant and the number of cells is modified to change the overall MOI (Fig. 2.2B). The monotonic increase in the number of accumulated deleterious mutations in the population in conjunction with increases in MOI is directly attributable to relaxed selection.

In Figure 2.2A, we found that increases in the viral population size (while maintaining a constant MOI) can slow mutation accumulation by decreasing the rate of genetic drift and slowing deleterious mutation accumulation. In Figure 2.2B, however, we found that increases in MOI (while maintaining a constant viral population size) can accelerate mutation accumulation by increasing the extent of phenotypic hiding. Thus, increases in viral population size that are not matched by increases in the size of the cell population could yield a non-monotonic relationship between viral population size and the rate of deleterious mutation accumulation. Figure 2.2C shows the results of this tension between the effects of genetic drift and phenotypic hiding. At low MOI ($\ll 1$), coinfection is rare, and the primary effect of a larger viral population size across simulations is a reduction in the strength of genetic drift, thus decreasing mutation accumulation. As MOI approaches 1, however, phenotypic hiding starts to play a more pronounced role and mutation accumulation increases. At very high MOI ($\gg 1$) phenotypic hiding is essentially complete and deleterious mutations accumulate at the neutral rate U.

Despite having constant sized populations in our simulations, the uniqueness of viral systems occupying high mutation rates with high mutational effects makes analytical inference a challenge. After calculating predictions of mutation accumulation from Gordo and Charlesworth (2000) (their equations 3a and 3b), we get a poor match compared to our simulations (Supplementary Figure A.1). Indeed, their predictions at very small populations exceed the neutral limit of accumulation (data not shown).

We attribute this to our simulations being in a parameter regime that is not often considered when modeling Muller's ratchet, where high mutation rates are constantly introducing large-effect mutations into small populations. Gordo and Charlesworth (2000) models Muller's ratchet where $Ve^{-U/s} >> 1$, and we only approach this regime at large V where phenotypic hiding is more strong than the benefits of large population sizes.

The rate of deleterious mutation accumulation should decrease in segmented viral genomes because reassortment can re-create high fitness genotypes that have been lost to drift by combining segments that have a small number of deleterious mutations, halting Muller's ratchet (Fisher, 1930, Wright, 1931, Kimura et al., 1963, Muller, 1964, Haigh, 1978, Chao, 1990, Chao et al., 1997). We confirm that this occurs in our base model when we consider the viral genome of $g = 8$ genes divided across $y = 1, 2, 4, 8$ gene segments (Fig. 2.3). Because reassortment does not affect the approach to mutation-selection balance, it has little effect at early times (e.g., $t = 20$). But at later times it results in a slower 'clicking' of the ratchet (Fig. 2.3A), and more highly segmented genomes, which allow more reassortment, have lower levels of accumulated deleterious mutations than genomes that have fewer gene segments. Reassortment has the largest effect on mutation accumulation at intermediate viral population sizes that are large enough to effectively select against individual mutations but small enough to be vulnerable to Muller's ratchet, $1/s < V < e^{U/s}/s$ (Lynch et al., 1995, Barton and Otto, 2005). At larger viral population sizes, the ratchet clicks very slowly even in non-reassorting viruses, and therefore reassortment provides little benefit (Fig. 2.3B, right side) (Muller, 1964).

The higher MOI is, the more opportunities viruses have to reassort. Even when cellular coinfection and therefore reassortment is rare (MOI < 1), it can substantially slow Muller's ratchet (Fig. 2.3A, and middle of panel B), consistent with findings from the population genetic literature (Bell, 1988, Charlesworth et al., 1993, Cohen
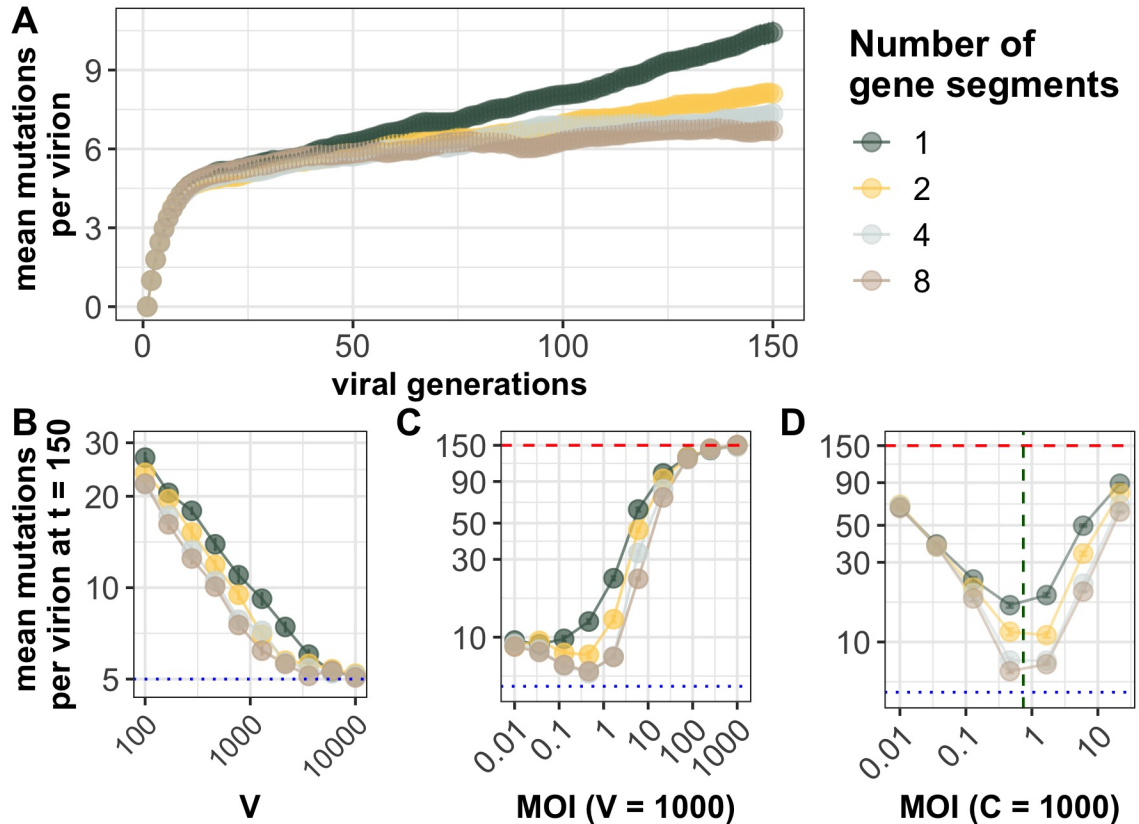
Figure 2.3: Genome segmentation slows the accumulation of deleterious mutations. In (A)–(D), the per genome mutation rate is $U = 1$ and the fitness cost of mutations is $s = 0.2$. Each data point is the average across 20 replicate simulations with error bars showing the standard error. Red dashed lines in (C) and (D) show the theoretical expectation of mutation accumulation at selective neutrality (Ut). Blue dashed lines in (B)–(D) show the expectation of mutation accumulation for an infinite viral population size at its mutation-selection balance (U/s). **(A)** Average number of deleterious mutations accumulated over time at a viral population size $V = 1000$ and a cell population size of $C = 10000$ for varying numbers of segments. **(B)**–**(D)** show the average number of deleterious mutations harbored by a viral population at generation $t = 150$ under different parameters. **(B)** Reassortment slows mutation accumulation in small populations subject to Muller's ratchet. MOI ($= V/C$) is kept constant at 0.1 by scaling linearly the cell population size C proportionally with the viral population size V. **(C)**–**(D)** Mutation accumulation is slowest at intermediate MOI ≈ 0.3 (dashed green vertical line), balancing the effects of reassortment and phenotypic hiding. In **(C)**, MOI is varied by changing C, while in **(D)** it is varied by changing V. At high MOI $\gg 1$, phenotypic hiding is nearly complete and mutations accumulate at close to the neutral rate.

et al., 2006). But higher reassortment rates are more effective at slowing the ratchet. In Figure 2.3C, we keep the viral population size (i.e., drift) the same as we test different sized cell populations to modulate MOI. As coinfection events become more

common at moderate MOI, segmented genomes accumulate fewer deleterious mutations than their unsegmented counterparts. However, segmented genomes are still vulnerable to the impacts of phenotypic hiding. When cellular coinfection is frequent (MOI > 1) and phenotypic hiding causes selection to be ineffective against single mutations, mutations accumulate nearly neutrally and reassortment provides little benefit (Fig. 2.2C and D, right sides). Hence, coinfection is a double-edged sword in populations with segmented genomes because sex and phenotypic hiding change the effective magnitude of selection in opposing directions. The opposing effects create an optimum MOI somewhat less than 1, at which reassortment is frequent but phenotypic hiding only mildly reduces the effectiveness of selection.

2.4.2 Stochastic heterogeneity increases deleterious mutation accumulation

As described in the Model section above, we consider the effect of heterogeneity driven by host cell characteristic by integrating individual cell heterogeneity with virus-driven differences in cellular fitness using draws from a gamma distribution, parameterized with dispersion parameter k. As expected, simulations with $k \gtrsim 1$ behave like the ones described above that do not incorporate stochastic heterogeneity (Fig. 2.4). However, for $k \ll 1$, more deleterious mutations accumulate under all simulated conditions (Fig. 2.4A and Supplementary Figure A.2). This is because the increased stochasticity reduces the efficacy of purifying selection. This has little effect under very high mean MOI $\gg 1$, because phenotypic hiding already weakens selection such that mutations accumulate at nearly the neutral rate, but it can greatly increase mutation accumulation at lower MOI where selection would otherwise be strong enough to halt mutation accumulation.
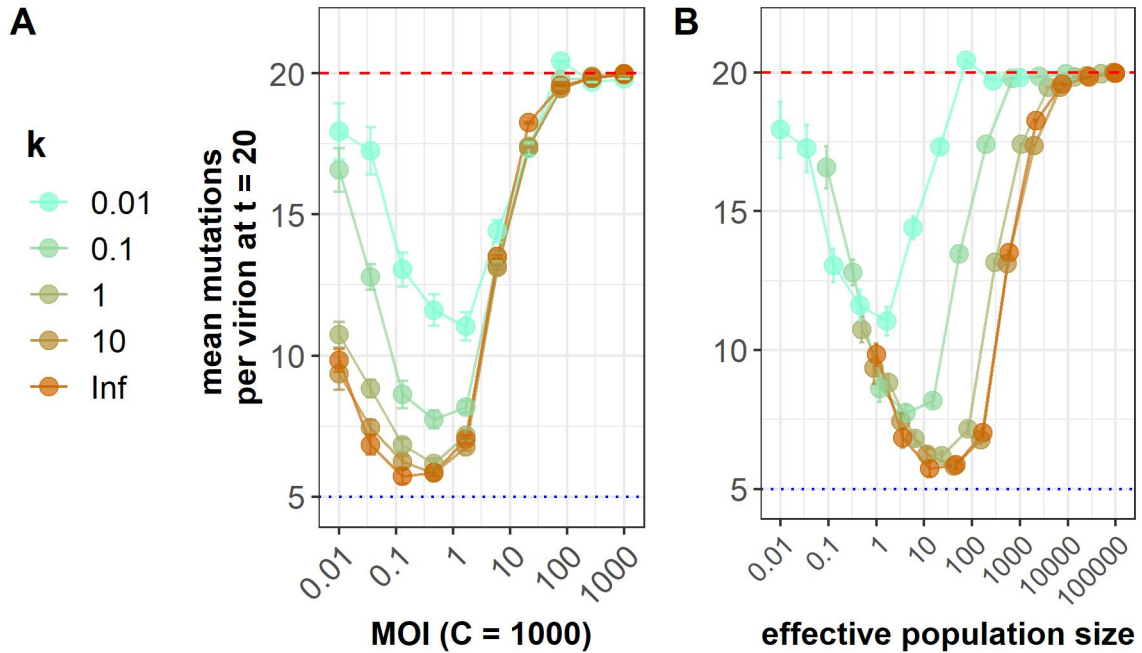
Figure 2.4: Stochastic heterogeneity increases deleterious mutation accumulation. All panels show mean number of deleterious mutations after $t = 20$ generations of within-host infection. Stochastic heterogeneity is parametrized by k, with $k \ll 1$ corresponding to strong heterogeneity and $k = \infty$ corresponding to the base model without heterogeneity. **(A)** Stochastic heterogeneity has the largest effect at low MOI. At high MOI, phenotypic hiding makes selection ineffective even in the absence of heterogeneity. **(B)** Same simulated data as (A), but shown as a function of the predicted effective viral population size $V_e = V/(1 + 1/k)$. The collapse of the different curves on the left side of the plot shows that V_e accurately captures the effect of heterogeneity on mutation accumulation in the regime where stochasticity is strong − small populations. In both panels, each data point shown is the average of 20 replicate simulations with error bars showing the standard error (with the exception of the three largest population sizes in which show only a single simulation). Red dashed lines show the theoretical expected mutation accumulation at selective neutrality (Ut). Blue dashed lines show the average number of mutations for an infinite viral population size at its mutation-selection balance (U/s). Parameters are $C = 1000, U = 1, s = 0.2, y = 1$.

Calculations of viral effective population size show that the impacts of stochastic heterogeneity do not impact mutation accumulation at high MOI

The effect of stochastic cellular heterogeneity on mutation accumulation can be better understood by quantifying the effective viral population size, V_e in these simulations. Stochastic heterogeneity in cellular virus production increases the variance in offspring

number among virions σ^2, and thereby decreases the viral effective population size, given by

$$V_e \equiv V/\sigma^2 \tag{2.5}$$

where σ^2 is more generally the variance in the offspring distribution (Ewens, 1982). We can calculate σ^2 at low MOI ($\ll 1$) where almost all cells are infected with either zero or one virion. Assuming that the population is large and ignoring fitness differences between virions, the offspring distribution is a gamma-Poisson mixture (i.e., a negative binomial) with a mean of 1 (because V is constant) and variance $\sigma^2 = 1 + 1/k$ since each infected cell produces a gamma-distributed number of virions (each cell with a different mean) and the virions infect an approximately Poisson-distributed number of cells in the next generation. When the number of virions is small, this somewhat overestimates the variance, i.e., underestimates V_e, because the Poisson approximation to the binomial offspring distribution allows one individual to have more offspring than there are total virions in the population. Even when the number of virions is large, our formula also overestimates the variance if MOI is large, because the noise in cellular output is shared among coinfecting virions. However, this effect only becomes appreciable when the number of cells is very small.

In the left sides of Figure 2.4 A and B, we see that our calculated viral effective population size V_e is indeed the relevant quantity for evolution at low MOI: viral populations with very different census sizes V but equal effective sizes V_e accumulate mutations are the same rate. However, this breaks down at high MOI (right sides of 2.4 A and B), where census size is the better predictor of evolution. This is because the primary factor reducing the effectiveness of selection is phenotypic hiding, which depends on the census size (through MOI) rather than the amount of stochasticity in reproduction. Note that for the smallest simulated population sizes and k values we still see that our approximate formula for V_e collapses the different curves, even though our approximations are breaking down and the formula is giving unbiological

values of $V_e < 1$.

2.4.3 Input-dependent viral populations accumulate slightly more mutations at intermediate MOI

We next performed simulations under cellular heterogeneity that stems from differences in viral input. When we assumed that viral output scaled linearly with viral input, we found slightly more mutations accumulated compared to the base model at intermediate MOI (Fig. 2.5 and Supplementary Figure A.3). In contrast, at both high and low MOIs, there were no appreciable differences observed from the base model. To understand these results, note that at low MOI ($\ll 1$), almost all infected cells are infected by only a single virion, so the input-output relationship is irrelevant (Supplementary Figure A.3A). At very high MOI ($\gg 1$), phenotypic hiding is nearly complete and mutations accumulate near the neutral rate in both models (Supplementary Figure A.3B). At intermediate MOI, however, there is a mix of singly infected cells, where virions do not experience phenotypic hiding, and multiply infected cells, where virions experience phenotypic hiding. With viral output scaling linearly with viral input, the multiply infected cells contribute more viral progeny to the next generation, thereby increasing the representation of viral genomes that have experienced relaxed selection.

2.4.4 Relaxed selection under phenotypic hiding is robust to the form of the fitness function

Above, we assume that the cellular fitness at gene i, $\overline{\omega}_i$, is determined by the average fitness of the infecting virions at the gene (Eqn. (2.2)); here we consider alternative models. If we think of the virions infecting a cell as being analogous to the homologous chromosomes of a polyploid individual, our model above assumes that there is no

A
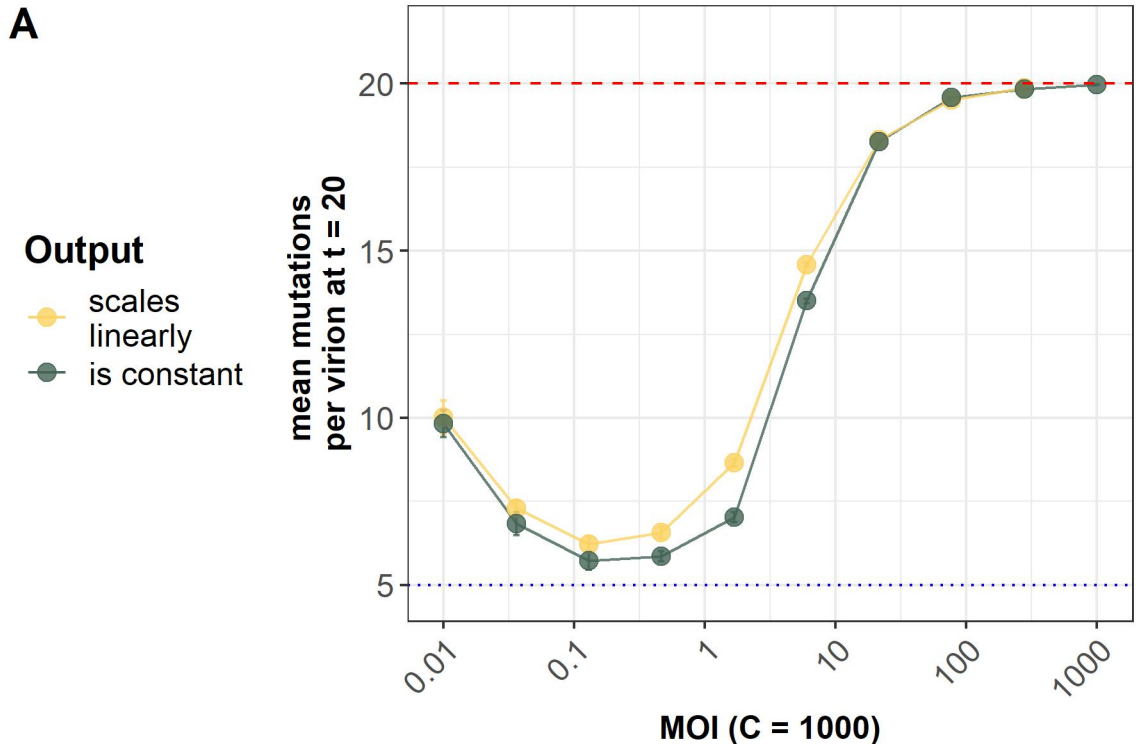
Figure 2.5: Input-dependent cellular fitness values increase the rate of deleterious mutation accumulation slightly at intermediate MOI. The black line show results from the base model. The yellow line shows simulations where cellular fitness W'_c depends both on the amount of viral input m_c to the host cell and the average fitness of the viral genomes in the host cell W_c. We use the per genome mutation rate $U = 1$ and the fitness cost of mutations $s = 0.2$. Each data point shown is the average across 20 replicate simulations with error bars showing the standard error. Red dashed lines show the theoretical expectation of mutation accumulation at selective neutrality (Ut). Blue dashed lines show the expectation of mutation accumulation for an infinite viral population size at its mutation-selection balance (U/s). **(A)** Average number of mutations harbored by an individual virion at generation $t = 20$. The cell population size is kept constant at $C = 1000$ and virus population sizes are modified to change MOI.

"dominance". Here we consider the two limiting possibilities of completely "recessive" or completely "dominant" deleterious mutations, in which the overall fitness of a gene is equal to the fitness of the fittest or least fit infecting copy of the gene, respectively.

Fig. 2.6 shows that our qualitative results on the effects of phenotypic hiding are robust to the form of the fitness function. At low MOI, coinfection is rare, so the alternative fitness functions necessarily produce results that are essentially identical to the base case (Fig. 2.6B and C, MOI ≪ 1; Supplementary Figures A.4

and A.5). At very high MOI, simulations assuming either recessive or dominant mutations both undergo phenotypic hiding and accumulate at nearly the neutral rate, as in the base case (Fig. 2.6B and C, MOI $\gg$ 1). At intermediate MOI, the primary quantitative difference appears to be that the reduced selection on recessive mutations allows them to accumulate more rapidly (Fig. 2.6B and C, MOI $\approx$ 1). Interestingly, selection against dominant mutations is also less effective than in the base case for somewhat large MOI $\approx$ 30. The different fitness functions also do not change the qualitative effect of stochastic heterogeneity in increasing mutation accumulation (Supplementary Figures A.4 and A.5).

While the qualitative patterns of mutation accumulation are unchanged, the fitness function can have a larger effect on the distribution of mutations within the population. For recessive mutations, the distribution of the number of mutations across virions is more prone to transient bimodality, with one cluster of high-fitness virions and another of low-fitness ones that rely on coinfection to reproduce themselves; see Fig. 2.6A for an example. We think transient bimodality occurs because phenotypic hiding allows highly-loaded individuals to cheat, and occasionally rise to high frequencies. Simulations where deleterious mutations are recessive are more likely to allow this phenomenon because the least-fit individuals are hidden from selective forces when they coinfect with individuals near the most-fit peak of the distribution of mutations. However, these dynamics are not the focus of the present work, as more investigation of these bimodal events requires a deeper analysis at longer time scales across a range of MOI.

2.5   Discussion

Here we consider how cellular coinfection in viral infections impacts deleterious mutation accumulation using an *in silico* simulation model. Using our model, we were
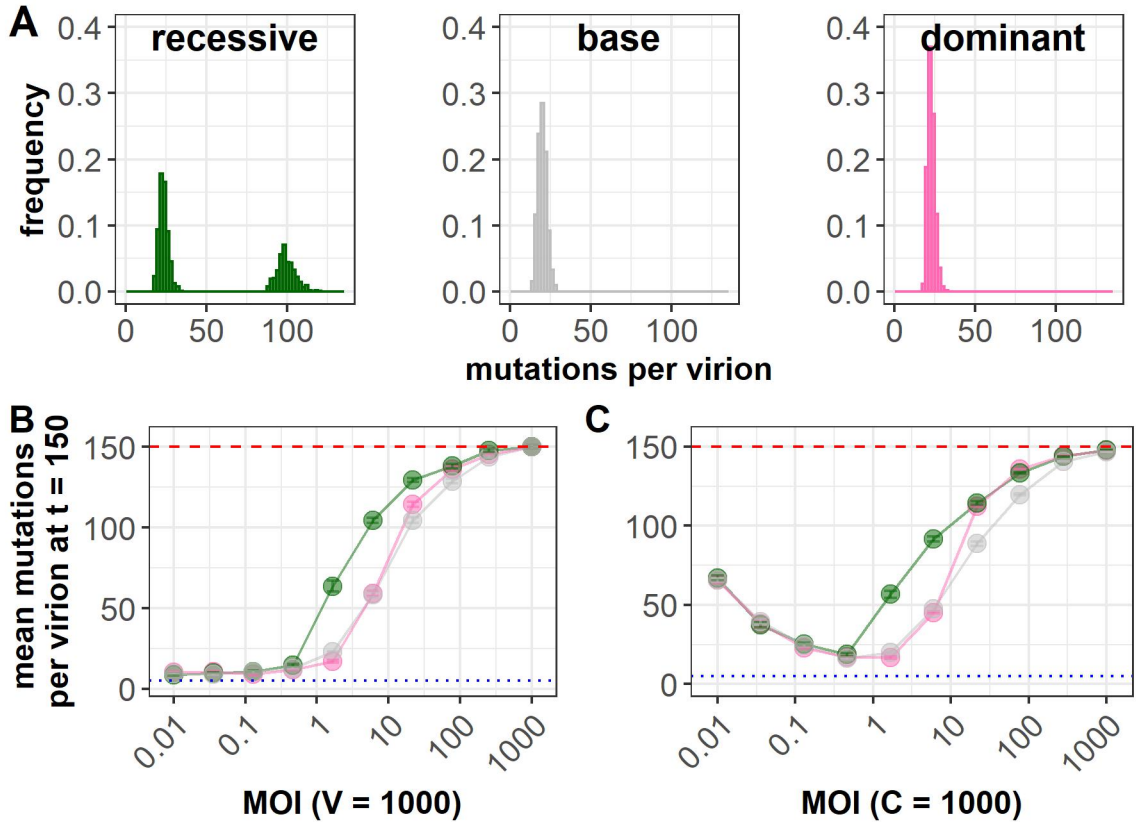
Figure 2.6: Different fitness functions change the distribution of mutations but have only a mild affect on the pattern of phenotypic hiding. In all panels, green indicates that cellular fitness is determined by the most fit virion to infect the cell, i.e., mutations are "recessive". Pink indicates results from simulations in which cellular fitness is determined by the least fit virion to infect the cell, i.e., mutations are "dominant". Grey indicates the base case ("incomplete dominance") shown in previous figures. **(A)** Distributions of numbers of mutations per virion from a single time point of a simulation with $V = 1668$ and $C = 1000$ for each model. The recessive mutations have a bimodal distribution, with individuals tending to either have a low load or a very high one. **(B)** The virus population size is kept constant at $V = 1000$ and cell population size C is modified to change MOI. Recessive mutations accumulate the most rapidly, particularly at intermediate MOI, while dominant mutations accumulate at nearly the base rate. **(C)** The cell population size is kept constant at $C = 1000$ and the virus population size V is modified to change MOI. Recessive mutations accumulate more rapidly than the base case, as do dominant mutations for MOI ≈ 30. In all panels, $U = 1$ and $s = 0.2$. Each data point in B and C is the average across 20 replicate simulations with error bars showing the standard error. Red dashed lines show the theoretical expectation of mutation accumulation at selective neutrality (Ut). Blue dashed lines show the expected number of mutations for an infinite viral population size at its mutation-selection balance (U/s).

able to recapitulate previous results of relaxed selection that occurs under regimes

of phenotypic hiding (Wilke and Novella, 2003a, Froissart et al., 2004, Novella et al.,

2004). We then extended these findings by showing that the heterogeneity inherent to viral infections, including cellular heterogeneity and differences in production of virions due to variation in number of infecting viral particles, increases the rates of deleterious mutation accumulation during viral infections.

Segmentation and reassortment reduce the rate of deleterious mutation accumulation among genes by allowing more fit genotypes to jointly reproduce progeny that do not contain all of the deleterious mutations harbored by their parents (Turner, 2003). However, our simulations indicate that phenotypic hiding can drastically reduce this benefit of segmented genomes (Fig. 2.3C). We show that intermediate levels of coinfection (MOI $\approx$ 0.3) are optimal for segmented viral populations since they allow sex to occur frequently enough to reduce mutation accumulation without significant levels of phenotypic hiding. While we focused on a genetic architecture based on influenza virus and therefore did not incorporate recombination into our model, we expect that recombination would give the same qualitative results as those we report for reassortment.

While our extensions to the base model have incorporated some realism, our model remains highly simplified. In particular, there are two key features of natural infections which impact population dynamics that we did not incorporate. First, many infections show substantial spatial structure (reviewed in Gallagher et al. (2018)). This could result in high MOI hotspots, increasing the potential for both phenotypic hiding and, in segmented viruses, reassortment. However, spatial structure also means that coinfecting virions are likely to be close relatives, reducing both the negative impact of phenotypic hiding and the benefits of reassortment.

The second aspect of natural infections not considered in our model is that we assume a constant viral population size, while natural infections expand from a small inoculum. Population expansion has been shown to increase the number of segregating deleterious mutations in the population but also decreases the per individual

number of deleterious mutations (Gazave et al., 2013). We do not know how population expansion would interact with cellular coinfection. Interpreting our results using Figure 2.2C indicates that if a viral population were to grow in a limited cell population, it would experience three stages. First at low MOI, selection would be at the individual level in a small population susceptible to drift. Then, selection would become more effective over the course of an infection as viral population size increases up until intermediate MOI. Finally, at high population sizes, the population would experience high levels of phenotypic hiding due to the density of viruses infecting cells, thus reducing the efficacy of selection. On the other hand, it is unclear what would happen if the viral population were to continue to colonize new tissue as it grew such that MOI remained roughly constant.

One possible genetic extension of our model would be to include epistasis among mutations. Positive epistasis would result in additional mutations accumulating because the fitness effect of adding a new mutation decreases with each subsequent mutation. Negative epistasis would have the opposite effect: selection would be more strict and thus fewer mutations would accumulate. However, neither form of epistasis should have much effect on mutation accumulation at high MOI where phenotypic hiding renders mutations effectively neutral.

Phenotypic hiding can be seen as an example of social interactions between viruses at the intracellular level. The emerging field of "sociovirology" examines how such interactions between viruses, including during cellular coinfection, can have an impact on the evolution of viral populations (Vignuzzi et al., 2006, Andino and Domingo, 2015, Bordería et al., 2015, Díaz-Muñoz et al., 2017, Sanjuán, 2017, Aguilera and Pfeiffer, 2019). The importance of coinfection in viral evolution has been demonstrated empirically (Chao et al., 1997, Turner et al., 1999, Wilke and Novella, 2003a, Froissart et al., 2004). Specifically, cellular MOI depends on viral traits such as aggregation via collective infectious units (reviewed in Sanjuán (2017)), while other traits may limit

coinfection via superinfection exclusion (Sun and Brooke, 2018). Some of the other modern work in the field also highlights the role of heterogeneity (Andreu-Moreno and Sanjuán, 2018, Sun and Brooke, 2018). However, while much of sociovirology focuses on positive selection, our work shows that interactions among virions also have large effects on the ability of purifying selection to shape the evolution of viral populations.

Data Availability

The code used to produce the data shown in this paper was written and implemented in MATLAB R2020a and is available at `https://github.com/allmanbrent/coinfection_heterogeneity`. Visualization was performed using R version 4.0.1.

Appendix A

Supplementary Materials to Chapter 2

A.1 Base Model Comparison Against Gordo and Charlesworth (2000)
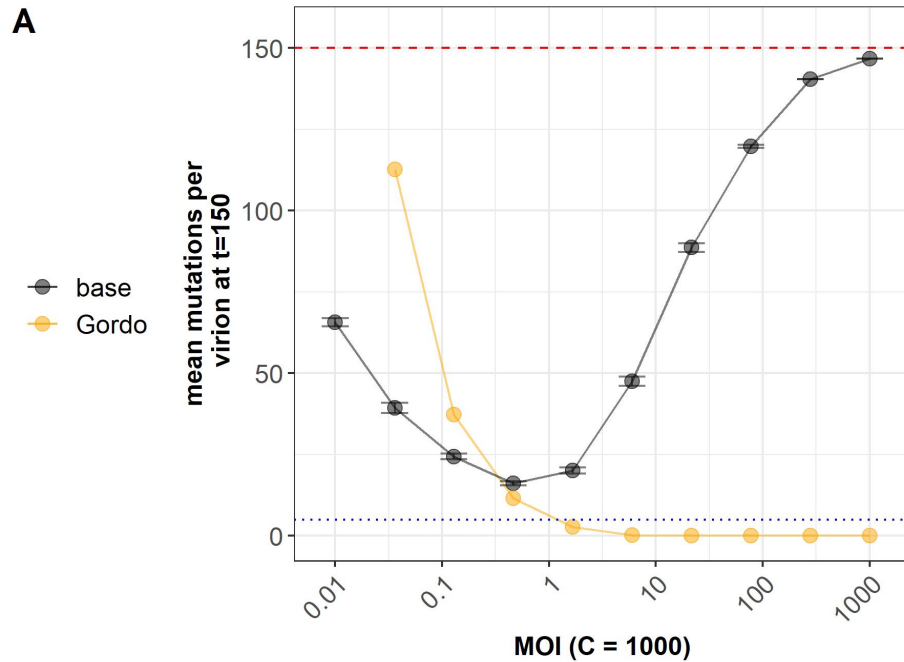
Figure A.1: The results from our base model are not well-predicted by existing models. Panel shows the mean number of deleterious mutations after $t = 150$ generations as simulated by our base model (black) and as predicted by Gordo and Charlesworth (2000) (orange) under equivalent viral population sizes. Each data point in black is the average of 20 replicate simulations with error bars showing the standard error. Red dashed lines show the theoretical expected mutation accumulation at selective neutrality (Ut). Blue dashed lines show the average number of mutations for an infinite viral population size at its mutation-selection balance (U/s). Parameters are $U = 1, s = 0.2, y = 1$, with values of k indicated by color. **(A)** The cell population size is kept constant at $C = 1000$ and the virus population size V is modified to change MOI.

A.2 Stochastic Heterogeneity
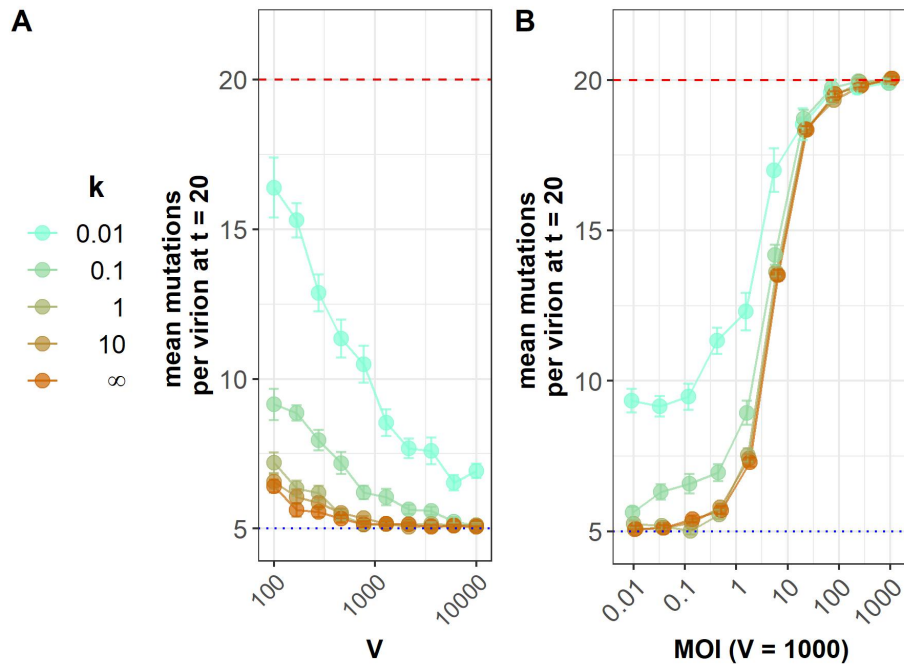
Figure A.2: Stochastic heterogeneity increases deleterious mutation accumulation at low and intermediate MOI, but not at high MOI. All panels show mean number of deleterious mutations after $t = 20$ generations. Each data point shown is the average of 20 replicate simulations with error bars showing the standard error. Red dashed lines show the theoretical expected mutation accumulation at selective neutrality (Ut). Blue dashed lines show the average number of mutations for an infinite viral population size at its mutation-selection balance (U/s). Parameters are $U = 1, s = 0.2, y = 1$, with values of k indicated by color. **(A)** At a constant MOI of 0.1, stochastic heterogeneity increases mutation accumulation. **(B)** In these simulations, the virus population size is kept constant at $V = 1000$ and cell population sizes are modified to change MOI. Different k in (A) and (B) show that additional stochastic heterogeneity (small k) leads to additional mutation accumulation until phenotypic hiding is prominent.

A.3 Input-Dependent Heterogeneity
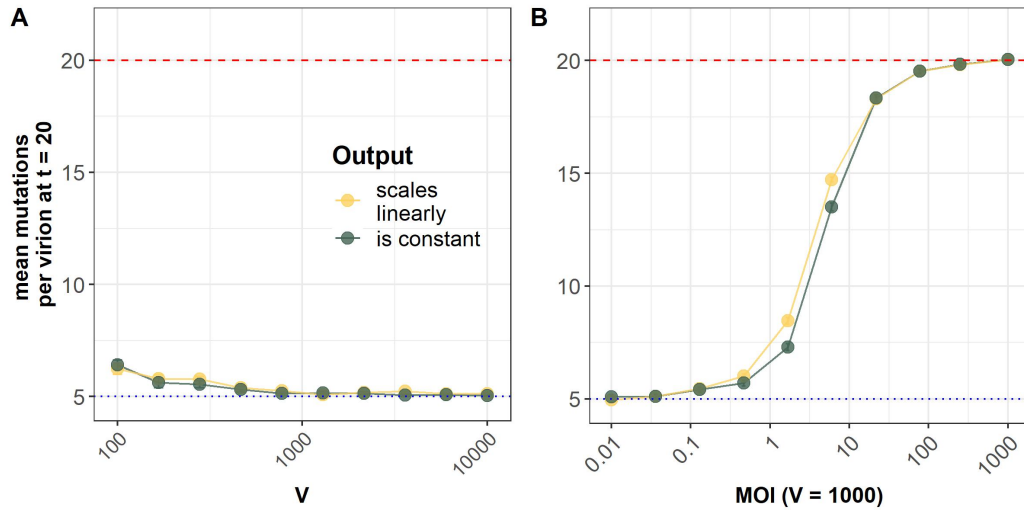
Figure A.3: Input-dependent cellular fitness values minimally affect mutation accumulation patterns. The black line represents simulations where there is no input-output relationship (i.e. the base model). The yellow line shows simulations where we have implemented our input-dependent model. We use the per genome mutation rate $U = 1$ and the fitness cost of mutations $s = 0.2$. Each data point shown is the average across 20 replicate simulations with error bars showing the standard error. Red dashed lines show the theoretical expectation of mutation accumulation at selective neutrality (Ut). Blue dashed lines show the expectation of mutation accumulation for an infinite viral population size at its mutation-selection balance (U/s). **(A)** Average number of mutations harbored by an individual virion at generation $t = 20$. Here, cell population sizes are changed accordingly across simulated viral population sizes to maintain an MOI of 0.1. **(B)** Average number of mutations harbored by an individual virion at generation $t = 20$. The virus population size is kept constant at $V = 1000$ and cell population sizes are modified to change MOI.

A.4 Stochastic Heterogeneity Impacts Are Consistent Across Alternative Fitness Functions

A.4.1 Simulated mutations are assumed to be "dominant"
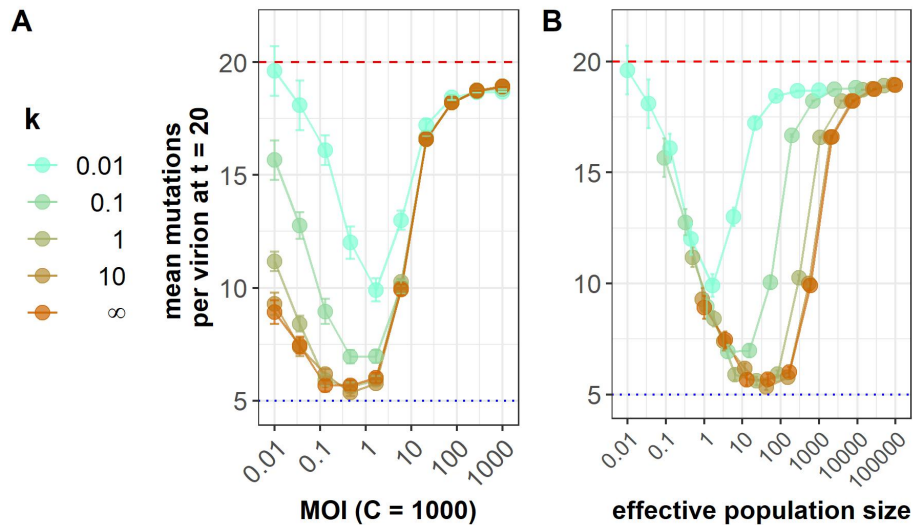
Figure A.4: Stochastic heterogeneity increases deleterious mutation accumulation when genic fitness takes the form $\omega_i = \min\{\omega_{i,1}, \ldots, \omega_{i,m}\}$ as described in the Methods of the main text. All panels show mean number of deleterious mutations after $t = 20$ generations of within-host infection. Each data point shown is the average of 20 replicate simulations with error bars showing the standard error. Red dashed lines show the theoretical expected mutation accumulation at selective neutrality (Ut). Blue dashed lines show the average number of mutations for an infinite viral population size at its mutation-selection balance (U/s). Parameters are $U = 1, s = 0.2, y = 1$, with values of k indicated by color. (A) Stochastic heterogeneity has the largest effect at low MOI. At high MOI, phenotypic hiding makes selection ineffective even in the absence of heterogeneity. (B) Same simulated data as (A), but shown as a function of the predicted effective viral population size $V_e = V/(1+1/k)$. The collapse of the different curves on the left side of the plot shows that V_e accurately captures the effect of heterogeneity on mutation accumulation in the regime where stochasticity is strong − small populations.

A.4.2 Simulated mutations are assumed to be "recessive"
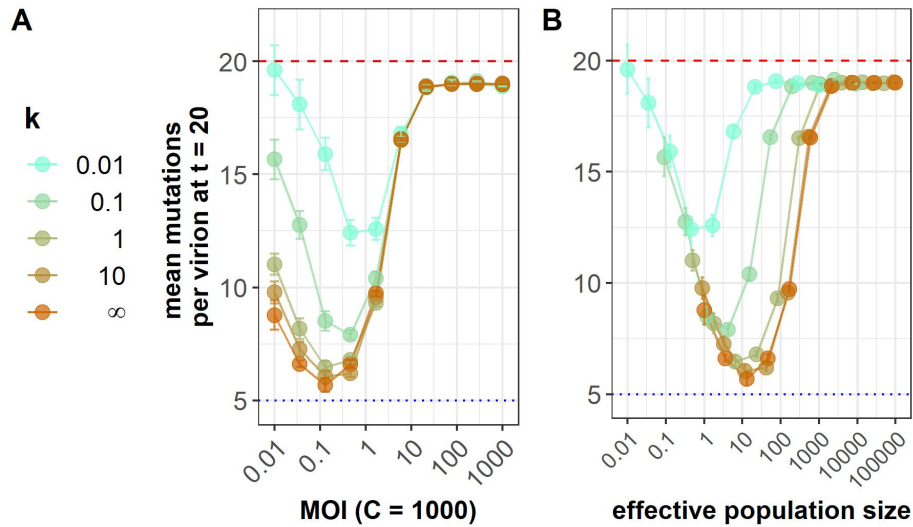
Figure A.5: Stochastic heterogeneity increases deleterious mutation accumulation when genic fitness takes the form $\omega_i = \max\{\omega_{i,1}, \ldots, \omega_{i,m}\}$ as described in the Methods of the main text. All panels show mean number of deleterious mutations after $t = 20$ generations of within-host infection. Each data point shown is the average of 20 replicate simulations with error bars showing the standard error. Red dashed lines show the theoretical expected mutation accumulation at selective neutrality (Ut). Blue dashed lines show the average number of mutations for an infinite viral population size at its mutation-selection balance (U/s). Parameters are $U = 1, s = 0.2, y = 1$, with values of k indicated by color. **(B)** Stochastic heterogeneity has the largest effect at low MOI. At high MOI, phenotypic hiding makes selection ineffective even in the absence of heterogeneity. **(B)** Same simulated data as (A), but shown as a function of the predicted effective viral population size $V_e = V/(1+1/k)$. The collapse of the different curves on the left side of the plot shows that V_e accurately captures the effect of heterogeneity on mutation accumulation in the regime where stochasticity is strong − small populations.

Chapter 3

Fitness estimation for viral variants in the context of cellular coinfection

In the following publication, we develop a model of viral variant growth that accounts for our previously described assumptions around public goods within host cells. We then use this model in both deterministic and stochastic simulations to fit model parameters to experimental influenza A virus infections in ferret hosts (Wilker et al., 2013). Specifically, we leverage *a priori* estimates of MOI to inform estimates of the fitness of a viral variant.

viruses

MDPI

Article

Fitness Estimation for Viral Variants in the Context of Cellular Coinfection

Huisheng Zhu [1,†], Brent E. Allman [2,†] and Katia Koelle [1,3,*]

1   Department of Biology, Emory University, Atlanta, GA 30322, USA; julie.zhu@emory.edu
2   Graduate Program in Population Biology, Ecology, and Evolution, Emory University, Atlanta, GA 30322, USA; brent.elliott.allman@emory.edu
3   Emory-UGA Center of Excellence for Influenza Research and Surveillance (CEIRS), Atlanta, GA 30322, USA
*   Correspondence: katia.koelle@emory.edu
†   Equal contributions.

Abstract: Animal models are frequently used to characterize the within-host dynamics of emerging zoonotic viruses. More recent studies have also deep-sequenced longitudinal viral samples originating from experimental challenges to gain a better understanding of how these viruses may evolve in vivo and between transmission events. These studies have often identified nucleotide variants that can replicate more efficiently within hosts and also transmit more effectively between hosts. Quantifying the degree to which a mutation impacts viral fitness within a host can improve identification of variants that are of particular epidemiological concern and our ability to anticipate viral adaptation at the population level. While methods have been developed to quantify the fitness effects of mutations using observed changes in allele frequencies over the course of a host's infection, none of the existing methods account for the possibility of cellular coinfection. Here, we develop mathematical models to project variant allele frequency changes in the context of cellular coinfection and, further, integrate these models with statistical inference approaches to demonstrate how variant fitness can be estimated alongside cellular multiplicity of infection. We apply our approaches to empirical longitudinally sampled H5N1 sequence data from ferrets. Our results indicate that previous studies may have significantly underestimated the within-host fitness advantage of viral variants. These findings underscore the importance of considering the process of cellular coinfection when studying within-host viral evolutionary dynamics.

Keywords: within-host dynamics; viral evolution; influenza H5N1; viral modeling

1. Introduction

Zoonotic pathogens are often poorly adapted to their spillover hosts. Viral adaptation, however, can occur during epidemiological spread following spillover, resulting in increases in viral transmission potential as the pathogen establishes itself in the host population [1]. This was observed most notably in influenza viruses that have successfully established in humans (e.g., [2,3]). The pandemic coronavirus SARS-CoV-2 provides a more recent example, with variant lineages that are better adapted to human hosts (such as D614G [4]) emerging and replacing earlier viral lineages. Viral adaptations that improve transmission potential often arise from their effect on within-host replication dynamics. For example, mutations that enable viruses to replicate more efficiently within hosts (in particular, in transmission-relevant tissues) could enhance transmission potential, as could mutations that allow for a more effective evasion of the host immune response.

In vivo studies could in principle be used to identify mutations that improve viral fitness in a spillover host. For example, experiments using the ferret animal model identified a set of influenza A subtype H5N1 mutations that increase viral replication within the nasal turbinate of hosts (a transmission-relevant tissue) and also increase transmissibility [5,6].

The fitness effects of mutations such as these have been estimated by interfacing quantitative models with data on how variants carrying these mutations change in frequency over the course of infection [7–9]. However, these approaches assume that fitness is an individual-level property of a variant. While this may be the case when cells are only singly infected, many viral infections involve significant levels of cellular coinfection. For example, due to incomplete viral genomes, influenza viruses heavily rely on complementation to produce viral progeny [10–12]. High levels of cellular coinfection in other viruses, such as HIV, is also likely, given the pervasiveness of recombinant genomes that are identified during viral sequencing [13,14].

Cellular coinfection can impede the ability of high-fitness variants to rise to high frequencies within an infected host. This is because of the phenomenon of 'phenotypic hiding' [15,16]. Phenotypic hiding comes about as a consequence of viral protein products being shared within coinfected cells. Delivery of a viral genome carrying a highly beneficial mutation results in the production of a viral protein that can provide a replicative benefit to all of the viral genomes present in the coinfected cell. Similarly, a viral genome carrying a deleterious (and potentially even lethal) mutation can be rescued by protein products derived from coinfecting viral genomes. Cellular coinfection thus results in natural selection no longer acting on individual viral genomes, but instead on viral collectives. This effectively reduces the strength of selection, such that deleterious mutations are purged more slowly [17] and beneficial mutations are also fixed more slowly [18]. As a result, the extent of cellular coinfection impacts the dynamics of allele frequency changes in an infection and affects fitness inference.

Here, we first develop a set of mathematical models to project changes in the allele frequencies of viral variants within infected hosts. Our models specifically allow for cellular coinfection and the effect of phenotypic hiding on allele frequency changes. Using Bayesian inference approaches, we then demonstrate how these mathematical models can be interfaced with longitudinally sampled allele frequency data to jointly estimate the relative fitness of a variant and cellular multiplicity of infection levels. Finally, we apply our developed methods to estimate the fitness effect of an adaptive mutation that was identified in an influenza H5N1 experimental challenge study performed using the ferret animal model. Our findings indicate that the fitness effect of this mutation is considerably higher than previously estimated and that cellular coinfection precipitously slowed down the rate of within-host influenza virus adaptation.

2. Materials and Methods

2.1. Deterministic Within-Host Evolution Model

Several studies have used longitudinal allele frequency data to estimate the relative fitness of a mutant allele over a wild-type allele within an infected host or from passage studies [9,19,20]. None of these models, however, account for the impact that cellular coinfection can have on variant allele frequency changes over time. To accommodate cellular coinfection, we first start with an evolutionary model that projects allele frequencies from one viral generation to the next in the absence of coinfection:

$$q^m(t_{g+1}) = \frac{q^m(t_g)e^{\sigma_m}}{q^m(t_g)e^{\sigma_m} + (1 - q^m(t_g))e^{\sigma_w}} \tag{1}$$

where $q^m(t_g)$ is the frequency of the variant (mutant) allele in viral generation g, σ_m (with range $-\infty$ to ∞) is the selective advantage/disadvantage of the focal mutation, and e^{σ_m} (with range ≥ 0) is the relative fitness of the variant allele over the wild-type allele. The fitness of the wild-type allele (e^{σ_w}) is defined as 1. This model is a simplification of a model first presented in [9]. That model considers an arbitrary number of viral haplotypes and further incorporates de novo mutation in its projection of allele frequencies. Here, we ignore de novo mutation over the course of infection and limit our analysis to two viral haplotypes: a wild-type viral genotype and a variant genotype carrying a mutant allele

at a single locus. We adopt these simplifications to focus attention on the effect of cellular coinfection in within-host evolution.

To extend this initial model to allow for the effect of cellular coinfection, we first assume that viral genomes enter cells independently of other viral genomes. Under this assumption, viral genomes are distributed across cells according to a Poisson distribution. Given a mean overall cellular multiplicity of infection (MOI) of M, the variant's mean MOI in viral generation t_g is simply given by $M_m = q^m(t_g)M$ and the wild-type virus's mean MOI is simply given by $M_w = (1 - q^m(t_g))M$. The probability that a cell is infected with k variant viral genomes and l wild-type viral genomes is then:

$$P(k,l) = \left(\frac{e^{-M_m}(M_m)^k}{k!} \right) \left(\frac{e^{-M_w}(M_w)^l}{l!} \right) \tag{2}$$

Under the assumption that viral protein products within cells have additive effects, the fitness of a viral genome present in a cell carrying k variant viral genomes and l wild-type viral genomes is given by:

$$F(k,l) = \frac{k}{k+l}e^{\sigma_m} + \frac{l}{k+l}e^{\sigma_w} \tag{3}$$

Note that this fitness does not depend on whether the focal genome is a variant viral genome or a wild-type viral genome, since all viral genomes within a cell share their protein products and thus have the same fitness.

The realized mean fitness of a viral variant in the context of cellular coinfection is calculated by taking a fitness average of the viral variant across its cellular contexts:

$$\overline{e^{\sigma_m}} = \frac{\sum_{k=0}^{\infty} \sum_{l=0}^{\infty} kP(k,l)F(k,l)}{M_m} \tag{4}$$

Similarly, and the realized mean fitness of the wild-type virus in the context of cellular coinfection is given by:

$$\overline{e^{\sigma_w}} = \frac{\sum_{k=0}^{\infty} \sum_{l=0}^{\infty} lP(k,l)F(k,l)}{M_w} \tag{5}$$

Examination of these equations indicates that the realized mean fitness of the viral variant and of the wild-type virus approach e^{σ_m} and e^{σ_w}, respectively, as cellular MOI becomes small, as expected. As cellular MOI becomes large, $\overline{e^{\sigma_m}}$ and $\overline{e^{\sigma_w}}$ converge in their values, as expected.

Variant allele frequency changes in the context of cellular coinfection can then be projected using a modified version of Equation (1), where realized mean fitnesses replace individual-level viral fitnesses:

$$q^m(t_{g+1}) = \frac{q^m(t_g)\overline{e^{\sigma_m}}}{q^m(t_g)\overline{e^{\sigma_m}} + (1 - q^m(t_g))\overline{e^{\sigma_w}}} \tag{6}$$

2.2. Stochastic Within-Host Evolution Model

A recent study highlighted the important role that stochastic processes can play in shaping patterns of within-host viral evolution [21]. The extent to which in vivo viral evolution is governed by stochastic processes can be quantified by the within-host effective viral population size, which we here refer to as N_e. Low values of N_e indicate that genetic drift plays a large role in shaping within-host viral populations, while high values of N_e indicate that genetic drift plays a more minor role. The within-host effective viral population size N_e for seasonal influenza A viruses has recently been estimated as being on the order of 30–70 [22]. Given estimates such as these, we develop here a stochastic version of the within-host evolutionary model presented in the previous section. For simplicity, in the equations below, we use N rather than N_e to denote the effective viral population size.

With a variant allele frequency of $q^m(t_g)$ in generation t_g, the variant's effective population size is given by:

$$N_m(t_g) = Nq^m(t_g) \tag{7}$$

and the effective population size of the wild-type virus in generation t_g is given by:

$$N_w(t_g) = N(1 - q^m(t_g)) \tag{8}$$

Defining the number of target cells as C, the mean cellular multiplicity of infection is given by N/C, the mean cellular MOI of variant virus is given by N_m/C, and the mean cellular MOI of the wild-type virus is given by N_w/C. Under the same assumption as before that viral genomes enter cells independently of one another, we stochastically determine the distribution of variant viruses across target cells using a multinomial distribution with the event probability of being in a cell given by $1/C$ (for all C cells) and the number of trials given by the variant population size N_m. We similarly stochastically determine the distribution of wild-type viruses across target cells using a multinomial distribution with the event probability of being in a cell given by $1/C$ (for all C cells) and the number of trials given by the wild-type viral population size N_w. The mean fitness of a viral variant in the context of cellular coinfection can then be calculated in a manner similar to the one specified in Equation (4). With $F(k_i, l_i)$ as the fitness of a viral genome present in cell i with k_i variant viral genomes and l_i wild-type viral genomes, the mean fitness of a viral variant is obtained by considering the stochastically realized viral content in each cell:

$$\overline{e^{\sigma_m}} = \frac{\sum_{i=1}^C k_i F(k_i, l_i)}{N_m} \tag{9}$$

Similarly, the mean fitness of the wild-type virus is given by:

$$\overline{e^{\sigma_w}} = \frac{\sum_{i=1}^C l_i F(k_i, l_i)}{N_w} \tag{10}$$

We then use Equation (6) to project the frequency of the viral variant in the next generation. Calling this projected frequency $p^m(t_{g+1})$, we generate a stochastic realization of this frequency by letting the variant effective population size N_m be drawn from a binomial distribution with N trials and a probability of success of $p^m(t_{g+1})$. The realized frequency of the viral variant, $q^m(t_{g+1})$, in generation t_{g+1} is then given by N_m/N.

2.3. Simulated Data

We simulated the models described above to ascertain the effect of cellular coinfection on variant allele frequency changes at various levels of coinfection. We also simulated mock datasets and used them to test the statistical inference methods described in detail below. We simulated one mock dataset using the deterministic within-host evolution model, with observed variant allele frequencies that include measurement noise (noise that is due to an inaccurate measuring process, rather than underlying noise in the viral dynamic process) . To implement measurement noise, we let the *observed* variant allele frequency in generation t_g, $q_o^m(t_g)$, be drawn from a beta distribution with shape parameter $\alpha = \nu q^m(t_g)$ and shape parameter $\beta = \nu(1 - q^m(t_g))$:

$$q_o^m(t_g) \sim Beta(\nu q^m(t_g), \nu(1 - q^m(t_g)))$$

where ν quantifies the degree of measurement noise. The parameter ν is constrained to be positive, with higher values corresponding to less measurement noise. We simulated a second mock dataset using the stochastic within-host model, similarly assuming beta-distributed measurement noise.

2.4. Empirical H5N1 Data

As an application of the approaches developed here, we used longitudinal allele frequency data from an influenza A subtype H5N1 experimental challenge study in ferrets [23]. We specifically focused on inferring the relative fitness of a single nucleotide variant on the hemagglutinin gene segment (G788A) in the VN1203-HA(4)-CA04 virus. This variant was present in the viral inoculum stock at a frequency of 4.40% and increased in frequency over the course of infection in each of the four ferrets that were challenged with this inoculum. Although G788A allele frequencies were measured in [23] on days 1, 3, and 5 post-inoculation, we excluded the day 5 samples from our analyses. This is because up to (and including) day 3, the viral population in each of the four ferrets exhibited low levels of genetic diversity, with G788A being the only variant present at substantial frequencies. By day 5, additional variants on the hemagglutinin gene segment had emerged, with some reaching high frequencies. Because there is genetic linkage between these later variants and G788A, the G788A frequency changes between days 3 and 5 are likely due in part to selection acting on these later variants. Because our model does not reconstruct viral haplotypes or consider epistatic interactions between loci, we thus decided to exclude day 5 from our analysis to be able to focus more specifically on estimating the fitness of G788A in the context of cellular coinfection.

2.5. Statistical Inference

The deterministic within-host model contains four parameters: the relative fitness of the variant virus (e^{σ_m}) over the wild-type virus, the mean cellular multiplicity of infection (M), the initial frequency of the variant virus in a host ($q^m(t_0)$), and the magnitude of measurement noise (ν). When interfacing this model with longitudinal allele frequency data, we estimate the first three parameters but do not estimate ν. We do not estimate ν because it can be parameterized from allele frequency measurements from replicate samples. To estimate e^{σ_m}, M, and $q^m(t_0)$, we rely on Markov Chain Monte Carlo (MCMC) approaches.

The stochastic within-host evolution model contains the same four parameters as the deterministic model, and one additional parameter: the effective viral population size N. (The number of target cells C is not an additional parameter because it is given by the product of the effective viral population size N and the mean cellular MOI M.) We use particle MCMC (pMCMC) [24] to infer e^{σ_m}, M, and $q^m(t_0)$, and set ν and N as given. Particle MCMC is a Bayesian inference approach that combines particle filtering with MCMC to estimate parameters of stochastic state-space models and to reconstruct unobserved state variables. This statistical inference method is increasingly used in the infectious disease modeling community [25,26] but as of yet has not been applied to within-host viral models.

For both the deterministic and stochastic within-host models, let $P(q_o^m(t_g))$ be the probability of observing a variant allele frequency of q_o^m in generation t_g. This probability is given by the beta probability density function, with shape parameters $\nu q_{sim}^m(t_g)$ and $\nu(1 - q_{sim}^m(t_g))$, evaluated at $q_o^m(t_g)$, where $q_{sim}^m(t_g)$ is the model-simulated allele frequency in generation t_g. This simulated variant allele frequency depends on parameters e^{σ_m}, M, and $q^m(t_0)$, and for the stochastic model also N. For the deterministic model, the likelihood of the model is then given by:

$$\prod_g P(q_o^m(t_g)) \tag{11}$$

where g indexes the generation times of all the measured variant allele frequency data points. For the stochastic model, $P(q_o^m(t_g))$ is used to calculate the particle weights in the pMCMC algorithm.

Statistical inference code was implemented using Python 3.7.4 and Matlab R2020A and is available from https://github.com/koellelab/withinhost_fitnessInference.

3. Results

3.1. The Extent of Cellular Coinfection Impacts Variant Frequency Dynamics

The within-host models developed above differ from previous models focused on within-host viral evolution by incorporating the possibility of cellular coinfection and its effects on variant frequency dynamics. Simulations of our deterministic model show, as expected, that a beneficial mutation does not increase in frequency as rapidly when cellular coinfection levels are high compared to when they are low (Figure 1A). Our simulations also show that a deleterious mutation does not decrease in frequency as rapidly when cellular coinfection levels are high compared to when they are low (Figure 1B). Both of these effects are a direct consequence of phenotypic hiding that occurs in cells that are infected by more than one viral genome.
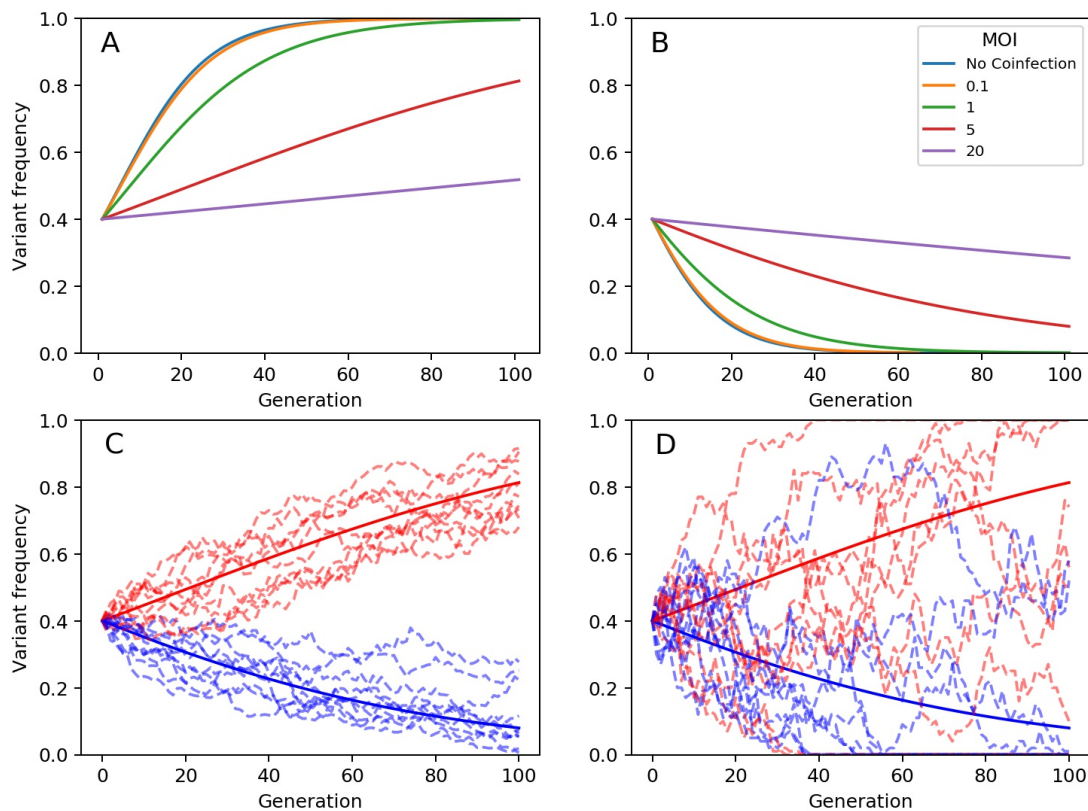
Figure 1. Model simulations showing changes in variant frequencies over viral generations. (**A**) Frequency changes of a beneficial mutation under the deterministic within-host model, parameterized at different mean cellular multiplicities of infection M. For all simulations shown, the variant's fitness is $e^{\sigma_m} = 1.1$ and its initial frequency is $q^m(t_0) = 0.4$. (**B**) Frequency changes of a deleterious mutation under the deterministic within-host model, parameterized at different mean cellular multiplicities of infection M. For all simulations shown, the variant's fitness is $e^{\sigma_m} = 0.9$ and its initial frequency is $q^m(t_0) = 0.4$. In (**A,B**), we consider MOI values of 0.1, 1, 5, and 20. Labeled as 'No coinfection', we also plot simulations of the model presented in Equation (1), which assumes that fitness is an individual-level property of a viral genome. (**C**) Frequency changes of a beneficial mutation (red; $e^{\sigma_m} = 1.1$) and of a deleterious mutation (blue; $e^{\sigma_m} = 0.9$) under the stochastic within-host model, parameterized with a mean cellular MOI of 5. Dashed lines show 10 stochastic realizations under each parameterization. Solid lines show simulations of the deterministic model under the same parameterization. Stochastic simulations used an effective viral population size of $N = 1000$. (**D**) Frequency changes of mutations, as in (**C**), only using an effective viral population size of $N = 100$.

Our stochastic within-host evolution model recapitulates the general patterns observed in simulations of the deterministic model, with demographic stochasticity playing a more pronounced role at lower effective viral population sizes, as expected (Figure 1C,D).

3.2. Statistical Estimation of Variant Fitness Using the Deterministic Within-Host Model

3.2.1. Statistical Inference with Simulated Data

We first aimed to determine if longitudinal allele frequency data could be used to infer variant fitness in the context of cellular coinfection under the assumption of deterministic within-host evolutionary dynamics. We therefore first generated a mock dataset by forward simulating the deterministic model and adding measurement noise (Figure 2A). Prior to applying the MCMC methods described above to this mock dataset, we assessed the identifiability of the two parameters of greatest biological interest: variant fitness e^{σ_m} and mean cellular mulitiplicity of infection M. We did this by setting the magnitude of measurement noise ν and the initial mutant allele frequency $q^m(t_g = 0)$ to their true values and plotting the model likelihood over a range of MOIs and over a range of variant fitnesses. Our results indicate that there is a likelihood 'ridge' from low MOI-low fitness parameter combinations to high MOI-high fitness parameter combinations (Figure 2B). The presence of this likelihood ridge is expected, given that higher variant fitness in the context of higher MOI compensates for the phenotypic hiding phenomenon that does not occur at lower MOI.
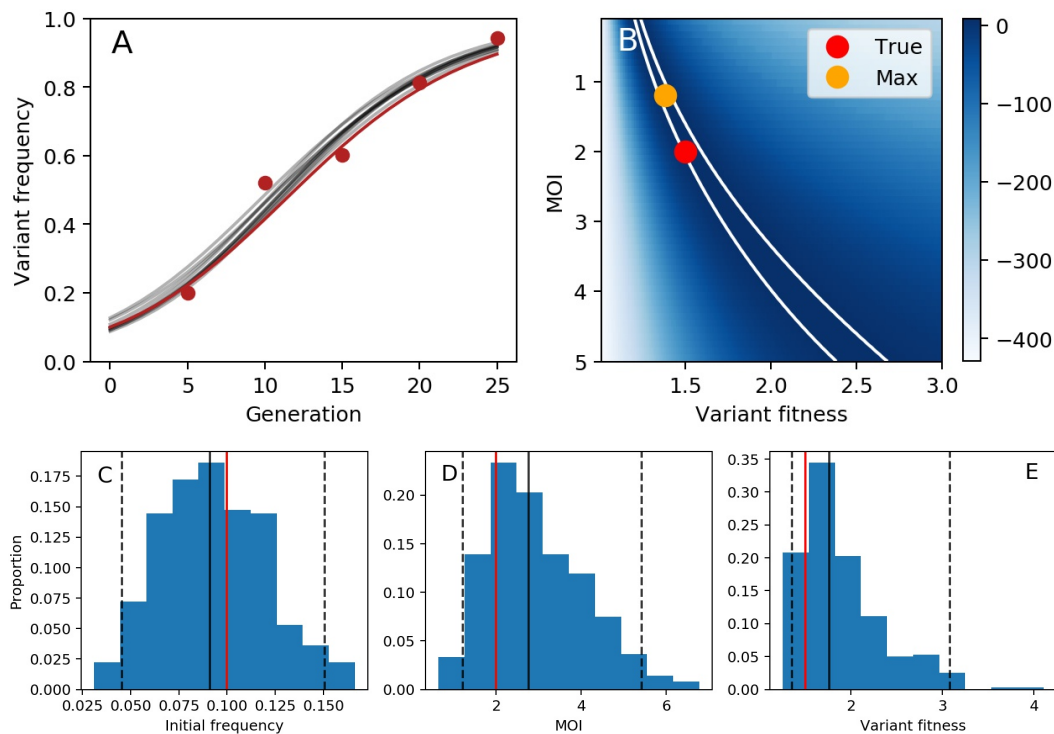
Figure 2. Variant fitness estimation under the assumption of deterministic evolutionary dynamics. (**A**) Mock data (red dots) generated from a forward simulation of the deterministic within-host evolution model with added measurement noise. The underlying deterministic dynamics are shown with a red line. The model is parameterized with variant fitness of $e^{\sigma_m} = 1.5$, a mean cellular MOI of $M = 2.0$, and an initial frequency of the variant of $q^m(t_0) = 0.10$. Measurement (observation) noise is set to $\nu = 100$. Grey lines show 10 model simulations, with parameters drawn from the MCMC posterior distributions. (**B**) Log-likelihood landscape, showing the log-likelihood of the model over a broad range of MOI and variant fitness values. When calculating these likelihoods, the initial frequency of the variant and the measurement noise were fixed at their true values. The red dot shows the true set of parameters used to simulate the mock data. The yellow dot shows the parameter combination yielding the highest log-likelihood. White boundary lines show the 95% confidence interval of parameter estimates. (**C**) Posterior distribution for the initial frequency of the variant. (**D**) Posterior distribution for the mean cellular multiplicity of infection M. (**E**) Posterior distribution for variant fitness. In (**C**–**E**), black solid lines show the median values of the posterior density, black dashed lines show the 95% credible intervals, and red solid lines show the true values.

Given this likelihood ridge, it would be difficult to use MCMC to obtain posterior distributions of the model parameters without an informative prior on either variant fitness or MOI. We decided, for the sake of illustration, to adopt a prior on MOI. Specifically, we assumed a lognormal prior on MOI, with a mean of $log(2)$ and a standard deviation of 0.5. We ran the MCMC chain for 20,000 iterations (Figure S1). Posterior distributions for the initial frequency of the variant, MOI, and variant fitness are shown in Figure 2C–E. All true parameters fell within the 95% credible intervals of the estimated parameter values. In Figure 2A, we further plot 10 forward simulations, parameterized with draws from the posterior distributions, alongside the mock data. These results indicate that the deterministic within-host evolution model can be successfully interfaced with longitudinal variant allele frequency data to infer model parameters using MCMC.

3.2.2. Statistical Inference with Experimental H5N1 Challenge Study

We now apply the same MCMC approaches to experimental data from an influenza A subtype H5N1 challenge study performed in ferrets. Figure 3A shows the frequencies of the G788A variant that was present in the inoculum stock at a frequency of 4.40% and increased in all four of the experimentally infected ferrets. For the reasons provided above, we used only days 1 and 3 for estimation of variant fitness. We also used the measured stock frequency of 4.40% as the day 0 data point for all ferrets. While technically the stock frequency and the ferrets' day 0 data points constitute very different samples, we felt comfortable with this assumption because of the likely very large transmission bottleneck size between the inoculum and index ferrets. Although an estimate of this transmission bottleneck size is not reported on in [23], a study using barcoded virus found that three-quarters of viral barcodes present in the inoculum were transmitted to index (donor) ferrets in experimental challenges that used 10^4 plaque-forming units (p.f.u.) of virus inoculum [27], which is two orders of magnitude less virus than used in [23]. In the barcoded virus study, some of the barcodes that were transmitted had frequencies as low as 0.5% in the stock, indicating that the transmission bottleneck size was likely hundreds to thousands of virions. Under the assumption of random sampling of virions from the stock, this means that the frequency of G788A on day 0 of the ferrets was likely very close to 4.40%, with measurement noise significantly outweighing any noise stemming from the wide transmission bottleneck. Indeed, calculations involving the binomial distribution (for the transmission bottleneck) and the beta distribution (for measurement noise) indicate that measurement noise dominates transmission bottleneck process noise when the bottleneck size is larger than the measurement noise parameter ν. With a bottleneck size in the hundreds to thousands and the value of ν we use for this dataset (see below), measurement noise is much larger than transmission bottleneck size noise, therefore allowing us to make the assumption that the day 0 allele frequencies of G788A in the ferrets is equal to the stock frequency of G788A.

In fitting our model to these data, we first converted days post inoculation to viral generations by assuming an 8 h influenza virus generation time based on [28]. Replicate samples for this experiment were not available, so we set the degree of measurement noise ν to 100, but consider the sensitivity of our results to this value (see below). We used an informative prior on the mean cellular MOI, specifically a lognormal prior with a mean of $log(4)$ and a standard deviation of 0.4. We used this prior based on studies that indicate that 3–4 virions are generally required to yield progeny virus from an infected cell [11]. However, we note that a wide range of estimates exist in the literature on the extent of viral complementation required for successful influenza virus progeny production, with findings indicating that this depends on the host cell type and on the viral strain considered [10,12]. We ran the MCMC chain for 20,000 iterations (Figure S2). Posterior distributions for mean cellular MOI and variant fitness are shown in Figure 3B,C, respectively. The joint density plot of MOI and variant fitness (Figure 3D) indicates that there is a positive correlation between these two parameters, consistent with our findings on simulated data (Figure 2B).

Posterior distributions for the initial frequencies of the variant in each ferret are shown in Figure S3.
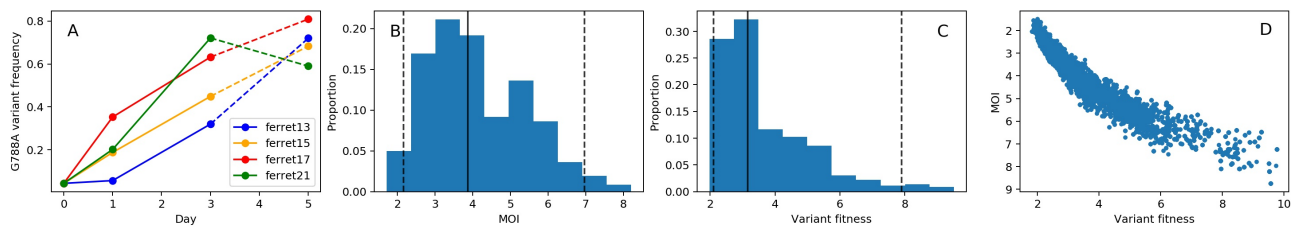
Figure 3. Fitness estimation for variant G788A, assuming deterministic within-host dynamics. (**A**) Measured G788A allele frequencies over the course of infection for 4 experimentally infected ferrets. Days 0 (stock frequency), 1, and 3 are used in the estimation of variant fitness. (**B**) Posterior distribution for the mean cellular multiplicity of infection. (**C**) Posterior distribution for variant fitness. In (**B**,**C**), black solid lines show the median values of the posterior densities and black dashed lines show the 95% credible intervals. (**D**) Joint density plot for MOI and variant fitness.

The results shown in Figure 3B indicate that cellular MOI is relatively high, although the informative prior used played a large role in shaping this parameter's posterior distribution. Our estimate of variant fitness (relative to wild-type fitness) lies between 2.11 and 7.91, with a median value of 3.15. This stands in stark contrast to a previous fitness estimate for this variant of approximately $e^{0.35} = 1.42$ [9]. However, this previous estimate was based on a model that did not consider cellular coinfection. With high levels of coinfection thought to occur in within-host influenza virus infections [11] and our inference of relatively high cellular MOI (Figure 3B), higher fitness was inferred for G788A to be able to account for its observed rapid rise in the context of phenotypic hiding. Indeed, the joint density plot shown in Figure 3D indicates that if we had constrained MOIs to be lower (closer in line with the estimates from [10]), our variant fitness estimates would have been considerably closer to those previously inferred for G788A.

Our inferred fitness estimate of ~2–8 for G788A may initially seem unreasonably large. However, several studies that have estimated variant fitness using in vitro experiments have arrived at estimates of similar magnitude. For example, a recent in vitro study of dengue virus evolution performed at low MOI found that, of the beneficial mutations that were identified, some had relative fitness effects exceeding 2 [29]. An in vitro study focused on HIV similarly found that beneficial mutations could have pronounced effects on viral fitness, with the largest estimated relative fitness of a single mutation being 6.6 [30]. These studies show that the fitness effects of viral mutations can be quite high, particularly when under strong selection pressure. While our relative fitness estimate of ~2–8 for G788A falls in the range of other estimates present in the viral literature, there are also studies that have inferred lower fitness values for beneficial mutations. For example, the highest relative fitness value estimated for an influenza B mutation that conferred resistance to a neuraminidase inhibitor was 1.8 [31].

The results presented in Figure 3 assume measurement noise ν of 100 and a viral generation time of 8 h. To ascertain the effects of these assumptions on our results, we first re-estimated MOI, variant fitness, and initial variant frequencies under the assumption of both higher ($\nu = 25$) and lower ($\nu = 400$) levels of measurement noise (Figures S4 and S5). With higher levels of measurement noise, 95% credible interval ranges for MOI and variant fitness were both wider than when measurement noise was set to $\nu = 100$. In contrast, with lower measurement noise, 95% credible interval ranges for MOI and variant fitness were both considerably more narrow than when measurement noise was set to $\nu = 100$, with variant fitness estimates falling in the range of 2.25–3.6. At both higher and lower levels of measurement noise, median estimates for MOI and variant fitness were not considerably impacted. We also considered the sensitivity of our results to the viral generation time assumed (Figures S6 and S7). With a shorter generation time of 6 h, the posterior distribution for MOI remained similar to one inferred using a viral generation time of 8 h.

However, variant fitness estimates were lower, with the 95% credible interval range of 1.66–3.47 and a median value of 2.36. With a longer generation time of 12 h, the posterior distribution for MOI again remained similar to one inferred using a viral generation time of 8 h. Variant fitness estimates using a 12 h viral generation time were considerably higher, however, with the 95% credible interval range of 2.88–9.31 and a median value of 4.58. These results underscore the importance of accurately parameterizing the viral generation time when performing variant fitness estimation.

In Figure 4, we show 10 forward simulations of the deterministic model, parameterized using draws from the posterior distributions. These indicate that the model, simulated using parameter estimates inferred from MCMC, reproduces observed G788A allele frequency patterns on days 0, 1, and 3 (the days included in the statistical analyses). The model, however, significantly over-predicts G788A frequencies on day 5 in ferret 15 and ferret 21 (Figure 4B,D). It is interesting to note that in both ferrets 15 and 21, one additional variant (G738A) rose to high frequencies between days 3 and 5. Previous work has inferred a large relative fitness value for this variant ($e^{0.9} = 2.5$) as well as (slightly negative) epistatic interactions between it and G788A [9]. Haplotype reconstruction indicates that the 'A' allele at site 738 arose in the genetic background of the 'G' allele at site 788 [9,23]. With the 'A' allele at site 738 conferring a large fitness advantage, and its genetic linkage to the 'G' allele at site 788, we would anticipate that this mutation would slow or even reverse the rise of variant G788A between days 3 and 5 in these ferrets due to this process of clonal interference. Indeed, our model projections significantly overestimate the frequency of G788A on day 5 in both of these ferrets, indicating that selection efficiently acted on G738A, impeding the projected increase in the frequency of G788A between days 3 and 5. It is also interesting to examine the dynamics of additional variants in ferrets 13 and 17, where the model predicts G788A frequencies relatively well on day 5, although this data point was not used during model fitting. Ferret 13 had one other variant arising between day 3 and day 5 (variant G496T). A previous study using these data inferred a large relative fitness value for this variant ($e^{0.7} = 2.0$) [9]. Our model simulations, however, projected the allele frequency of G788A on day 5 well in the absence of considering this variant. As such, we would predict that this G496T variant had lower relative fitness than previously estimated. Ferret 17 also had one other variant rising to high frequencies between day 3 and day 5 (variant C736A). It is unclear whether previous work inferred this mutation to be strongly beneficial or strongly deleterious, since A736C (rather than C736A) was the mutation identified as being under positive selection. Regardless, our model slightly over-projects the frequency of G788A on day 5, such that we expect C736A to have contributed to some extent to allele frequency changes of G788A through linkage effects.
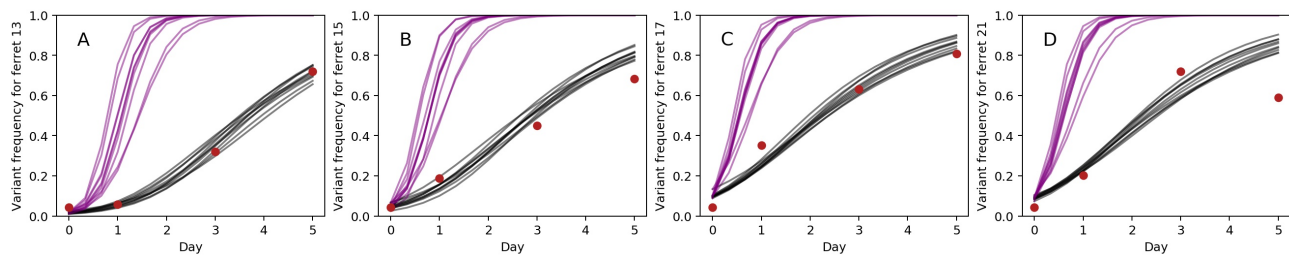
Figure 4. Deterministic model simulations (grey lines) and observed data points (red dots) are shown for (**A**) ferret 13, (**B**) ferret 15, (**C**) ferret 17, and (**D**) ferret 21. Only days 0, 1, and 3 were used in model fitting. Parameters for the model simulations were drawn from the posterior distributions of the parameters. Purple lines show model simulations under the same parameterizations of variant fitness and initial variant frequencies as the grey lines, but simulated in the absence of cellular coinfection. These no-coinfection projections were simulated using Equation (1).

In Figure 4, we further plot model simulations that assume no cellular coinfection. Specifically, we simulate Equation (1) where the dynamics are driven by the variant's individual-level fitness e^{σ_m} rather than by $\overline{e^{\sigma_m}}$. The frequency of G788A rises consid-

erably faster in these simulations compared to those that incorporate cellular coinfection. This indicates that the speed of within-host viral adaptation is severely reduced by cellular coinfection.

3.3. Statistical Estimation of Variant Fitness Using the Stochastic Within-Host Evolution Model

3.3.1. Statistical Inference with Simulated Data

The within-host evolutionary dynamics of viral pathogens may not be appropriately described by a deterministic model, even though viral population sizes within infected individuals over the course of infection are often times very large. Indeed, recent studies have highlighted the role that stochastic processes play in within-host viral dynamics [21,22]. We therefore next aimed to determine if longitudinal allele frequency data could be used to infer variant fitness in the context of cellular coinfection under a model of within-host evolution that incorporated stochastic effects. As described above, we incorporated stochastic effects by implementing the within-host model with a small effective viral population size, specified by the parameter N. As such, we are modeling demographic stochasticity, with genetic drift being the driver of random changes in variant allele frequencies. We generated a mock within-host dataset by forward-simulating the stochastic model and adding measurement noise (Figure 5A). This dataset was generated under the same parameterization as the deterministic dataset shown in Figure 2A, with stochastic effects included by setting the viral population size N to 100.
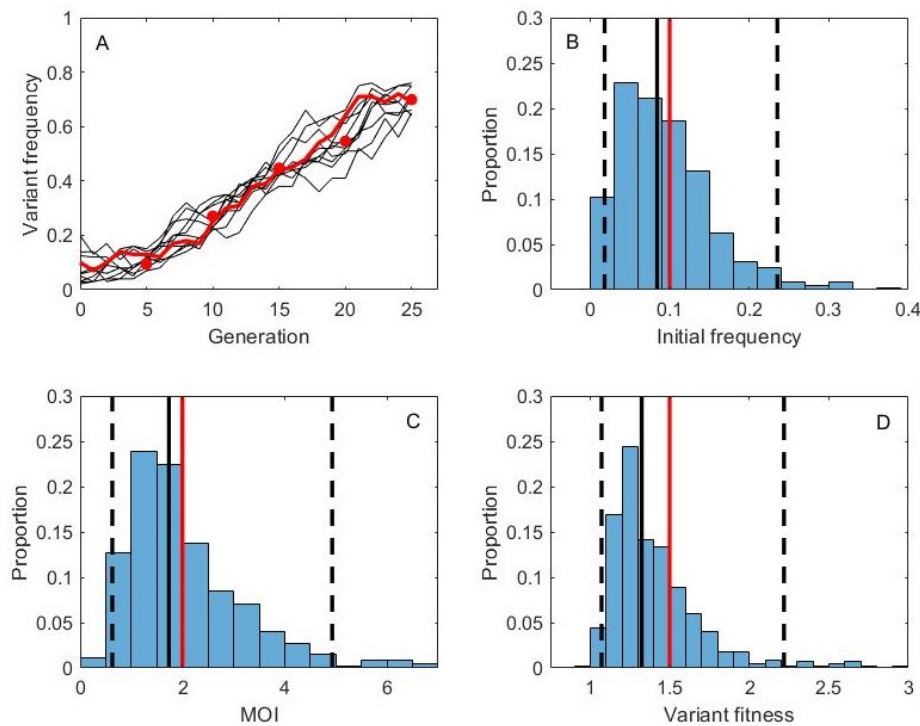
Figure 5. Variant fitness estimation under the assumption of stochastic evolutionary dynamics. (**A**) Mock data (red dots) generated from a forward simulation of the stochastic within-host evolution model with added measurement noise. The underlying stochastic dynamics are shown with a red line. The model is parameterized with variant fitness of $e^{\sigma_m} = 1.5$, a mean cellular MOI of $M = 2.0$, an initial frequency of the variant of $q^m(t_0) = 0.10$. Measurement (observation) noise is set to $\nu = 100$. The viral effective population size is set to $N = 100$. Grey lines show the dynamics of 10 reconstructed allele frequency trajectories. These trajectories are unobserved state variables that have been reconstructed using pMCMC. (**B**) Posterior distribution for the initial frequency of the variant. (**C**) Posterior distribution for the mean cellular multiplicity of infection M. (**D**) Posterior distribution for variant fitness. In (**B**–**D**), black solid lines show the median values of the posterior densities, black dashed lines show the 95% credible intervals, and red solid lines show the true values. 200 particles were used in the pMCMC.

Using the same prior on MOI as with the deterministic analysis and under the assumption that ν and N are known, we ran the MCMC chain for 50,000 iterations (Figure S8). Posterior distributions for the initial frequency of the variant, mean cellular MOI, and variant fitness are shown in Figure 5B–D. All true parameters fell within the 95% credible intervals of the estimated parameter values. In Figure 5A, we plot 10 reconstructed variant allele frequency trajectories. These results indicate that the stochastic within-host evolution model can be successfully interfaced with longitudinal variant allele frequency data to infer model parameters and underlying variant frequency dynamics using pMCMC.

3.3.2. Statistical Inference with Experimental H5N1 Challenge Study Data

We now apply the same pMCMC approaches to the H5N1 experimental data analyzed already using the deterministic model. We again used only days 0, 1, and 3 for estimation of variant fitness, assumed a viral generation time of 8 h, and set the degree of measurement noise ν to 100. We used the same informative prior on the mean cellular multiplicity of infection M. We set the effective viral population size to $N = 100$ in our analyses, but consider a scenario of even higher stochasticity below. We ran the pMCMC chain for 50,000 iterations (Figure S9). Posterior distributions for mean cellular MOI and variant fitness are shown in Figure 6A,B, respectively. The joint density plot of MOI and variant fitness (Figure S10) again indicates that there is a positive correlation between these parameters, consistent with the results from our analysis using the deterministic model. Posterior distributions for the initial frequencies of the variant in each ferret are shown in Figure S11. Our results are consistent with the findings from our deterministic analysis: we estimate that the fitness of the G788A variant is considerably (2–10.5 times) higher than that of the wild-type virus. These results are robust to higher levels of stochasticity; we show, for example, the posterior distributions for M and variant fitness under the assumption that the viral effective population size N is 40 (Figure S12).
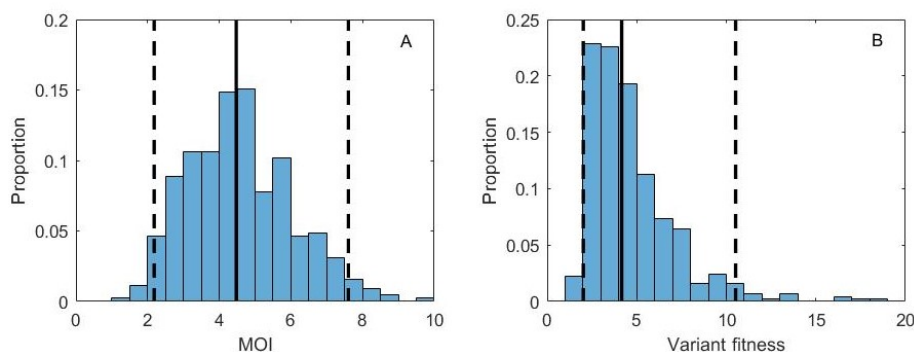
Figure 6. Fitness estimation for variant G788A, assuming stochastic within-host dynamics. (**A**) Posterior distribution for the mean cellular multiplicity of infection M. (**B**) Posterior distribution for variant fitness. In (**A,B**) the model was parameterized with an effective viral population size of $N = 100$. In (**A,B**) black solid lines show the median values of the posterior densities and black dashed lines show the 95% credible intervals.

4. Discussion

Here, we developed mathematical within-host models that can take into consideration cellular coinfection when projecting changes in viral allele frequencies over the course of an infection. We further described and demonstrated how these evolutionary models can be statistically interfaced with viral sequence data to jointly estimate variant fitness relative to the wild-type allele along with the mean cellular multiplicity of infection. Our results indicate that ignoring the possibility of cellular coinfection can result in significant underestimation of a variant's selective advantage. This is important because a variant with a much higher selective advantage, once established monomorphically within a host, is expected to have a more precipitous impact on within-host viral dynamics than a variant with a smaller selective advantage. We might, for example, expect a variant with

a higher selective advantage to result in higher peak viral loads and potentially longer durations of infection. This would impact both symptom development as well as onward transmission potential.

Our models, like all models, make some simplifying assumptions. First, we assume low viral diversity, with diversity comprising just one locus and two alleles (a wild-type and a variant allele). We chose to model evolution at a single locus to highlight the important contribution that cellular coinfection may play in the within-host evolution of viral pathogens. Our application to the G788A mutation in the H5N1 experimental challenge study in ferrets satisfied this assumption between days 0 through 3. Because other sites became polymorphic in each of the four studied ferrets by day 5, we excluded this time point from our statistical analyses. To consider the effect of cellular coinfection within a system with higher levels of genetic diversity, and the possibility of new variants arising over the course of infection, the models developed here should be extended using approaches developed already in [9]. These approaches include inference of viral haplotypes and the incorporation of de novo mutations into the presented model structures. With these additions, full genetic linkage between loci can be considered, and epistatic interactions between loci can also be inferred. Our models, as presented here, however, could still be applied to higher diversity viral systems if recombination occurred freely between loci, as may be the case between influenza gene segments or some viruses with high recombination rates.

A second assumption present in the current formulation of our models is that viral fitness is additive: if a coinfected cell harbors both variant and wild-type viral genomes, then the fitness of each viral genome is not only assumed to be equal, but also equal to the arithmetic mean fitness of the involved genomes. This may be a good assumption if the focal mutation impacts, for example, polymerase activity, with the viral polymerase protein being used for the replication of all viral genomes. However, it may also be the case that a mutation has a disproportionate effect on intracellular viral fitness. Future work should therefore examine the impact of a mutation's 'dominance' [32] on in vivo viral evolution.

A third assumption is one that is somewhat less transparent in the structure of our models, namely that we assume that there is no intracellular viral competition for host cell machinery. This assumption is reflected in the calculation of a variant allele's mean fitness ($\overline{e^{\sigma_m}}$). A single viral genome's fitness in a cell depends on the genotypes of the other genomes present in the cell, but not on the cellular multiplicity of infection directly. If a variant genome is in a cell alone or with a large number of other variant genomes, for example, its fitness will be the same. However, if host cell machinery is limiting, one would expect the per genome fitness—which can be interpreted here as *per capita* viral yield or reproductive success—to be lower in highly coinfected cells. Indeed, empirical studies with influenza virus indicates that there is a saturating relationship between viral input and viral output from a cell [33]: at low cellular MOI, doubling the viral input yields a doubling of viral output, such that viral competition is not readily apparent; at high MOI, however, doubling the viral input does not appreciably change the overall viral output, indicative of limiting host cell machinery. Future work should therefore also examine the impact of intracellular viral competition on within-host viral evolution and extend models such as the ones we presented here to account for intracellular viral competition.

Finally, our model assumes that the mean cellular multiplicity of infection (MOI) is fixed across viral generations and that virion entry into cells is governed by a Poisson process. In terms of the former assumption, it is conceivable that MOI might change over the course of an infection. For example, at the beginning of a viral infection, MOI may be low because a very small viral population is initiating infection in a large environment of host cells. As viruses replicate within their host, viral population sizes increase and the number of target cells decreases. This may result in more individual-level selection at the beginning of the infection (due to low MOI), followed by a greater degree of phenotypic hiding later on in the infection (due to higher MOI). To accommodate these changes in MOI, the structures of the within-host models presented here would not need to be significantly

altered; MOI could simply be made into a time-varying parameter. For simplicity, we here instead decided to assume that MOI is fixed over the course of infection, in part because of the lack of empirical data to inform MOI at multiple time points over the course of an infection. A further argument against incorporating dynamic changes in MOI is that spatially structured within-host viral dynamics, such as those characterized for influenza [34], may result in cellular MOIs that are more uniform over time than expected from a spatially unstructured setting. In terms of the latter assumption (Poisson-distributed virions), there are several reasons why this assumption may not be met. Virions could aggregate, such that virion entry into cells is not an independent process. Cells could also be heterogeneous with respect to their susceptibility to infection, for example due to their cell cycle state or due to antiviral states triggered by interferon. Both of these factors would result in virions being overdispersed across cells, rather than Poisson-distributed. While considering different assumptions of how virions are distributed across cells is beyond the scope of this study, future work should address the effect of viral overdispersion on variant fitness estimation.

Despite these limiting assumptions, a general takeaway from the evolutionary models presented here is that cellular coinfection will slow down the rate of viral adaptation within hosts when adaptation occurs through selection acting on single point mutations (or insertions/deletions) as we considered here. (A caveat here is that cellular coinfection could accelerate viral adaptation if it heavily relies on genetic exchange, i.e., recombination or reassortment.) Slower rates of viral adaptation is good news from the perspective of the host population, as this will also slow down viral adaptation at the population-level. This finding has clear implications for emerging zoonotic viruses that are adapting to a new host population. Analogously, cellular coinfection will result in less effective purging of deleterious mutations. By making natural selection a weaker evolutionary force, cellular coinfection may thus be one reason why stochastic processes appear to dominate within-host viral dynamics and why selection does not seem to act efficiently over the course of an acute infection for viruses such as seasonal influenza [21,35]. There are other factors, however, that may also limit the ability for positive selection to act efficiently within hosts. For example, the temporal asynchrony between the timing of the immune response and when virus diversification occurs may explain why antigenic immune escape variants do not readily arise in individuals with some pre-existing immunity [36]. A second takeaway is that variants whose fitness levels (relative to wild-type) have been quantified using models that do not include cellular coinfection may have significantly underestimated variant fitness. Underestimation of variant fitness may underestimate the effect of a mutation on viral replication dynamics once those dynamics involve only the variant virus. Our results—that the fitness effect of certain mutations can be large—speak to the adaptive potential of these viruses to new or changing host populations, even if adaptation may occur more slowly than might be expected.

Supplementary Materials: The following are available online at https://www.mdpi.com/article/10.3390/v13071216/s1: Figure S1: MCMC trace plots for parameters estimated by interfacing the deterministic within-host model with the simulated data. Figure S2: MCMC trace plots for parameters estimated by interfacing the deterministic within-host model with the influenza H5N1 experimental challenge study data. Figure S3: Posterior distributions of initial G788A frequencies from fitting the deterministic model. Figure S4: Parameter estimation for variant G788A, assuming deterministic within-host dynamics and a larger amount of measurement noise. Figure S5: Parameter estimation for variant G788A, assuming deterministic within-host dynamics and a smaller amount of measurement noise. Figure S6: Parameter estimation for variant G788A, assuming deterministic within-host dynamics and a viral generation time of 6 hours. Figure S7: Parameter estimation for variant G788A, assuming deterministic within-host dynamics and a viral generation time of 12 hours. Figure S8: MCMC trace plots for parameters estimated by interfacing the stochastic within-host model with the simulated data. Figure S9: MCMC trace plots for parameters estimated by interfacing the stochastic within-host model with the influenza H5N1 experimental challenge study data. Figure S10: Joint density of MOI versus variant fitness for the stochastic model fit to the influenza H5N1 experimental

challenge study data. Figure S11: Posterior distributions of initial G788A frequencies from fitting the stochastic within-host model. Figure S12: Fitness estimation for variant G788A, assuming stochastic within-host dynamics, parameterized with an effective viral population size of $N = 40$.

References

1. Antia, R.; Regoes, R.R.; Koella, J.C.; Bergstrom, C.T. The role of evolution in the emergence of infectious diseases. *Nature* **2003**, *426*, 658–661. [CrossRef]
2. Matrosovich, M.; Tuzikov, A.; Bovin, N.; Gambaryan, A.; Klimov, A.; Castrucci, M.R.; Donatelli, I.; Kawaoka, Y. Early alterations of the receptor-binding properties of H1, H2, and H3 avian influenza virus hemagglutinins after their introduction into mammals. *J. Virol.* **2000**, *74*, 8502–8512. [CrossRef] [PubMed]
3. Su, Y.C.; Bahl, J.; Joseph, U.; Butt, K.M.; Peck, H.A.; Koay, E.S.; Oon, L.L.; Barr, I.G.; Vijaykrishna, D.; Smith, G.J. Phylodynamics of H1N1/2009 influenza reveals the transition from host adaptation to immune-driven selection. *Nat. Commun.* **2015**, *6*, 7952. [CrossRef] [PubMed]
4. Volz, E.; Hill, V.; McCrone, J.T.; Price, A.; Jorgensen, D.; O'Toole, Á.; Southgate, J.; Johnson, R.; Jackson, B.; Nascimento, F.F.; et al. Evaluating the effects of SARS-CoV-2 Spike mutation D614G on transmissibility and pathogenicity. *Cell* **2021**, *184*, 64–75. [CrossRef]
5. Herfst, S.; Schrauwen, E.J.; Linster, M.; Chutinimitkul, S.; de Wit, E.; Munster, V.J.; Sorrell, E.M.; Bestebroer, T.M.; Burke, D.F.; Smith, D.J.; et al. Airborne transmission of influenza A/H5N1 virus between ferrets. *Science* **2012**, *336*, 1534–1541. [CrossRef] [PubMed]
6. Imai, M.; Watanabe, T.; Hatta, M.; Das, S.C.; Ozawa, M.; Shinya, K.; Zhong, G.; Hanson, A.; Katsura, H.; Watanabe, S.; et al. Experimental adaptation of an influenza H5 HA confers respiratory droplet transmission to a reassortant H5 HA/H1N1 virus in ferrets. *Nature* **2012**, *486*, 420–428. [CrossRef] [PubMed]
7. Holland, J.J.; De La Torre, J.C.; Clarke, D.; Duarte, E. Quantitation of relative fitness and great adaptability of clonal populations of RNA viruses. *J. Virol.* **1991**, *65*, 2960–2967. [CrossRef]
8. Ganusov, V.V.; Goonetilleke, N.; Liu, M.K.; Ferrari, G.; Shaw, G.M.; McMichael, A.J.; Borrow, P.; Korber, B.T.; Perelson, A.S. Fitness costs and diversity of the (cytotoxic T lymphocyte (CTL)) response determine the rate of (CTL) escape during acute and chronic phases of (HIV) infection. *J. Virol.* **2011**, *85*, 10518–10528. [CrossRef]
9. Illingworth, C.J. Fitness inference from short-read data: Within-host evolution of a reassortant H5N1 influenza virus. *Mol. Biol. Evol.* **2015**, *32*, 3012–3026. [CrossRef] [PubMed]
10. Brooke, C.B.; Ince, W.L.; Wrammert, J.; Ahmed, R.; Wilson, P.C.; Bennink, J.R.; Yewdell, J.W. Most influenza A virions fail to express at least one essential viral protein. *J. Virol.* **2013**, *87*, 3155–3162. [CrossRef]
11. Jacobs, N.T.; Onuoha, N.O.; Antia, A.; Steel, J.; Antia, R.; Lowen, A.C. Incomplete influenza A virus genomes occur frequently but are readily complemented during localized viral spread. *Nat. Commun.* **2019**, *10*, 3526. [CrossRef] [PubMed]

12. Phipps, K.L.; Ganti, K.; Jacobs, N.T.; Lee, C.Y.; Carnaccini, S.; White, M.C.; Manandhar, M.; Pickett, B.E.; Tan, G.S.; Ferreri, L.M.; et al. Collective interactions augment influenza A virus replication in a host-dependent manner. *Nat. Microbiol.* **2020**, *5*, 1158–1169. [CrossRef]

13. Shriner, D.; Rodrigo, A.G.; Nickle, D.C.; Mullins, J.I. Pervasive genomic recombination of HIV-1 in vivo. *Genetics* **2004**, *167*, 1573–1583. [CrossRef]

14. Neher, R.A.; Leitner, T. Recombination rate and selection strength in HIV intra-patient evolution. *PLoS Comput. Biol.* **2010**, *6*, e1000660. [CrossRef]

15. Wilke, C.O.; Novella, I.S. Phenotypic mixing and hiding may contribute to memory in viral quasispecies. *BMC Microbiol.* **2003**, *3*, 11. [CrossRef]

16. Zavada, J. Viral pseudotypes and phenotypic mixing. *Arch. Virol.* **1976**, *50*, 1–15. [CrossRef]

17. Froissart, R.; Wilke, C.O.; Montville, R.; Remold, S.K.; Chao, L.; Turner, P.E. Co-infection weakens selection against epistatic mutations in RNA viruses. *Genetics* **2004**, *168*, 9–19. [CrossRef]

18. Wodarz, D.; Levy, D.N.; Komarova, N.L. Multiple infection of cells changes the dynamics of basic viral evolutionary processes. *Evol. Lett.* **2019**, *3*, 104–115. [CrossRef]

19. Acevedo, A.; Brodsky, L.; Andino, R. Mutational and fitness landscapes of an RNA virus revealed through population sequencing. *Nature* **2014**, *505*, 686–690. [CrossRef] [PubMed]

20. Foll, M.; Shim, H.; Jensen, J.D. WFABC: A Wright–Fisher ABC-based approach for inferring effective population sizes and selection coefficients from time-sampled data. *Mol. Ecol. Resour.* **2015**, *15*, 87–98. [CrossRef] [PubMed]

21. McCrone, J.T.; Woods, R.J.; Martin, E.T.; Malosh, R.E.; Monto, A.S.; Lauring, A.S. Stochastic processes constrain the within and between host evolution of influenza virus. *Elife* **2018**, *7*, e35962. [CrossRef]

22. McCrone, J.T.; Woods, R.J.; Martin, E.T.; Monto, A.S.; Lauring, A.S. The effective population size and mutation rate of influenza A virus in acutely infected individuals. *bioRxiv* **2020**. [CrossRef]

23. Wilker, P.R.; Dinis, J.M.; Starrett, G.; Imai, M.; Hatta, M.; Nelson, C.W.; O'Connor, D.H.; Hughes, A.L.; Neumann, G.; Kawaoka, Y.; et al. Selection on haemagglutinin imposes a bottleneck during mammalian transmission of reassortant H5N1 influenza viruses. *Nat. Commun.* **2013**, *4*, 2636. [CrossRef]

24. Andrieu, C.; Doucet, A.; Holenstein, R. Particle Markov chain Monte Carlo methods. *J. R. Stat. Soc. Ser. B Stat. Methodol.* **2010**, *72*, 269–342. [CrossRef]

25. Rasmussen, D.A.; Ratmann, O.; Koelle, K. Inference for nonlinear epidemiological models using genealogies and time series. *PLoS Comput. Biol.* **2011**, *7*, e1002136. [CrossRef]

26. Endo, A.; van Leeuwen, E.; Baguelin, M. Introduction to particle Markov-chain Monte Carlo for disease dynamics modellers. *Epidemics* **2019**, *29*, 100363. [CrossRef]

27. Varble, A.; Albrecht, R.A.; Backes, S.; Crumiller, M.; Bouvier, N.M.; Sachs, D.; García-Sastre, A. Influenza A virus transmission bottlenecks are defined by infection route and recipient host. *Cell Host Microbe* **2014**, *16*, 691–700. [CrossRef]

28. Dou, D.; Hernández-Neuta, I.; Wang, H.; Östbye, H.; Qian, X.; Thiele, S.; Resa-Infante, P.; Kouassi, N.M.; Sender, V.; Hentrich, K.; et al. Analysis of IAV replication and co-infection dynamics by a versatile RNA viral genome labeling method. *Cell Rep.* **2017**, *20*, 251–263. [CrossRef]

29. Dolan, P.T.; Taguwa, S.; Rangel, M.A.; Acevedo, A.; Hagai, T.; Andino, R.; Frydman, J. Principles of dengue virus evolvability derived from genotype-fitness maps in human and mosquito cells. *Elife* **2021**, *10*, e61921. [CrossRef]

30. Da Silva, J.; Coetzer, M.; Nedellec, R.; Pastore, C.; Mosier, D.E. Fitness epistasis and constraints on adaptation in a human immunodeficiency virus type 1 protein region. *Genetics* **2010**, *185*, 293–303. [CrossRef]

31. Burnham, A.J.; Armstrong, J.; Lowen, A.C.; Webster, R.G.; Govorkova, E.A. Competitive fitness of influenza B viruses with neuraminidase inhibitor-resistant substitutions in a coinfection model of the human airway epithelium. *J. Virol.* **2015**, *89*, 4575–4587. [CrossRef] [PubMed]

32. Bushman, M.; Antia, R. A general framework for modelling the impact of co-infections on pathogen evolution. *J. R. Soc. Interface* **2019**, *16*, 20190165. [CrossRef]

33. Martin, B.E.; Harris, J.D.; Sun, J.; Koelle, K.; Brooke, C.B. Cellular co-infection can modulate the efficiency of influenza A virus production and shape the interferon response. *PLoS Pathog.* **2020**, *16*, e1008974. [CrossRef] [PubMed]

34. Gallagher, M.E.; Brooke, C.B.; Ke, R.; Koelle, K. Causes and consequences of spatial within-host viral spread. *Viruses* **2018**, *10*, 627. [CrossRef]

35. Dinis, J.M.; Florek, N.W.; Fatola, O.O.; Moncla, L.H.; Mutschler, J.P.; Charlier, O.K.; Meece, J.K.; Belongia, E.A.; Friedrich, T.C. Deep sequencing reveals potential antigenic variants at low frequencies in influenza A virus-infected humans. *J. Virol.* **2016**, *90*, 3355–3365. [CrossRef] [PubMed]

36. Morris, D.H.; Petrova, V.N.; Rossine, F.W.; Parker, E.; Grenfell, B.T.; Neher, R.A.; Levin, S.A.; Russell, C.A. Asynchrony between virus diversity and antibody selection limits influenza virus evolution. *Elife* **2020**, *9*, e62105. [CrossRef]

Chapter 4

Detecting intra-patient single nucleotide variants of SARS-CoV-2 in chronically infected immunocompromised patients

The following chapter is a publication recently accepted in the New England Journal of Medicine. While there are experiments presented here, my contributions were centered around analyzing the sequencing data that was collected from immunocompromised patients infected with SARS-CoV-2. Specifically, we detected minor variants circulating in these patients, some of which have been implicated in immune escape.

SARS-CoV-2 evolution and immune escape in immunocompromised patients treated with exogenous antibodies

Authors:
Erin M. Scherer, Ph.D., D.Phil.[1,2], Ahmed Babiker, M.B.B.S.[1,3], Max W. Adelman, M.D.[1], Brent Allman, B.A.[4], Autum Key, M.S.[3], Jennifer M. Kleinhenz, B.S.[2,5], Rose M. Langsjoen, Ph.D.[3], Phuong-Vi Nguyen[1], Ivy Onyechi, M.S.[6], Jacob D. Sherman, B.S.[1,2], Trevor W. Simon, M.S.[1,2], Hannah Soloff[7], Jessica Tarabay, M.P.H.[8], Jay Varkey, M.D.[1], Andrew S. Webster, M.D.[1], Daniela Weiskopf, Ph.D.[9], Daniel B. Weissman, Ph.D.[10,11], Yongxian Xu, M.D.[1,2], Jesse J. Waggoner, M.D.[1], Katia Koelle, Ph.D.[11], Nadine Rouphael, M.D.[1,2], Stephanie M. Pouch, M.D., M.S.[1], Anne Piantadosi, M.D., Ph.D.[1,3]

Affiliations:
[1]Division of Infectious Diseases, Department of Medicine, Emory University School of Medicine, Atlanta, GA, USA
[2]Hope Clinic of the Emory Vaccine Center, Emory University School of Medicine, Decatur, GA, USA
[3]Department of Pathology and Laboratory Medicine, Emory University School of Medicine, Atlanta, GA, USA
[4]Population Biology, Ecology, and Evolution Graduate Program, Laney Graduate School, Emory University, Atlanta, GA, USA
[5]Department of Pediatrics, Emory University School of Medicine, Atlanta, GA, USA
[6]Emory Integrated Genomics Core, Emory University, Atlanta, GA, USA
[7]Emory University, Atlanta, GA, USA
[8]Emory Healthcare
[9]Center for Infectious Disease and Vaccine Research, La Jolla Institute for Immunology, La Jolla, CA, USA
[10]Department of Physics, Emory University, Atlanta, GA, USA
[11]Department of Biology, Emory University, Atlanta, GA, USA

Corresponding Authors:
Erin M. Scherer
Division of Infectious Diseases, Department of Medicine, Emory University School of Medicine,
Hope Clinic of the Emory Vaccine Center, Emory University School of Medicine
erin.margaret.scherer@emory.edu

Anne Piantadosi
Department of Pathology and Laboratory Medicine, Emory University School of Medicine
Division of Infectious Diseases, Department of Medicine, Emory University School of Medicine
anne.piantadosi@emory.edu

Abstract

Background:

SARS-CoV-2 mutations conferring escape from neutralizing antibodies can arise in immunocompromised patients with prolonged infection, but the conditions that facilitate immune escape are still not fully understood.

Methods:

We characterized endogenous immune responses, within-host SARS-CoV-2 evolution, and autologous neutralization of the viral variants that arose in five immunocompromised patients with prolonged infection and B cell deficiencies.

Results:

In two patients treated with the monoclonal antibody bamlanivimab, viral resistance to autologous serum arose early and persisted for several months, accompanied by ongoing evolution in the spike protein. These patients exhibited deficiencies in both T and B cell arms, and one patient succumbed to disease. In contrast, we did not observe spike mutations in immunologically important regions in patients who did not receive exogenous antibodies or who received convalescent plasma and had intact T cell responses to SARS-CoV-2.

Conclusions:

Our results underscore the potential importance of multiple factors – the absence of an effective endogenous immune response, persistent virus replication, and selective pressure such as single-agent bamlanivimab – in promoting the emergence of SARS-CoV-2 mutations associated with immune evasion. These findings highlight the need for larger clinical studies in immunocompromised populations to better understand the ramifications of different therapies. Our results also confirm that patients with B cell deficiencies can elicit effector T cells and may suggest an important role for T cells in controlling infection, which is relevant to vaccines and therapeutics.

Introduction

Immunocompromised patients can develop months-long infection with SARS-CoV-2, providing opportunities for within-host virus evolution and the emergence of immune escape mutations. Prior studies have identified immunologically important mutations in SARS-CoV-2 sequences from immunocompromised patients, particularly within the spike protein, which is required for entry and is the target of currently approved vaccines. For example, spike mutations in the angiotensin converting enzyme 2 (ACE2) receptor binding motif (RBM) such as E484K and Q493K[1,2] and deletions in the spike N terminal domain (NTD)[3,4] have been identified in immunocompromised patients with prolonged infection. These mutations have been found to confer partial resistance to neutralizing antibodies[5–9] and are also are found in SARS-CoV-2 variants of concern. In part due to this, it has been hypothesized that prolonged SARS-CoV-2 infection in immunocompromised patients may contribute to the emergence of variants with global impact[10,11].

However, immunologically important mutations do not arise in all immunocompromised patients with prolonged infection, and the lack of adaptive immune responses makes it possible that an additional selective pressure is required, such as exogenous antibody treatment. Understanding conditions that promote the emergence of immunologically important SARS-CoV-2 mutations in immunocompromised patients is critically important to both guiding treatment and potentially preventing the emergence of new SARS-CoV-2 variants. Here, we investigated the interplay between exogenous antibody treatment, endogenous humoral and cellular immune responses, and within-host virus evolution in five immunocompromised patients with prolonged SARS-CoV-2 infection.

Results

Overview of clinical courses

We identified five immunocompromised patients with persistent (> 30 days) SARS-CoV-2 infection (**Table 1, Figure 1**). All had a history of underlying malignancy and four were treated with immunosuppressive regimens including rituximab, while the other patient (P4) had Good Syndrome, resulting in hypogammaglobulinemia, B-cell deficiency, and CD4/CD8 T-cell imbalance. The duration of positive PCR tests for SARS-CoV-2 ranged from 42 to 302 days from the time of first positive test (d42-d302). Patients had persistently low SARS-CoV-2 PCR cycle threshold (C_T) values throughout infection, as well as detectable subgenomic RNA (**Figure 1**). Two patients (P2 and P3) were treated with the single-agent monoclonal antibody (mAb) bamlanivimab soon after SARS-CoV-2 infection (d4 and d8, respectively). Two other patients were treated with high-titer convalescent plasma (CP): P4 at d0 and d104, and P5 at d196. Two patients (P3 and P4) received intravenous immunoglobulin (IVIG) as part of treatment for their underlying condition. All patients were treated with remdesivir and all but one (P1) were treated with steroids; there were no known changes to the patients' baseline immunosuppressive regimens. All but one patient (P2) ultimately recovered.

Detailed clinical courses
Patient 1:

This patient was a 60-69-year-old man with a history of relapsed B-cell acute lymphoblastic leukemia who underwent peripheral stem cell transplant (PBSCT) 18 months prior to his COVID-19 diagnosis. His post-PBSCT course was complicated by chronic graft-versus-host disease (GVHD) of the skin and gastrointestinal tract for which he was maintained on tacrolimus and rituximab infusions every 8 weeks. His last dose of rituximab was 9 days prior to his COVID-19 diagnosis, and he received rituximab again 47 days after his initial positive test. He initially presented with 3 days of nausea, vomiting, cough, and sore throat and was diagnosed with COVID-19 via nasopharyngeal (NP) PCR (cycle threshold [C_T] unknown). He was not hypoxemic and chest X-ray showed no acute abnormalities. He was treated symptomatically and did not receive antivirals or undergo changes in immunosuppression, and he was discharged one day after admission. His symptoms initially resolved, but he developed recurrent cough and progressive shortness of breath and presented to the emergency department for further evaluation 29 days following his previous discharge. At that time, he was hypoxemic to 84% on room air, and chest CT showed peripheral areas of ground glass opacity and changes compatible with diffuse alveolar damage. His SARS-CoV-2 NP PCR was again positive, with C_T 26. This was felt to reflect ongoing COVID-19 infection, and he received a 5-day course of remdesivir. His symptoms improved over several days and he was discharged without supplemental oxygen 10 days after admission. He had no functional limitations at follow-up 3 months after the second hospitalization.

Patient 2:

This patient was a 40-49-year-old woman diagnosed with stage IV diffuse large B-cell lymphoma 2 months prior to her COVID-19 infection, for which she had been treated with 2 cycles of R-CHOP; she last received rituximab 7 days prior to her COVID-19 diagnosis. Several days after the second cycle she developed cough and shortness of breath and was diagnosed with COVID-19 via NP PCR (C_T unknown). On day 4 of illness, she was treated with bamlanivimab and clinically improved, and she subsequently received cycle 3 of R-CHOP 17 days later. She then developed fever and progressive shortness of breath prompting readmission 7 days following cycle 3 of R-CHOP. SARS-CoV-2 NP PCR was again positive with C_T 18, and chest CT showed patchy groundglass opacities. IgG antibodies to the SARS-CoV-2 receptor binding domain were positive, and this was felt to reflect previous receipt of bamlanivimab. She was treated with 5 days of remdesivir and 10 days of dexamethasone. She was readmitted again one week later with worsening chills, shortness of breath, and hypoxemia. SARS-CoV-2 testing via NP PCR was again positive (C_T 15), and chest CT showed worsened opacities. She was treated with another 5-day course of remdesivir and steroid pulse then taper for possible organizing pneumonia. She was discharged after a 7 day hospitalization but was again admitted 7 days later for dyspnea and hypoxia to 86%. SARS-CoV-2 testing via NP PCR was positive (C_T 16), and chest CT showed progression of bilateral patchy opacities. She was continued on methylprednisolone, and her course was complicated by *Pneumocystis jirovecii* pneumonia despite prophylaxis, progressive respiratory failure requiring mechanical ventilation, CMV viremia, and renal failure. SARS-CoV-2 NP PCR obtained on day 22 of hospitalization was positive with a C_T 16, and she died on hospital day 33.

Patient 3:

This patient was a 30-39-year-old woman with prior history of myelodysplastic syndrome who had undergone matched related PBSCT 3 years prior to her COVID-19 diagnosis. Her post-transplant course was complicated by chronic GVHD of the gastrointestinal tract, skin, and eyes, as well as CMV enteritis, and she was maintained on rituximab (last dose approximately 3 months prior to COVID-19 diagnosis), mycophenolate mofetil, prednisone, and monthly intravenous immunoglobulin infusions. She tested positive for COVID-19 via NP PCR (C_T unknown) after exposure to a known case; she had no symptoms at that time and received bamlanivimab 8 days later. Approximately 2 weeks after monoclonal antibody administration, she developed shortness of breath and hypoxia requiring hospital admission. A SARS-CoV-2 NP PCR was positive (C_T unknown) and chest CT showed multifocal groundglass opacities with areas of tree-in-bud nodularity. Given concern for pulmonary GVHD, she underwent bronchoscopy with transbronchial biopsy; BAL cultures were negative, and histology was unrevealing. She did not receive any treatment for COVID-19 during that admission, and no changes were made to her immunosuppression. One week following discharge, she was readmitted for worsening shortness of breath and fever. A repeat SARS-CoV-2 NP PCR was positive (C_T 23), and chest CT showed progression of patchy peripheral bilateral opacities. She was treated with 5 days of remdesivir and 10 days of dexamethasone. Repeat NP PCR after 5 days of remdesivir was positive with C_T 19. She was discharged, initially improved, but developed worsening shortness of breath after steroids were tapered, prompting readmission 3 weeks later. SARS-CoV-2 NP PCR was again positive (C_T 23), and chest CT showed new bilateral scattered groundglass opacities. Her clinical picture and radiographic findings were felt to reflect SARS-CoV-2 related inflammatory changes, and she was discharged home on a 4-week dexamethasone taper which was converted to a maintance dose of prednisone. She did well from a pulmonary standpoint, but was readmitted three months later and again seven months later, both times with CMV enteritis. During the first of those readmissions, at 260 days after her first PCR test, a clinical lymphocyte panel showed immune deficiencies in both T and B cell arms (534 $CD3^+$ T cells/uL blood; 263 $CD4^+$ T cells/uL blood; 294 $CD8^+$ T cells/uL blood; 2 $CD19^+$ B cells uL/blood). The patient's SARS-CoV-2 NP PCR was positive on both admisssions (C_T 34 and 26), but she did not exhibit any respiratory symptoms. She continued to follow up with Infectious Diseases as an outpatient and eventually tested negative by home rapid antigen test 12 months after initial diagnosis.

Patient 4:

This patient was a 40-49-year-old man with prior history of thymoma and subsequent thymectomy who developed cough, fever, and shortness of breath and was diagnosed with COVID-19 at another institution via NP PCR (C_T unknown). At that time, he was noted to be hypoxemic and was treated for COVID-19 with convalescent plasma, remdesivir, and steroids with clinical improvement. However, approximately 2 weeks later, his symptoms worsened and he was readmitted to the same facility. At that time, he was was presumptively treated for bacterial pneumonia with antibiotics but did not receive any dedicated treatment for COVID-19, and he was discharged on

supplemental oxygen. Approximately 2 weeks later, he experienced recrudescence of fever, chills, cough, and shortness of breath and was hospitalized at the same facility; he was treated with antibiotics for possible bacterial pneumonia and was discharged on a steroid taper. He was subsequently admitted to our facility given lack of improvement. At that time, SARS-CoV-2 NP PCR was positive (C_T 23), and extensive testing for secondary bacterial and fungal infections was negative. Given concern for persistent SARS-CoV-2 infection, he received 10 days of remdesivir and dexamethasone. His laboratory evaluation was otherwise significant for hypogammaglobulinemia, B-cell dysregulation, an abnormal CD4/CD8 ratio, and lack of lymphocyte response to tetanus and *Candida* antigens. In the context of these findings and prior thymoma, he was diagnosed with Good Syndrome and was treated with IVIG. Approximately 3 weeks later, he was again readmitted to our center with acute hypoxic respiratory failure due to COVID-19. SARS-CoV-2 NP PCR was positive (C_T 23). At that time, he was treated with 10 days of remdesivir and dexamethasone and received two doses of convalescent plasma for the management of SARS-CoV-2 infection; he also received a dose of IVIG for Good Syndrome. Convalescent plasma was found to be high titer either based on signal-to-cutoff (S/C) ratio ≥ 9.5 on the VITROS Anti-SARSCoV-2 IgG assay (Ortho Clinical Diagnostics, Raritan, NJ) or a cut off index ≥ 109 or a titer of ≥ 132 U/mL on the Elecsys Anti-SARSCoV-2 assay (Roche Diagnostics International Ltd, Rotkreuz, Switzerland). He was seen in follow up approximately 3.5 months following discharge; at that time, he was doing well and continued on monthly IVIG for his underlying immunodeficiency state.

Patient 5:

This patient was a 40-49-year-old man with marginal zone lymphoma diagnosed approximately 3 years before developing COVID-19. At the time of his lymphoma diagnosis, he was treated with bendamustine and rituximab and achieved remission; thereafter, he was continued on monthly maintenance rituximab for approximately 2 years. One month after stopping rituximab, he developed cough and shortness of breath and was diagnosed with COVID-19; the details surrounding his initial diagnosis and treatment are unknown. He continued to have dyspnea on exertion and exertional hypoxemia three months following his COVID-19 diagnosis. He underwent video-assisted thoracoscopic biopsy, and pathology showed changes compatible with organizing pneumonia secondary to COVID-19; there was no evidence of superimposed infectious or malignant process. He was treated with prednisone (40mg daily), but did not have any improvement in symptoms over the next 4 months. In this context, he was admitted to our facility for ongoing management. At that time, SARS-CoV-2 NP PCR was positive (C_T 22), and chest CT showed patchy multifocal and confluent groundglass opacities. Given concern for persistent COVID-19 infection in the setting of B-cell depleting therapy, he received a 5-day course of remdesivir and a dose of convalescent plasma. Convalescent plasma was found to be high titer either based on signal-to-cutoff (S/C) ratio ≥ 9.5 on the VITROS Anti-SARSCoV-2 IgG assay (Ortho Clinical Diagnostics, Raritan, NJ) or a cut off index ≥ 109 or a titer of ≥ 132 U/mL on the Elecsys Anti-SARSCoV-2 assay (Roche Diagnostics International Ltd, Rotkreuz, Switzerland). A subsequent SARS-CoV-2 NP PCR obtained 8 days following admission and completion of SARS-CoV-2-directed therapies was again positive (C_T 32). He improved

symptomatically and was discharged home. He was seen in outpatient follow up approximately 2.5 months later and had remained off steroids and supplemental oxygen.

Immune responses

Multiple immune measurements underscored the impact of exogenous antibody treatment and the lack of an endogenous antibody response in these patients. Both patients who received bamlanivimab within 8 days (P2 and P3) had high serum IgG titers to a pre-fusion stabilized spike trimer of reference virus Wuhan-Hu-1 and potent pseudovirus neutralizing serum titers to the reference virus at the earliest time points tested (d33 and d55, respectively) (**Figure 2**). They retained elevated, though decreasing, anti-spike IgG and neutralizing antibody titers through the last time points tested (d77 and d83, respectively). Of the two patients who received CP, P5 had low but detectable anti-spike IgG and neutralizing antibody titers at d200, four days after receiving CP. By contrast, P4, who received CP at the onset of infection, did not have detectable anti-spike IgG or detectable neutralizing antibody titers to the reference virus at d82 and d101. P1 did not receive exogenous antibody treatment, and anti-spike IgG and neutralizing antibody titers were negative at d37, indicating a lack of endogenous immune response.

We examined the peripheral cellular immune compartment for the three immunocompromised patients for whom whole blood samples were available. Immunocompromised patients P2, P4, and P5 had lower frequencies of lymphocytes within peripheral blood mononuclear cells (PBMC; 2.4% for P2; 62.3% ad 38.7% for P4 at d82 and d101; 24.0% for P5) compared to healthy controls (59.9% and 68.4%) (**Figure 3**). Age-matched patients hospitalized with COVID-19 also had low frequencies of lymphocytes within PBMC (48.3% and 31.1%) (**Figure 3**), consistent with clinical lymphopenia described with COVID-19[12,13].

The three immunocompromised patients had low to undetectable frequencies of CD19$^+$ B cells within the lymphocyte population (0.19% for P2, 0.01% for P4 at d82 and d101, and 0.01% for P5) compared to healthy controls (8.93% and 4.44%) or COVID-19 controls (21.89% and 32.91%) (**Figure 3**). We were not able to measure cellular responses for P3 due to severe anemia, however the patient received rituximab 3 months prior to infection, and at d260 still exhibited clinically low T and B cell counts. Thus, basic immune phenotyping data suggest that the antibody responses against reference SARS-CoV-2 virus observed in P2, P3, and P5 were due to exogenous treatment rather than an endogenous immune response.

Although patients P2, P4, and P5 all had CD3$^+$, CD4$^+$, and CD8$^+$ T cells, only P4 and P5 had robust SARS-CoV-2 specific T cell responses to SARS-CoV-2 peptide pools (**Figure 4**). This response was predominantly effector CD8$^+$ T cells secreting antiviral IFNg or both IFNg and TNF following *ex vivo* PBMC stimulation with pools containing spike peptides, but also included multi-functional CD4$^+$ T cell responses against pools containing spike peptides for P5. Both P4 at d82 and d101 and P5 at d200 exhibited higher magnitude SARS-CoV-2 CD8$^+$ T cells responses than either age-matched COVID-19 control at d13 or d18. In contrast, P2 at d66 and the healthy controls had only baseline levels of SARS-CoV-2 specific T cell responses (**Figure 5, Figure 6**). All subjects elicited T cell responses to a positive control antigen.

Intra-patient SARS-CoV-2 evolution

To assess within-patient SARS-CoV-2 diversity and evolution, we performed high-depth viral sequencing from residual nasopharyngeal samples collected across 1-6 time points per patient (**Figure 1**). Phylogenetic analysis of consensus SARS-CoV-2 sequences indicated that patients were infected with viral lineages circulating in the community (**Figure 7**). Sequences belonged to SARS-CoV-2 lineages B.1.2 (P1, P2, and P3), B.1.568 (P4), and B.1.493 (P5). Longitudinal samples were available from patients P2, P3, and P4, and consensus sequences from each were monophyletic, reflecting within-host evolution. Compared to the first available time point, between 4 and 26 consensus single nucleotide polymorphisms (SNPs) arose within each patient, most of which were nonsynonymous and many of which occurred in the spike protein **(Figure 8)**.

Through analysis of deep sequencing data, we identified intra-sample single nucleotide variants (iSNVs) present at >2% frequency in the patients with longitudinal samples available (P2-P4). We identified both iSNVs and fixed mutations in spike regions known to be associated with immune escape (**Figure 9**) . P2 and P3 (treated with bamlanivimab) experienced rapid evolution in the spike RBM, the target of bamlanivimab. Specifically, in P2, RBM substitution Q493R (compared to Wuhan-Hu-1) was present at d28 but reverted to the ancestral Q493 just 11 days later, at d39. At the same time, substitution S494P arose at the adjacent amino acid position. Both sites remained monomorphic until d75, when Q493R and S494 were again observed at frequencies of 20-25%. RBM substitution E484K also arose in P2 between d28 and d39 and remained detectable thereafter, but only at intermediate frequencies (29-45%), with the ancestral E484 remaining dominant. Evolution at site 484 also occurred in P3, in whom E484Q was fixed at d51, transiently became polymorphic with E484K at d56 (66% frequency E484K, 34% frequency E484Q), reverted to fixed with E484Q at d79, d91, and d101, and was fixed with E484K at d302. Thus, in both P2 and P3, substitution E484K was present either intermittently or at intermediate frequency.

We also observed changes in the spike NTD, a target of some potently neutralizing antibodies[4] but not bamlanivimab (**Figure 9**). In P2, a proline residue rapidly replaced the serine residue at site 272 between d28 and d39, with a low level of serine circulation apparent again at d75. In P3, NTD deletion V143-Y144 was present throughout infection, accompanied by adjacent substitution Y145D at all time points but the last. In addition, there were transient deletions of the upstream 5 amino acids (138-142) at d56, the upstream 1 amino acid (142) at d101, and the upstream 2 amino acids (141-142) at d302. These deletions occurred in the NTD recurrent deletion region 2 (RDR2)[4], where similar deletions have been observed in other immunocompromised patients[1,2,14–16].

In contrast to the virus evolution observed in two patients treated with bamlanivimab, we did not detect consensus-level mutations or iSNVs in the RBM or NTD for P4 at either d77, d100, or d109 (**Figure 8, Figure 9**), after CP treatments at d0 and d104. For each of the other two patients, only one sample was available. P1, who was not treated with exogenous antibodies, did not have consensus-level spike RMB or NTD mutations at d30, but did have substitution Q677P in the spike S1 subunit. P5 was infected for substantially longer and did not have consensus-level spike RBM or NTD

mutations prior to treatment with CP at d192. Only one iSNV was observed in P1, and none in P5, which may have been due to low sequencing depth (**Table 2**). Overall, we thus observed the emergence of spike mutations associated with immune evasion in only the patients undergoing bamlanivimab treatment.

Neutralization of autologous spike variants

To assess whether the variant spike proteins from P1, P2, and P3 were recognized by antibodies in autologous serum, we constructed SARS-CoV-2 pseudoviruses using replication incompetent lentiviruses expressing spike from the reference virus Wuhan-Hu-1, as well as the spike variants. All pseudoviruses infected a human cell line expressing ACE2 and could be neutralized by the human-derived anti-SARS-CoV-2 mAb CC12.1[17] (**Figure 10**).

Sera from patient P1, who did not receive exogenous antibody treatment, could not neutralize either pseudovirus containing autologous spike protein from d30, or reference virus, suggesting this patient did not elicit SARS-CoV-2 neutralizing antibodies. In contrast, sera or plasma from P2 and P3 neutralized the reference virus, but not pseudovirus containing autologous spikes (**Figure 11**). Specifically, five P2 samples from d33-d77 were unable to neutralize pseudovirus with spike from either d28 (containing P272S and Q493R) – or d39 (containing S494P, with or without E484K). Two P3 samples from d55 and d83 were unable to neutralize pseudovirus with the spike from either d51 (containing VY143del, Y145D, and E484Q) or d56 (containing DPFLGVY138del, Y145D, and E484K). These results suggest that, in P2 and P3 (treated with bamlanivimab), spike mutations conferring resistance to neutralization by serum containing active mAb had already emerged by the first sampled time point (d28 and d51, respectively). Moreover, the virus remained resistant to serum neutralization after continued spike evolution.

Discussion

Our results underscore the complex interplay between antibody-based treatment, endogenous immune responses, and within-host SARS-CoV-2 evolution in immunocompromised patients with prolonged SARS-CoV-2 infection. By examining viral evolution and both humoral and cellular immune responses from multiple patients, our study represents one of the most comprehensive investigations to date.

Overall, our results suggest that persistent infection itself may not be sufficient to promote the emergence of immunologically relevant spike mutations. Instead, opportunities for immune escape arise when persistent virus replication is combined with selective pressure such as single-agent mAb treatment and the absence of effective endogenous immune responses. We detected viruses with neutralization resistant spike mutations 1-2 months after treatment with bamlanivimab, suggesting that escape from neutralization by exogenously supplied antibody may be a key factor in allowing persistent infection, and supporting the possibility that mAbs may contribute to the emergence of resistance mutations at the population level. Due to concerns about the emergence of resistance mutations, the FDA emergency use authorization for single-agent bamlanivimab therapy was revoked, and patients have subsequently been treated with alternative single or multi-agent mAb therapies. Multi-agent mAb therapy is theoretically less likely to select for neutralization resistance[18], though it has been

reported[19,20]. Although some previous studies have indicated that convalescent plasma may also exert selective pressure during longitudinal SARS-CoV-2 infection[3,15,16], others have not[21], and we did not observe escape mutations in the two patients who were treated with CP. This is potentially due to the timing of treatment compared to sample collection, or a lower effective antibody titer of CP compared to mAb therapy.

Based on the rapid emergence of spike mutations that did not confer changes in neutralization susceptibility, we propose that selective pressures other than single-agent bamlanivimab therapy were also at play in our patients with longitudinal infection. For example, in P2, the original spike variant with RBM substitution Q493R rapidly reverted to Q493, while over the same time, replacement with S494P occurred at the adjacent site. Both variants were neutralization resistant, consistent with prior reports[22,23]. Because the Q493/S494P variant rapidly rose in frequency and persisted throughout infection, it likely had a fitness advantage compared to Q493R/S494. One plausible explanation is ACE2 affinity, since S494P has similar binding compared to wild-type virus[23,24], whereas Q493R is predicted to have weaker binding[25]. Supporting the higher fitness of S494P, it is much more common at a population level than Q493R, with 12,664 sequences[26] compared to 252 sequences[27] worldwide as of 2021-11-19. Underscoring the importance of complex fitness tradeoffs, spike RBM mutation E484K was detected at sub-consensus levels in P2 and transiently in P3. In both patients, E484K arose in the setting of existing neutralization resistance and did not alter the virus' neutralization profile. It may not have achieved fixation due to potentially weaker binding to ACE2[24], but its persistence at intermediate frequency could suggest cooperative interactions between variants[28].

Finally, we observed deletions of fluctuating length in the spike NTD RDR2[4] in one patient (P3). NTD deletions are most often reported in patients treated with CP[2,14–16], unlike our patient, but they also have been reported in immunocompromised patients without exogenous antibody treatment[29], as well as in publicly available sequences, not all of which are likely to be from immunocompromised patients[4], and in one immunocompetent patient[30]. Similar to our results, prior studies have observed NTD and RBM mutations arising as minor variants[2] and/or transiently[1]. Overall therefore, it is apparent that SARS-CoV-2 has multiple pathways available to achieve neutralization resistance, and additional selective pressures are important in determining within-host evolution in patients with longitudinal infection.

Interestingly, both patients in whom we did not observe spike RBM or NTD mutations (P4 and P5) were treated with CP and had SARS-CoV-2-specific T cell responses. P4 and P5 clinically improved soon after CP treatment, however larger studies have not demonstrated a benefit to CP, and it is no longer recommended for treatment[31]. Thus, our results raise interesting questions about the role of CD8^{+} T cells in immunocompromised patients. First, our results confirm that patients with B cell deficiencies can elicit effector T cells[32]. Other studies have observed functional SARS-CoV-2-specific CD4^{+} and CD8^{+} T cell responses in patients with B cell deficiencies, including higher magnitude CD8^{+} than CD4^{+} T cell responses[1,32,33]. However, those studies were smaller or did not also examine humoral responses. Second, our results suggest that CD8^{+} T cells may be critical to the resolution of SARS-CoV-2 infection, as suggested by other studies of immunocompromised patients[34]. Specifically, we observed clinical recovery in P4, who had no detectable neutralizing antibody response

but did have a functional SARS-CoV-2-specific CD8$^+$ T cell response, and in P5, who had functional SARS-CoV-2 specific CD4$^+$ and CD8$^+$T cell responses. By contrast, P2 succumbed to disease, after exhibiting no detectable neutralizing antibody response to autologous virus and only baseline SARS-CoV-2-specific T cell responses.

Notably, both P4 and P5 demonstrated higher magnitude CD8$^+$ T cell responses than age-matched immunocompetent patients hospitalized with COVID-19. There are a number of possible explanations for this, the most parsimonious of which is disparate timing of sampling with respect to disease onset: d82-200 for P4 and P5 versus d13-18 for the COVID-19 controls. Thus, sampling may have occurred prior to peak T cell responses in the COVID-19 controls, or there may have been a difference in quality of the T cells elicited during acute versus late infection. Indeed, despite highly variable cellular responses to SARS-CoV-2 in COVID-19 patients, studies with larger cohorts found that a hyperactivated/exhausted T cell "immunotype" was associated with acute severe disease and that the quality of T cell responses differed in acute versus convalescent phases[35,36]. Further work is needed to characterize the phenotype of responding T cells in COVID-19 patients with B cell deficiencies.

Limitations to our study include a small number of patients and the use of convenience samples. Larger clinical studies in immunocompromised populations are needed, including serial sampling to further elucidate therapies that promote immune evasion. Our work and others' emphasize the need to both protect immunocompromised patients from acquiring infection, and to prevent the forward spread of viruses with immune escape mutations. Such needs might be met with broad spectrum monoclonal antibodies and next generation SARS-CoV-2 vaccines that induce potent neutralizing antibody responses to prevent infection and memory CD8$^+$ T cell responses to control breakthrough.

Methods

This study was approved by the institutional review board at Emory University under protocols STUDY00000260, 00022371, and 00045821. Clinical data was obtained by electronic medical review. Residual nasopharyngeal (NP) swab and serum samples were obtained from the Emory Medical Labs. Whole blood samples were obtained after patient enrollment and consent.

SARS-CoV-2 molecular testing, genome sequencing, and analysis

Total nucleic acid was extracted from NP swabs and tested for SARS-CoV-2 total RNA (using an N2 target) as well as subgenomic RNA as previously described[37]. Samples underwent DNase treatment (ArcticZymes, Tromso, Norway), random hexamer cDNA synthesis (Invitrogen, New England Biolabs), Nextera XT library indexing and amplification (Illumina), and Illumina sequencing. As a negative control, water was included with each batch of samples starting from DNase. As a positive control, *in vitro* transcribed ERCC spike-ins (NIST) were added to each sample prior to cDNA synthesis. In order to analyze intra-sample single nucleotide variants (iSNVs) in patients with more than one time point available, duplicate libraries were made from extracted total nucleic acid from each sample. Reads from both libraries were merged and underwent reference-based SARS-CoV-2 genome assembly using reference NC_045512.1 (viral-ngs version 2.1.19.0-rc119). Sequences from immunocompromised

patients were aligned with 301 reference sequences collected from patients within the Emory Healthcare System between 1/1/2021 and 4/30/2021 using MAFFT as implemented in geneious (geneious.com). A maximum-likelihood tree was constructed using a general time reversible model with empirical base frequencies and a 3 rate model in IQ-TREE version 2.0 with 1,000 ultrafast boostraps[38] and visualized in FigTree (http://tree.bio.ed.ac.uk/software/figtree).

To identify iSNVs, reads were mapped to reference sequence NC_045512.1 using minimap2, variants were called using vphaser2 with maximum strand bias of 5, and variants annotated with SNPeff, all as implemented in viral-ngs version 2.1.19.0-rc119. Reads containing iSNVs were manually inspected in genious (geneious.com), and iSNVs were removed from further consideration if they were primarily found in the same position across all metagenomic sequencing reads, suggesting an artefact of Nextera library construction. To minimize false-positives from PCR or sequencing error, iSNVs are only reported if they were present in two replicate libraries from each sample and had a total frequency greater than 2%[39].

Materials

293T cells were purchased from ATCC (CRL-3216). A HeLa cell line transduced to stably express the human ACE2 receptor (ACE2-HeLa) was generously provided by David Nemazee[17]. Anti-SARS-CoV-2 neutralizing monoclonal IgG CC12.1 was generously provided by Dennis R. Burton and the International AIDS Vaccine Initiative[17]. Purified SARS-CoV-2 cross-reactive, anti-SARS monoclonal antibody CR3022[40] was generously provided by Jens Wrammert. Plasmids pCMV ΔR8.2 (replication defective HIV-1 backbone)[41] pHR' CMV-Luc (luciferase reporter plasmid)[41] VRC7480 (expresses SARS-CoV-2 Wuhan-Hu-1 full-length spike)[42] and TMPRSS2 (expresses human TMPRSS2)[42] were generously provided by the Vaccine Research Center, NIAID/NIH under a Material Transfer Agreement with Emory University. Plasmid nCoV-2P-F3CH2S[43] expressing a His-tagged, pre-fusion stabilized SARS-CoV-2 spike trimer from Wuhan-Hu-1 isolate was generously provided by Jason McLellan. Previously described peptide megapools[44] containing 15-mers overlapping by 10 residues of the SARS-CoV-2 spike ORF (CD4-S); 15-mers overlapping by 10 residues of all other non-spike SARS-CoV-2 ORFs (CD4-R); predicted HLA class I epitopes from SARS-CoV-2, including spike; and predicted HLA class I epitopes from SARS-CoV-2, not including spike, were generously provided by Alba Grifoni, Alessandro Sette, and Daniela Weiskopf.

SARS-CoV-2 Wuhan-Hu-1 spike trimer protein expression

Spike trimer plasmids were transiently transfected into Expi293 cells (ThermoFisher) with 5 mM kifunensine (Mfr), purified with His-Trap columns (Cytiva), trimers selected with a Superdex 200 gel filtration column (Mfr), and finished product dialyzed into 20 mM Tris pH 8.0, 200 mM sodium chloride, 0.02% sodium azide by the BioExpression and Fermentation Facility at the University of Georgia.

Generation of autologous SARS-CoV-2 pseudovirus constructs

Q5 Site-Directed Mutagenesis Kit (New England Biolabs) was used to introduce mutations in VRC7480 corresponding to SARS-CoV-2 variant spike proteins identified in

patients P1 (d30 psV), P2 (d28 psV, d39 psV, d39 + E484K psV), and P3 (d51 psV, d56 psV). Primers for site-directed mutagenesis were designed using the NEBaseChanger online tool (http://nebasechanger.neb.com/) and manufacturer recommended protocol and thermocycling conditions were followed. Incorporation of mutations was verified by Sanger sequencing. Variant open reading frames were excised from the plasmid by restriction digest and ligated separately into the parental VRC7480 plasmid using the Quick Ligation Kit (NEB). The entire spike protein open reading frame of each resulting variant plasmid was verified by Sanger sequencing, then used for large-scale DNA purification and pseudovirus production.

PBMC isolation and use

PBMCs were separated from whole blood using BD Vacutainer® Mononuclear CPT sodium citrate tubes and stored in a liquid nitrogen tank. Cryopreserved PBMCs were thawed in a 37 °C water bath and washed with RPMI 1640 containing 10% fetal bovine serum (FBS, Gemini), 100 units/ml of penicillin, and 100 µg/ml of streptomycin (Gibco) referred to as R10 complete medium, as well as 2 units/ml RNase-free DNase I (Sigma). Before use, cells were counted and checked for viability using a Guava cell counter (Luminex).

SARS-CoV-2 pseudovirus neutralization assay

Plasma and serum sample neutralizing activity was measured against SARS-CoV-2 pseudoviruses constructed from HIV-1 lentiviruses carrying luciferase reporter genes and pseudotyped with full-length SARS-CoV-2 spike protein. The following neutralization assay was adapted from previously published methods[42].

Pseudovirus production

Pseudoviruses were produced by seeding 16 million 293T cells (ATCC CRL-3216) into DMEM with 10% heat-inactivated FBS and 1% GlutaMAX (ThermoFisher) (DMEM-10) in a T-150 flask the night prior to transfection and incubating at 37°C in a humidified 5% CO_2 incubator. On the day of transfection, the HIV-1 lentiviral packaging plasmid, pCMV R8.2 (17.5 μg); luciferase reporter plasmid, pHR' CMV-Luc (17.5 μg); VRC7480 expressing full length SARS-CoV-2 Wuhan-Hu-1 spike or patient variant spikes (1 μg); and a plasmid expressing human TMPRSS2 (0.3 μg) were co-transfected into cells using FuGENE6 transfection reagent (Promega). Flasks were incubated under the above conditions for 48-72 hours after transfection, and cell supernatant with pseudoviruses was removed, clarified by brief centrifugation, filtered (0.45 μm), and stored in aliquots at -80°C until use.

Pseudovirus titration

ACE2-HeLa cells were seeded in Nunc Edge 2.0 plates (ThermoFisher) at 5,000 cells per well in DMEM-10 with 1% penicillin/streptomycin, and phosphate buffered saline (PBS) applied to the outer plate moats (replenished throughout the course of the experiment). Plates were stored at 37°C in a humidified 5% CO_2 incubator. Approximately 24 hours later, SARS-CoV-2 pseudoviruses were diluted in a 2-fold dilution series in MEM with 5% FBS, 1% GlutaMAX, and 1% penicillin/streptomycin (MEM-5) and pre-incubated at 37°C for 45 minutes. DMEM-10 media was then removed

from plates with cells and 50 μl pseudovirus dilutions added onto ACE2-HeLa cells and incubated for two hours at 37°C. After the incubation, 150 μl MEM-5 media was added and plates incubated an additional 72 hours at 37°C. After 72 hours, media was removed, wells washed with PBS, and 25 μl Luciferase Cell Culture Lysis Reagent (Promega) added to wells with shaking for 15 minutes at room temperature. After shaking, lysates were clarified by centrifugation and 20 μl lysate added to 96-well black and white isoplates (Perkin-Elmer). Fifty μl luciferase substrate (Luciferase Assay System, Promega) was added and luminescence quantified in a BioTek Synergy 2.0 microplate reader using a 5 second shake and a 5 second integration time with a gain of 245 (Biotek Synergy Neo2). The mean background signal (average of signal in cell only wells) was subtracted from the signal of wells with pseudoviruses prior to determining mean pseudovirus relative light units (RLUs). The final dilution of SARS-CoV-2 pseudoviruses yielding approximately 1,000,000-2,000,000 RLUs was selected for future experiments.

Neutralization assay

The same protocol was followed as for the titration above, except that pseudoviruses at 2X the final dilution were mixed with equal parts sample in a dilution series (1:15 starting dilution to achieve a final starting dilution of 1:30) in triplicate and preincubated at 37°C for 45 minutes in a humidified 5% CO_2 incubator. To compare the ability of a serum, plasma, or mAb to neutralize different psV, the same input RLUs were used for each psV (e.g., 1,000,000 RLU of P1 d30 psV and 1,000,000 RLUs of Wuhan-Hu-1 psV).The pseudovirus-sample mixture was plated onto ACE2-HeLa cells and incubated for 2 hours at 37°C. Mean background signal (cell only wells) was subtracted from signal of wells containing pseudovirus or pseudovirus plus sample. Percent neutralization was determined using the following formula:

$$\frac{(Meanbackground-subtractedpseudovirussignal)-(Meanbackground-subtractedpseudovirus+samplesignal)}{Meanbackground-subtractedpseudovirussignal}x100$$

Percent neutralization curves were fitted with a 3-parameter non-linear regression (Prism v8) to determine the half-maximal inhibitory concentration (IC50).

Samples that did not achieve 50% neutralization at 1:30 were assigned a reciprocal titer of $\leq$10 and were confirmed in triplicate at a single sample dilution of 1:30 in a separate, independent experiment (except that there was only enough P2 d55 serum to test at a single 1:60 dilution in a second experiment). Samples with >50% neutralization at 1:30 were analyzed in two or more independent experiments with full serial dilutions. The SARS-CoV-2 neutralizing monoclonal antibody CC12.1 was used as a positive control for each experiment. For the negative control, sera pooled from six healthy subjects was utilized, where the individual negative control sera were collected in Atlanta, Georgia in March to April 2020 from persons with no COVID-19 history.

SARS-CoV-2 Spike Trimer Capture ELISA

The following ELISA was adapted from previously published methods[17]: 96-well half area, high binding plates (Corning #3690) were coated with anti-6x-His-tag monoclonal antibody (#MA1-21315MG, ThermoFisher) at 2 μg /mL in PBS at 4°C

overnight. After washing three times in PBS with 0.05% Tween (wash buffer), plates were blocked with 3% BSA in PBS for 1 hour at room temperature (RT). His-tagged spike trimers at 5 μg /mL in PBS with 1% BSA and 0.05% Tween (diluent) were incubated on plates for 90 minutes at RT. Plates were washed before heat-inactivated subject serum/plasma sample dilutions were applied to the plates for 90 minutes at RT. CR3022 was applied as a positive control. Pooled control sera from the six seronegative donors described above served as the negative control. After sample incubation, plates were washed and alkaline phosphatase-conjugated goat-anti-human IgG (#109-055-008, Jackson ImmunoResearch) in diluent was applied for 1 hour at RT. After washing, plates were developed with phosphatase substrate (Sigma) in staining buffer (40 mM sodium carbonate and 10 mM magnesium chloride hexahydrate, pH 9.8). Absorbance was measured in a BioTek Synergy 2.0 microplate reader at 405 nm. Data were background-subtracted with absorbance from blank wells. Healthy control cutoffs were determined by measuring absorbances from six healthy control subject samples (described above) and applying the formula: Cutoff = mean + (standard deviation * 2.177)[45].

Mean background-subtracted absorbances were plotted relative to sample dilutions and curves fitted with a four-parameter non-linear regression (Prism v8). To ascertain a precise endpoint titer (ET), curve data (best fit values for the bottom, top, logEC50, and hill slope) were processed by a MATLAB program designed to determine the sample dilution at which each regression curve intersected the healthy control cutoff value. Samples with background-subtracted absorbances below the healthy control cutoff were assigned an ET of 10. Samples with background-subtracted absorbances slightly above the healthy control cutoff but with poor curve fitting due to low signal were assigned an ET of 30. All samples were analyzed in at least two independent experiments.

Immunophenotyping by flow cytometry

Thawed Cryopreserved PBMCs were directly used for phenotypic staining. Approximately one million viable PBMCs were stained with Zombie aqua fixable cell viability dye (BioLegend) to exclude dead cells; washed with PBS containing 2% FBS, referred to as FACS buffer; surface-stained with the following fluorescent monoclonal antibodies: CD3 (clone SK7, BioLegend), CD4 (clone SK3, BioLegend), CD8 (clone SK1, BioLegend), CD19 (clone HIB19, eBioscience), CD20 (clone 2H7, BioLegend), CD45RA (clone HI100, BD), CCR7 (clone G043H7, BioLegend), CD27 (clone M-T271, BioLegend), CD38 (clone HB7, BioLegend). Flow cytometry data were collected on an LSR Fortessa (BD Biosciences) and analyzed using FlowJo software V10 (Tree Star). Patient P2 only had 0.5 million PBMC available for staining.

Intracellular Cytokine Staining

For measuring SARS-CoV-2-specific CD4 and CD8 T cell responses, thawed cryopreserved PBMCs were rested overnight in a 5% CO_2 incubator at 37°C in R10 with DNase I. On day 2, approximately 1-2 million viable PBMCs per sample were stimulated for two hours at 37 °C in R10 with 1 μg/ml of CD4-S, CD4-R, CD8-A, or CD8-B, or negative control (R10 with equivalent peptide vehicle (DMSO)), or positive control (R10 with 1 μg/ml Staphylococcal enterotoxin B (SEB, Sigma)) in the presence of anti-CD28

and anti-CD49d (BD Biosciences). After two hours, a cocktail protein transport inhibitor (eBioscience) was added and cells were cultured for an additional 4 hours at 37°C, then stored at 4°C overnight. On day 3, samples were stained with aqua cell viability dye to exclude dead cells, surface stained with CD3 (clone SK7, BioLegend), CD4 (clone SK3, BioLegend), CD8 (clone SK1, BioLegend), CCR7 (clone G043H7, BioLegend), and CD45RA (clone HI100, BD) for 25 minutes. After washing with FACS buffer and fixing and permeabilizing cells with Cytofix/Cytoperm (BD Biosciences), the cells were stained intracellularly with the following fluorescent monoclonal antibodies: CD154 (clone CD40L 24-31, BioLegend), IL-2 (clone MQ1-17H12, BD Biosciences), IFN-γ (clone 4S.B3, eBioscience), TNF (clone Mab11, BD Biosciences). Flow cytometry data were collected on an LSR Fortessa (BD Biosciences) and analyzed using FlowJo software V10 (Tree Star).

Interferon gamma ELISPOT

Interferon gamma (IFN-γ) ELISPOT was used to enumerate the number of individual T cells secreting IFN-γ after approximately 0.2 million thawed cryopreserved PBMCs were stimulated with antigen. 96-well ELISPOT filter plates (Millipore, #MSIPS4W10) were coated with anti-human-IFN-γ (clone 1-D1K, Mabtech) overnight at 4°C. Plates were washed and blocked with R10 1-2 hours at 37°C in a 5% CO_2 incubator prior to use. Thawed and rested PBMC were resuspended in R10 at 0.2 million cells/well and mixed with 1 µg/ml each of both SARS-CoV-2 CD4-S and CD4-R peptide megapools, a negative control (R10 only), or positive control (1 µg/ml SEB) in the presence of anti-CD28 and anti-CD49d and distributed into ELISPOT plates and incubated 21-24 hours at 37 °C. IFN-γ spots were detected with biotinylated murine anti-human IFN-γ antibody (clone 7-B6-1, Mabtech), followed by incubation with streptavidin-HRP (BD) and then developed using AEC substrate (EMD Millipore). Developed and dried ELISPOT plates were scanned and counted by using an automated ELISPOT counter (Cellular Technologies Limited). Each spot forming unit (SFU) indicates an IFN-γ secreting cell and is reported as the number of SFU per million PBMC.

Data availability:

All sequence data (cleaned of human reads) are available on NCBI under BioProject PRJNA634356. SARS-CoV-2 consensus sequences are available in GISAID under accession numbers EPI_ISL_1503958 and EPI_ISL_6913932-43.

Figures

Fig. 1: Five immunocompromised patients experienced prolonged SARS-CoV-2 infection despite multiple treatments. Panels indicate the timing of hospital admissions (blue), treatments (dark pink) and SARS-CoV-2 molecular testing (medium pink) for patients P1 (A), P2 (B), P3 (C), P4 (D), and P5 (E). Timeline is not to scale. C_T values shown are from confirmatory testing in the research laboratory to ensure consistency. Boxes with dark outlines and black swabs indicate nasopharyngeal samples used for SARS-CoV-2 sequencing, and blood drops indicate samples used for humoral or cellular analysis. Abbreviations: CMV = cytomegalovirus, CP = convalescent plasma, IVIG = intravenous immunoglobulin, R-CHOP = rituximab, cyclophosphamide, hydroxydanorubicin, vincristine sulfate, prednisone, mAb = monoclonal antibody (bamlanivimab), MV= mechanical ventilation, PCP = pneumocystis carinii pneumonia.
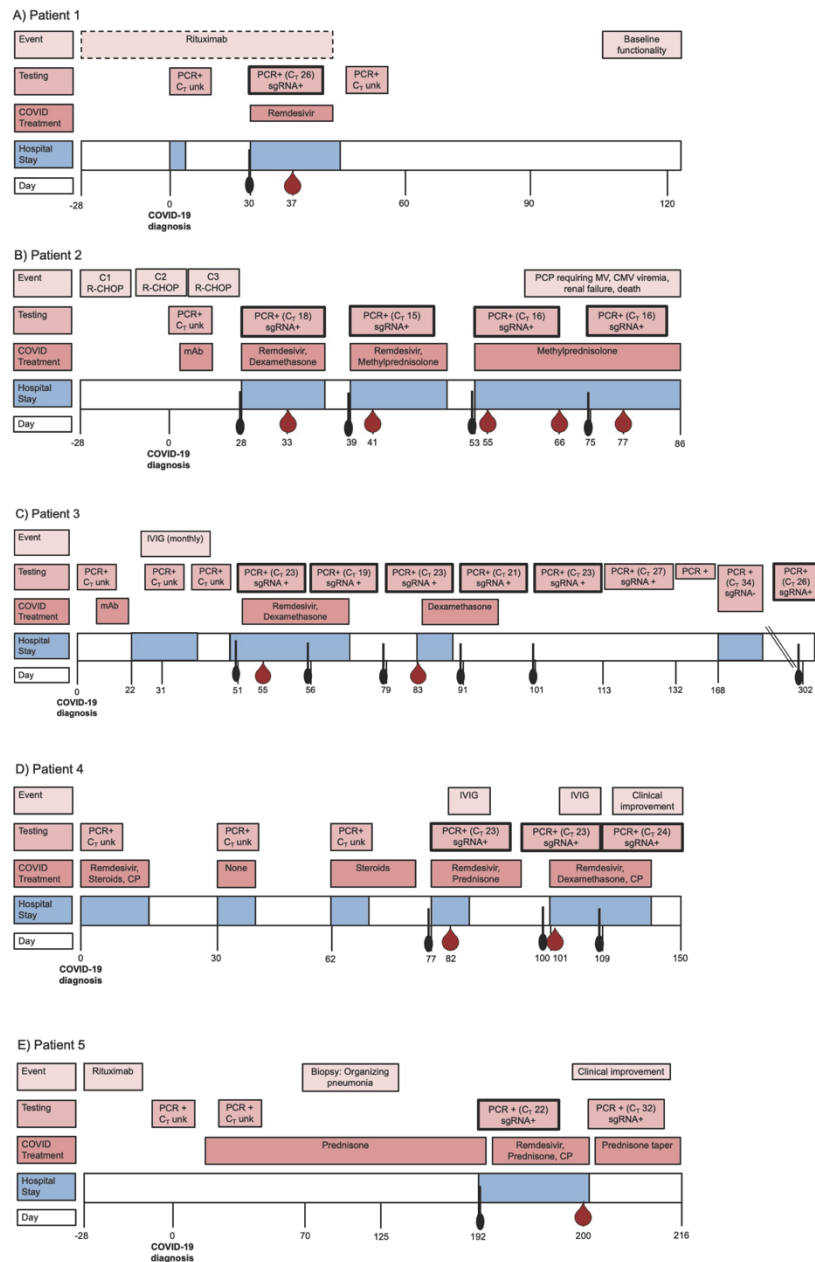
Fig. 2: Antibody responses to SARS-CoV-2 reference isolate in immunocompromised patients reflect exogenous antibody treatments. A) Endpoint IgG titers to SARS-CoV-2 Wuhan-Hu-1 spike trimer in serum samples collected from immunocompromised patients at various time points post-infection. **B)** Neutralizing titers of patient sera against a SARS-CoV-2 Wuhan-Hu-1 pseudovirus (psV) at various time points post-infection. PsV neutralizing titers represent the reciprocal serum dilution at which half-maximal psV neutralization was observed, or IC50. Data show geometric means and geometric SD from 2-5 independent experiments. The dotted line represents the limit of detection (LOD).
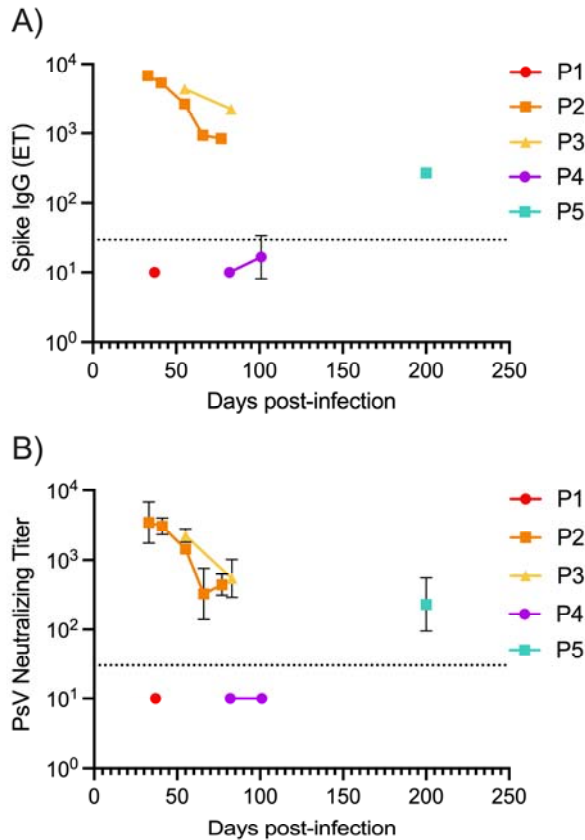
Fig.3: Gating strategy used to identify patient frequencies of lymphocytes, B cells, and T cells

PBMC from two healthy control subjects, immunocompromised patients P4 (d82 and d101) and P5 (d200), and two age-matched patients hospitalized with COVID-19 (COVID-19 controls 1 and 2) were stained with a dye that penetrates dead cells and fluorescent antibodies against surface markers and analyzed by flow cytometry. B cells and T cells are identified by the lineage specific markers CD19 or CD3, respectively.
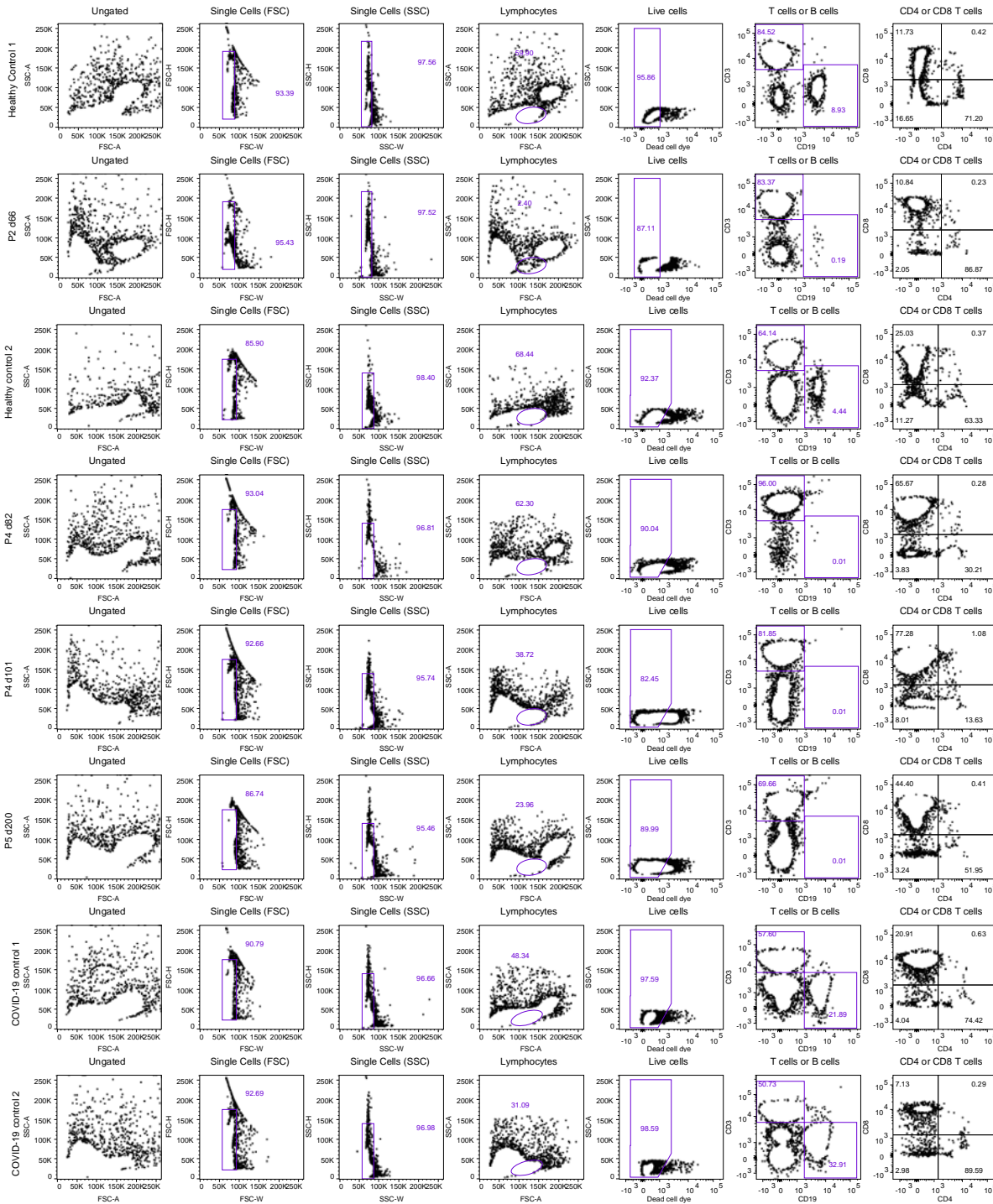
Fig. S4: Gating strategy used to identify SARS-CoV-2-specific CD4$^+$ and CD8$^+$ T cells Frequencies of non-naive CD4$^+$ or CD8$^+$ T cells responding to stimulation with a negative control (media with equivalent peptide vehicle) or peptide megapool containing predicted CD8+ T cell epitopes of SARS-CoV-2 ORFs (including spike) as an example of antigen-specific responses, were identified by intracellular cytokine staining and flow cytometry.
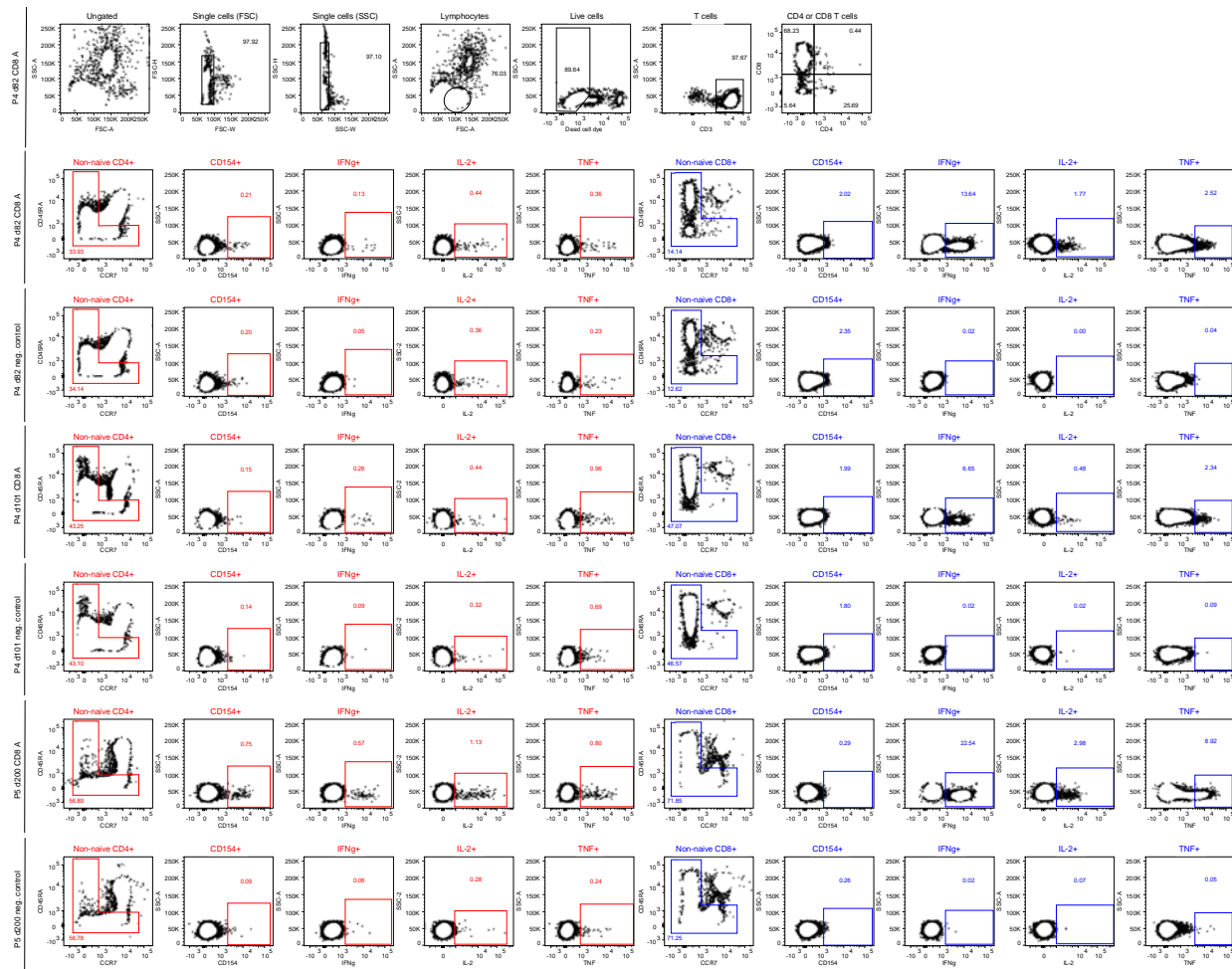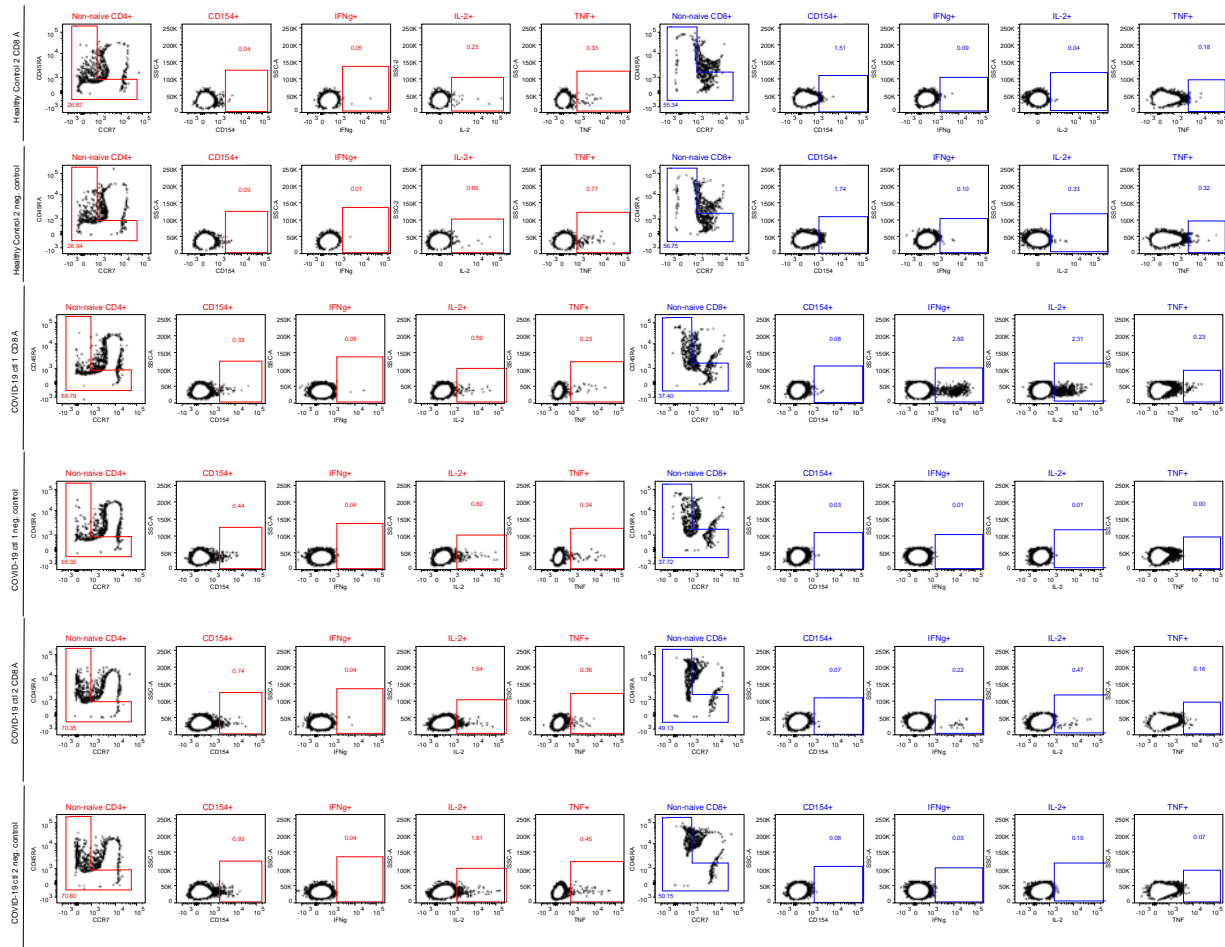
Fig. 5: Patients P4 and P5 elicit functional CD8 and CD4 T cell responses against SARS-CoV-2
PBMC isolated from patient P4 at d82 and d101 and from patient P5 at d200, as well as from a healthy control donor (HC2) and two age-matched patients hospitalized with COVID-19 (COVID 1 and 2) were stimulated with a peptide megapool containing A) 15-mers from the spike ORF, B) 15-mers from all other non-spike SARS-CoV-2 ORFs, C) predicted CD8$^+$ T cell epitopes from ORFs, including spike, or D) predicted CD8$^+$ T cell epitopes from non-spike ORFs; or E) a positive control antigen (*Staphylococcus enterotoxin* B, SEB); or a negative control (media with equivalent peptide vehicle). Frequencies of non-naive T cells out of total CD154, IFN-γ, TNF, or IL-2 expressing CD4$^+$ or CD8$^+$ T cells responding to each stimulation were measured by flow cytometry, and background responses subtracted.
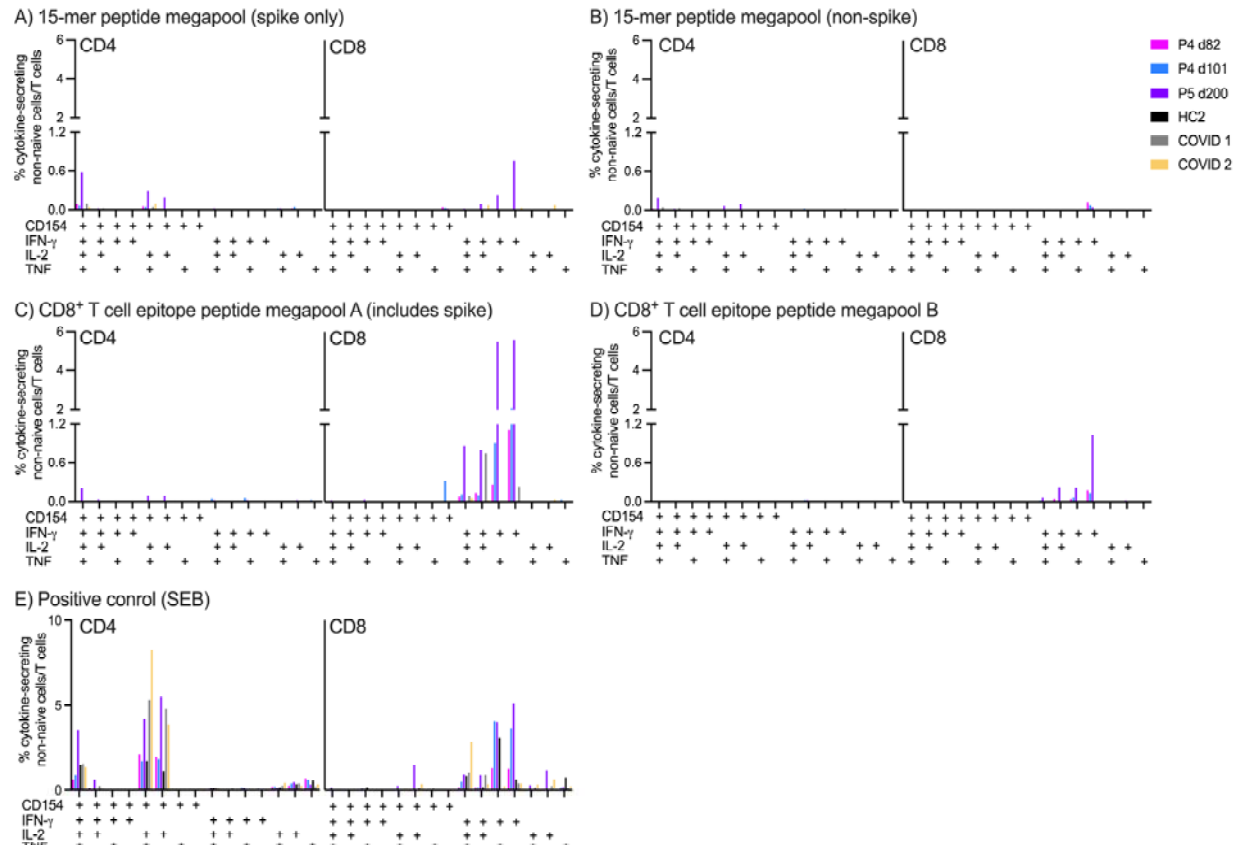
Fig. 6: Patient P2 elicits background levels of SARS-CoV-2-specific T cell responses. PBMC from patient P2 at d66 and from a healthy control (HC1) were separately stimulated with a peptide megapool containing 15-mers against all SARS-CoV-2 ORFs, a negative control (media with equivalent peptide vehicle), or a positive control (staphylococcal enterotoxin B, a superantigen). IFN-γ-secreting cells were detected by ELISPOT and quantified as spot-forming units (SFU) per well (numbers in red) and SFU per million PBMC (number in black). The assay limit of detection is $\leq$10 SFU/well.
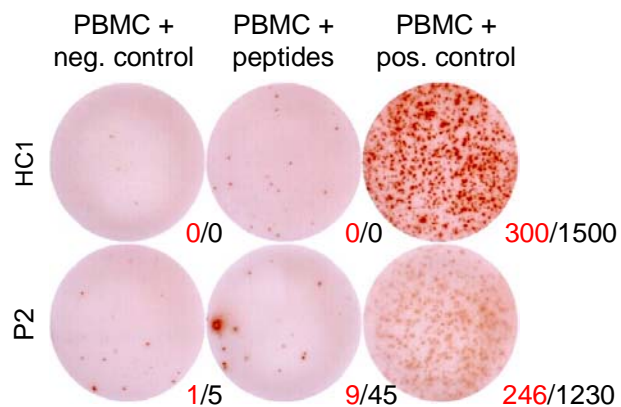
Fig. 7: SARS-CoV-2 consensus sequences from each immunocompromised patient indicate infection from the community and no evidence for reinfection in patients with longitudinal samples. Maximum-likelihood tree includes consensus SARS-CoV-2 sequences from P1 (n = 1), P2 (n = 4), P3 (n = 6), P4 (n = 3), and P5 (n = 1), as well as 301 reference sequences from patients within the Emory Healthcare system between 1/1/2021 and 4/30/2021. Sequences from each of the three patients with longitudinal samples form monophyletic clades, indicating no evidence for reinfection. 1,000 bootstrap replicates were performed, and percent bootstrap support is shown for the most recent common ancestor of each immunocompromised patient with longitudinal sampling.

Fig. 8: Consensus-level SNPs across patients. Filled green squares show SNPs that reach the consensus level relative to the Wuhan-Hu-1 reference, annotated by gene and corresponding amino acid change (if applicable). Sites where within-patient consensus-level changes occur over the course of infection are ones that transition from green to unfilled squares or from unfilled squares to green squares. Abbreviations: non-coding region (NCR); leader protein (LP); nonstructural protein (nsp); RNA-dependent RNA polymerase (RdRp); 3C-like proteinase (3C-l.p.); 3'-to-5' exonuclease (exonuclease); 2'-O-ribose methyltransferase (2'-O-r.m.); ORF3a protein (ORF3a); envelope (E); membrane glycoprotein (M); ORF7a protein (ORF7a); ORF8 protein (ORF8); nucleocapsid phosphoprotein (NcPh); deletion from A21974 to 21994 (del_1); deletion from D138-Y144 and Y145D (AA_1); deletion from T21983 to 21994 (del_2); deletion from L141 to Y144 (AA_2); deletion from T21986 to 21994 (del_3); deletion from G142-Y144 and Y145D (AA_3); deletion from T2189 to 21994 (del_4); deletion from V143-Y144 and Y145D (AA_4).

Position	Wuhan-1	SNP	Amino Acid	Gene
44	C	T	upstream	NCR
241	C	T	upstream	NCR
246	G	A	upstream	NCR
316	T	G	S17R	LP
521	G	T	V86F	LP
595	T	C	H110	LP
1042	G	T	L293F	nsp2
1059	C	T	T265I	nsp2
1347	C	T	P361L	nsp2
1630	A	G	Q455	nsp2
2113	C	T	I616	nsp2
2156	C	T	L631F	nsp2
2365	T	C	L700	nsp2
3037	C	T	F924	nsp3
3048	A	G	D928G	nsp3
3176	C	T	P971S	nsp3
4230	C	T	T1322I	nsp3
4233	A	G	D1323G	nsp3
4241	A	G	I1326V	nsp3
4250	T	C	Y1329H	nsp3
4574	A	C	T1437P	nsp3
5008	G	T	T1581	nsp3
5014	T	C	V1583	nsp3
5170	C	T	Y1635	nsp3
5175	C	T	T1637I	nsp3
5178	C	T	T1638I	nsp3
5178	C	A	T1638N	nsp4
5180	G	A	D1839N	nsp3
5629	G	T	T1788	nsp3
5654	C	T	L1797	nsp3
5830	G	A	K1855	nsp3
6001	T	A	I1912	nsp3
6025	T	C	Y1920	nsp3
6040	C	T	F1925	nsp3
6466	A	G	K2067	nsp3
6896	C	T	L2211	nsp3
7081	C	T	N2272	nsp3
8083	G	A	M2606I	nsp3
9165	C	T	T2967I	nsp4
9223	C	T	H2986	nsp4
9653	G	T	V3130F	nsp5
10279	C	T	L3338	3C-l.p.
10319	C	T	L3352F	3C-l.p.
10323	A	G	K3353R	3C-l.p.
10450	C	T	P3395	3C-l.p.
11083	G	T	L3606F	nsp6
11451	A	G	Q3729R	nsp6
11916	C	T	S3884L	nsp7
12049	C	T	N3928	nsp7
12439	C	T	P4058	nsp8
12455	C	A	L4064I	nsp8
12756	C	A	T4164N	nsp9
12775	T	C	A4170	nsp9
12806	G	A	V4181I	nsp9
12970	C	T	N4235	nsp9
13887	C	T	Y4541	RdRp
14408	C	T	P4715L	RdRp
14529	C	T	S4755	RdRp
14805	C	T	Y4847	RdRp
15276	T	A	P5004	RdRp
15591	T	C	D5109	RdRp
16428	C	T	Y5388	helicase
17285	C	T	S5674L	helicase

Position	Wuhan-1	SNP	Amino Acid	Gene
17403	C	A	A5713	helicase
17483	C	T	T5740I	helicase
17866	G	A	V5868I	helicase
18424	A	G	N6054D	exonuclease
18647	C	T	P6128L	exonuclease
19009	G	T	D6249Y	exonuclease
19402	C	T	H6380Y	exonuclease
19763	C	T	T6500I	endoRNAse
20520	T	C	D6752	endoRNAse
21304	C	T	R7014C	2'-O-r.m.
21606	G	T	C15F	spike
21614	C	T	L18F	spike
21811	C	A	V83	spike
21846	C	T	T95I	spike
21907	G	T	Q115H	spike
21952	C	T	V130	spike
21974	del_1	G	AA_1	spike
21983	del_2	-	AA_2	spike
21988	del_3	-	AA_3	spike
21989	del_4	-	AA_4	spike
22206	A	G	D215G	spike
22359	A	G	Y266C	spike
22376	C	T	P272S	spike
23012	G	A	E484K	spike
23012	G	C	E484Q	spike
23040	A	G	Q493R	spike
23042	T	C	S494P	spike
23243	C	T	P561S	spike
23284	T	C	D474	spike
22306	C	T	L582F	spike
23380	C	T	D606	spike
23403	A	G	D614G	spike
23531	A	G	N657D	spike
23592	A	C	Q677P	spike
23758	C	T	T732	spike
25563	G	T	Q57H	ORF3a
25599	G	T	W69C	ORF3a
25907	G	T	G172V	ORF3a
25913	G	A	G174D	ORF3a
26020	G	T	D210Y	ORF3a
26369	A	G	Y42C	E
26527	C	T	A2V	M
26530	A	G	D3G	M
26590	T	C	V23A	M
26957	T	C	L145	M
27074	G	T	S184	M
27712	A	G	I107V	ORF7a
27798	G	T	A15S	ORF7b
27870	G	T	E39*	ORF7b
27916	G	T	G8V	ORF8
27964	C	T	S24L	ORF9
28253	C	T	F120	ORF10
28328	G	A	G19R	N
28344	C	T	T24I	N
28472	C	T	P67S	N
28603	C	T	F110	N
28606	C	T	Y111	N
28842	G	T	S190I	N
28869	C	T	P199L	N
29194	T	C	F307	N
29370	C	T	T366I	N
29377	T	A	P368	N
29700	A	G	downstream	NCR

Fig. 9: SARS-CoV-2 spike mutations from five immunocompromised patients. Mutations in the SARS-CoV-2 spike gene for each patient and time point, compared to Wuhan-Hu-1. Shading denotes mutation frequency. For each mutation, the variant nucleotide listed in the 'Observed' row, and the amino acid mutation is listed below the plot. Gray text indicates synonymous mutations. Abbreviations: fs = frameshift, del = amino acid deletion, d1 = deletion from 21974-82; d2 = deletion from 21983-5; d3 = deletion from 21986-8; d4 = deletion from 21989-94; d5 = deletion from 21991-3. B) Mutations in the SARS-CoV-2 spike gene for all patients and time points, mapped to their locations on the genome. Abbreviations: NS = nonsynonymous, S = synonymous, Del = deletion, Ins = insertion, NTD = N terminal domain, RBD = receptor binding domain, FP = fusion peptide, HR1 = heptad repeat 1, HR2 = heptad repeat 2, TM = transmembrane, CT = C-terminal.
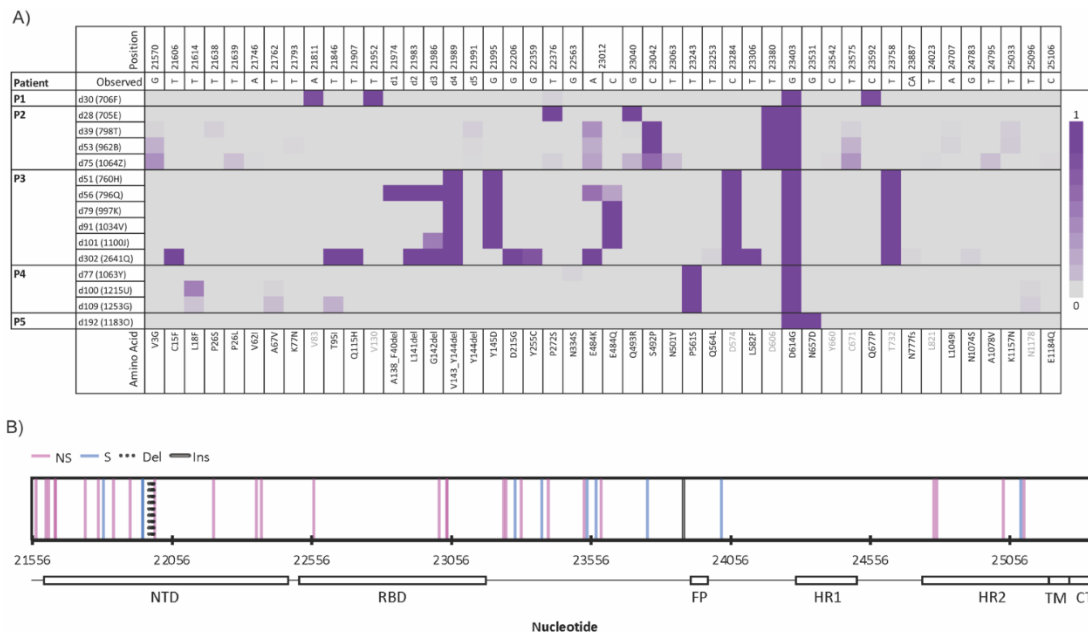
Fig. 10: Autologous variant pseudoviruses (psV) are infectious and neutralized by mAb CC12.1 A) Serial dilutions of transfection supernatants containing indicated psV were incubated with ACE2-expressing cells and assessed for expression of a luciferase reporter plasmid as a measure of productive infection. All psV were infectious, as demonstrated by high levels of background-subtracted luminescence, quantified in relative light units (RLUs), on the y-axis. Variation in RLUs obtained for different psV is not necessarily indicative of differences in psV infectivity, as it could also reflect variation in transfection efficiencies. B) Graphs show the ability of mAb CC12.1 to neutralize SARS-CoV-2 psV with Wuhan-Hu-1 spike or spikes expressing mutations corresponding to autologous viral variants P1 d30, P2 d28, P2 d39, P2 d39 + E484K (P2 minor variant), P3 d51, or P3 d56.

80
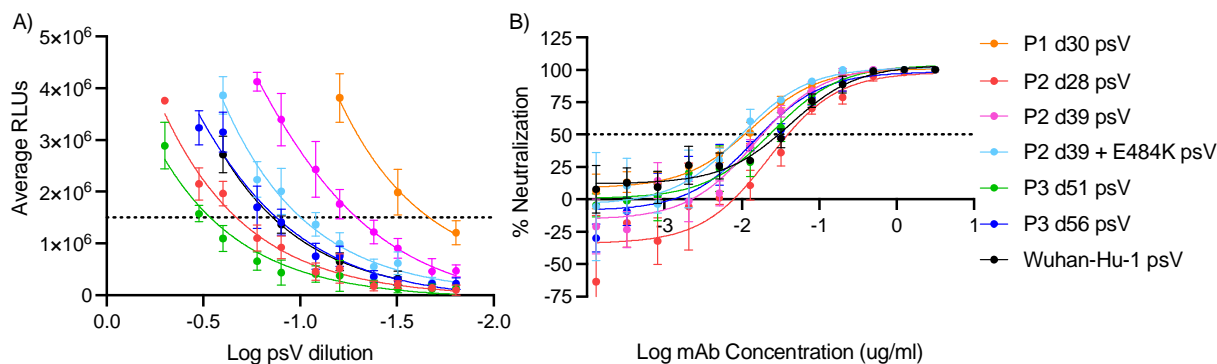
Fig. 11: Sera/plasma from patients in immunocompromised cohort cannot neutralize autologous viral variants. Graphs show the ability of sera/plasma from patients P1 (A), P2 (B), or P3 (C) at indicated time points post infection to neutralize SARS-CoV-2 pseudoviruses with Wuhan-Hu-1 spike or spikes expressing mutations corresponding to autologous viral variants P1 d30, P2 d28, P2 d39, P2 d39 + E484K (P2 minor variant), P3 d51, or P3 d56. A serum, plasma, or monoclonal antibody is designated non-neutralizing if it does not achieve 50% neutralization at the highest concentrations tested. Graphs represent the mean and SD of three replicates and are representative of at least two independent experiments.

29
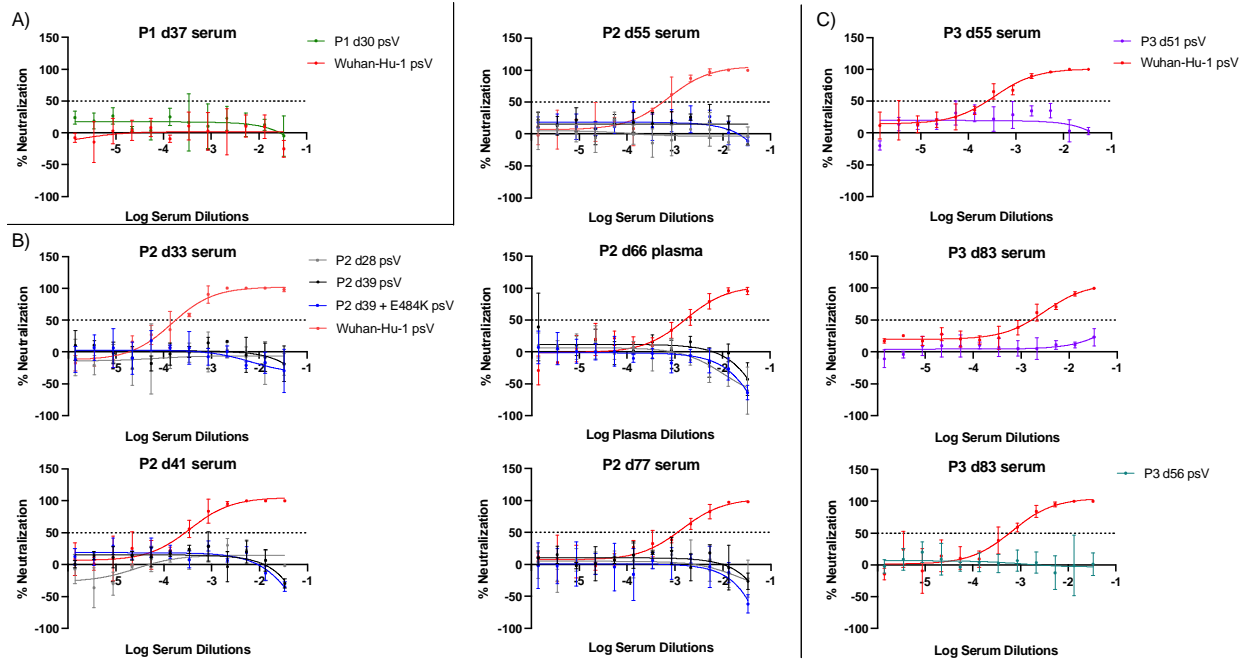
Tables

Table 1: Clinical features of five immunocompromised patients with persistent SARS-CoV-2 infection. Abbreviations: ALL= acute lymphoblastic leukemia; cGVHD = chronic graft versus host disease; DLBCL = diffuse large B cell lymphoma; MDS = myelodysplastic syndrome; PBSCT = peripheral blood stem cell transplantation; R-CHOP = rituximab, cyclophosphamide, hydroxydanorubicin, vincristine sulfate, prednisone; MMF= mycophenolate mofetil; IVIG = intravenous immunoglobulin.

	Age Range, Gender	Underlying Condition	Immuno-suppressive Treatment	Bamlanivimab	Convalescent Plasma	Latest SARS-CoV-2 PCR+	Outcome
P1	60-69, M	B-cell ALL, PBSCT, cGVHD	rituximab, tacrolimus	N	N	d42	Recovery
P2	40-49, F	DLBCL	R-CHOP	Y (d4)	N	d75	Death
P3	30-39, F	MDS, PBSCT, cGVHD	rituximab, MMF, prednisone	Y (d8)	N	d302	Recovery
P4	40-49, M	thymoma, thymectomy, Good Syndrome	N/A	N	Y (d0 and d104)	d109	Recovery
P5	40-49, M	marginal zone lymphoma	rituximab	N	Y (d196)	d201	Recovery

Table 2: Sequencing metrics. Total reads indicates total number of metagenomic sequencing reads obtained per sample, and is the sum of at least two independent sequencing libraries. Coverage indicates percent SARS-CoV-2 genome coverage based on reference-based assembly to NC_045512.1, and mean depth indicates mean depth of coverage at each SARS-CoV-2 nucleotide position.

Sample	Total Reads	Coverage	Mean depth
Patient 1			
d30: 706F	170,162,696	100%	141
Patient 2			
d28: 705E	17,361,712	100%	4,656
d39: 798T	20,598,872	100%	12,303
d53: 962B	17,485,750	100%	7,907
d75: 1064Z	15,756,412	100%	12,555
Patient 3			
d51: 760H	326,861,238	100%	427
d56: 769Q	19,928,108	100%	1,589
d79: 997K	373,163,364	100%	641
d91: 1034V	519,308,996	100%	3,031
d101: 1100J	499,743,018	100%	432
d302: 2641Q	239,745,572	100%	210
Patient 4			
d77: 1063Y	376,481,746	100%	352
d100: 1215U	353,338,568	100%	386
d109: 1253G	188,162,712	100%	358
Patient 5			
d192: 1183O	105,667,508	100%	185

References:

1. Choi B, Choudhary MC, Regan J, et al. Persistence and Evolution of SARS-CoV-2 in an Immunocompromised Host. N Engl J Med 2020;383(23):2291–3.

2. Chen L, Zody MC, Composto K, et al. Emergence of Multiple SARS-CoV-2 Antibody Escape Variants in an Immunocompromised Host Undergoing Convalescent Plasma Treatment. mSphere 2021;6(4):7.

3. Hensley MK, Bain WG, Jacobs J, et al. Intractable Coronavirus Disease 2019 (COVID-19) and Prolonged Severe Acute Respiratory Syndrome Coronavirus 2 (SARS-CoV-2) Replication in a Chimeric Antigen Receptor-Modified T-Cell Therapy Recipient: A Case Study. Clin Infect Dis 2021;73(3):e815–21.

4. McCarthy KR, Rennick LJ, Nambulli S, et al. Recurrent deletions in the SARS-CoV-2 spike glycoprotein drive antibody escape. Science 2021;371(6534):1139–42.

5. Jangra et al. SARS-CoV-2 spike E484K mutation reduces antibody neutralisation. Lancet Microbe 2021;2(7):e283-4.

6. Liu Z, VanBlargan LA, Bloyet L-M, et al. Identification of SARS-CoV-2 spike mutations that attenuate monoclonal and serum antibody neutralization. Cell Host Microbe 2021;29(3):477-488.e4.

7. Chi X, Yan R, Zhang J, et al. A neutralizing human antibody binds to the N-terminal domain of the Spike protein of SARS-CoV-2. Science 2020;369(6504):650–5.

8. Starr TN, Greaney AJ, Addetia A, et al. Prospective mapping of viral mutations that escape antibodies used to treat COVID-19. Science 2021;371(6531):850-4:5.

9. Greaney AJ, Loes AN, Crawford KHD, et al. Comprehensive mapping of mutations in the SARS-CoV-2 receptor-binding domain that affect recognition by polyclonal human plasma antibodies. Cell Host Microbe 2021;29(3):463-476.e6.

10. Corey L, Beyrer C, Cohen MS, Michael NL, Bedford T, Rolland M. SARS-CoV-2 Variants in Patients with Immunosuppression. N Engl J Med 2021;5.

11. Cele S, Karim F, Lustig G, et al. SARS-CoV-2 prolonged infection during advanced HIV disease evolves extensive immune escape. Cell Host Microbe 2022;30(2):154-162.e5.

12. Chen G, Wu D, Guo W, et al. Clinical and immunological features of severe and moderate coronavirus disease 2019. J Clin Invest 2020;130(5):2620–9.

13. Tan L, Wang Q, Zhang D, et al. Lymphopenia predicts disease severity of COVID-19: a descriptive and predictive study. Signal Transduct Target Ther 2020;5(1):33.

14. Avanzato VA, Matson MJ, Seifert SN, et al. Case Study: Prolonged Infectious SARS-CoV-2 Shedding from an Asymptomatic Immunocompromised Individual with Cancer. Cell 2020;183(7):1901-1912.e9.

15. The CITIID-NIHR BioResource COVID-19 Collaboration, The COVID-19 Genomics UK (COG-UK) Consortium, Kemp SA, et al. SARS-CoV-2 evolution during treatment of chronic infection. Nature 2021;592(7853):277–82.

16. Truong TT, Ryutov A, Pandey U, et al. Increased viral variants in children and young adults with impaired humoral immunity and persistent SARS-CoV-2 infection: A consecutive case series. EBioMedicine 2021;67:103355.

17. Rogers TF, Zhao F, Huang D, et al. Isolation of potent SARS-CoV-2 neutralizing antibodies and protection from disease in a small animal model. Science 2020;369(6506):956–63.

18. Baum A, Fulton BO, Wloga E, et al. Antibody cocktail to SARS-CoV-2 spike protein prevents rapid mutational escape seen with individual antibodies. Science 2020;369(6506):1014–8.

19. Daniele Focosi, Federica Novazzi, Angelo Genoni, Francesco Dentali, Daniela Dalla Gasperina, Andreina Baj, and Fabrizio Maggi. Emergence of SARS-COV-2 Spike Protein Escape Mutation Q493R after Treatment for COVID-19. Emerg Infect Dis 2021;

20. Guigon A, Faure E, Lemaire C, et al. Emergence of Q493R mutation in SARS-CoV-2 spike protein during bamlanivimab/etesevimab treatment and resistance to viral clearance. J Infect 2021;S0163445321004357.

21. Baang JH, Smith C, Mirabelli C, et al. Prolonged Severe Acute Respiratory Syndrome Coronavirus 2 Replication in an Immunocompromised Patient. J Infect Dis 2021;223(1):23–7.

22. Alenquer M, Ferreira F, Lousa D, et al. Signatures in SARS-CoV-2 spike protein conferring escape to neutralizing antibodies. PLOS Pathog 2021;17(8):e1009772.

23. Starr TN, Greaney AJ, Dingens AS, Bloom JD. Complete map of SARS-CoV-2 RBD mutations that escape the monoclonal antibody LY-CoV555 and its cocktail with LY-CoV016. Cell Rep Med 2021;2(4):100255.

24. Upadhyay V, Lucas A, Panja S, Miyauchi R, Mallela KMG. Receptor binding, immune escape, and protein stability direct the natural selection of SARS-CoV-2 variants. J Biol Chem 2021;297(4):101208.

25. Ortega JT, Pujol FH, Jastrzebska B, Rangel HR. Mutations in the SARS-CoV-2 spike protein modulate the virus affinity to the human ACE2 receptor, an in silico analysis. EXCLI 2021;

26. Alaa Abdel Latif, Julia L. Mullen, Manar Alkuzweny, Ginger Tsueng, Marco Cano, Emily Haag, Jerry Zhou, Mark Zeller, Emory Hufbauer, Nate Matteson, Chunlei Wu, Kristian G. Andersen, Andrew I. Su, Karthik Gangavarapu, Laura D. Hughes, and the Center for Viral Systems Biology. outbreak.info. S:S494P Mutation Report.

27. Alaa Abdel Latif, Julia L. Mullen, Manar Alkuzweny, Ginger Tsueng, Marco Cano, Emily Haag, Jerry Zhou, Mark Zeller, Emory Hufbauer, Nate Matteson, Chunlei Wu, Kristian G. Andersen, Andrew I. Su, Karthik Gangavarapu, Laura D. Hughes, and the Center for Viral Systems Biology. outbreak.info. S:Q493R Mutation Report.

28. Xue KS, Hooper KA, Ollodart AR, Dingens AS, Bloom JD. Cooperation between distinct viral variants promotes growth of H3N2 influenza in cell culture. eLife 2016;5:e13974.

29. Weigang S, Fuchs J, Zimmer G, et al. Within-host evolution of SARS-CoV-2 in an immunosuppressed COVID-19 patient as a source of immune escape variants. Nat Commun 2021;12(1):6405.

30. Ko SH, Bayat Mokhtari E, Mudvari P, et al. High-throughput, single-copy sequencing reveals SARS-CoV-2 spike variants coincident with mounting humoral immunity during acute COVID-19. PLOS Pathog 2021;17(4):e1009431.

31. Lynch JB, Davitkov P, Anderson DJ, Bhimraj A, Cheng VC, Guzman-Cottrill J, Dhindsa J, Duggal A, Jain MK, Lee GM, Liang SY, McGeer A, Lavergne V, Murad MH, Mustafa RA, Morgan RL, Falck-Ytter Y, Sultan S. Infectious Diseases Society of America Guidelines on Infection Prevention in Patients with Suspected or Known COVID-19. Infect Dis Soc Am 2020;1.0.1.

32. Gaitzsch E, Passerini V, Khatamzas E, et al. COVID-19 in Patients Receiving CD20-depleting Immunochemotherapy for B-cell Lymphoma. HemaSphere 2021;5(7):e603.

33. Sepulcri C, Dentone C, Mikulska M, et al. The Longest Persistence of Viable SARS-CoV-2 With Recurrence of Viremia and Relapsing Symptomatic COVID-19 in an Immunocompromised Patient—A Case Study. Open Forum Infect Dis 2021;8(11):ofab217.

34. Turner JS, Day A, Alsoussi WB, et al. SARS-CoV-2 Viral RNA Shedding for More Than 87 Days in an Individual With an Impaired CD8+ T Cell Response. Front Immunol 2021;11:618402.

35. Sekine T, Perez-Potti A, Rivera-Ballesteros O, et al. Robust T Cell Immunity in Convalescent Individuals with Asymptomatic or Mild COVID-19. Cell 2020;183(1):158-168.e14.

36. Mathew D, Giles JR, Baxter AE, et al. Deep immune profiling of COVID-19 patients reveals distinct immunotypes with therapeutic implications. Science 2020;369(6508):eabc8511:18.

37. Immergluck K, Gonzalez MD, Frediani JK, et al. Correlation of SARS-CoV-2 Subgenomic RNA with Antigen Detection in Nasal Midturbinate Swab Specimens. Emerg Infect Dis 2021;27(11):2887–91.

38. Nguyen L-T, Schmidt HA, von Haeseler A, Minh BQ. IQ-TREE: A Fast and Effective Stochastic Algorithm for Estimating Maximum-Likelihood Phylogenies. Mol Biol Evol 2015;32(1):268–74.

39. Cingolani P, Platts A, Wang LL, et al. A program for annotating and predicting the effects of single nucleotide polymorphisms, SnpEff: SNPs in the genome of Drosophila melanogaster strain w [1118]□; iso-2; iso-3. Fly (Austin) 2012;6(2):80–92.

40. ter Meulen J, van den Brink EN, Poon LLM, et al. Human Monoclonal Antibody Combination against SARS Coronavirus: Synergy and Coverage of Escape Mutants. PLoS Med 2006;3(7):e237.

41. Naldini L, Blömer U, Gage FH, Trono D, Verma IM. Efficient transfer, integration, and sustained long-term expression of the transgene in adult rat brains injected with a lentiviral vector. Proc Natl Acad Sci 1996;93(21):11382–8.

42. Corbett KS, Edwards DK, Leist SR, et al. SARS-CoV-2 mRNA vaccine design enabled by prototype pathogen preparedness. Nature 2020;586(7830):567–71.

43. Wrapp D, Wang N, Corbett KS, et al. Cryo-EM structure of the 2019-nCoV spike in the prefusion conformation. Science 2020;367(6483):1260–3.

44. Grifoni A, Weiskopf D, Ramirez SI, et al. Targets of T Cell Responses to SARS-CoV-2 Coronavirus in Humans with COVID-19 Disease and Unexposed Individuals. Cell 2020;181(7):1489-1501.e15.

45. Frey A, Di Canzio J, Zurakowski D. A statistically defined endpoint titer determination method for immunoassays. J Immunol Methods 1998;221(1–2):35–41.

Chapter 5

Haplotypes are more informative than iSNVs when interpreting the evolutionary dynamics of SARS-CoV-2 within an immunocompromised host

Brent Allman[1,*], Rose Langsjeon[2], Anne Piantadosi[2,3], Katia Koelle[4,†], Daniel Weissman[4,5,†]

[1]Graduate Program in Population Biology, Ecology, and Evolution, Emory University, Atlanta, Georgia 30322

[2]Department of Pathology and Laboratory Medicine, Emory University School of Medicine, Atlanta, Georgia 30322

[3]Division of Infectious Diseases, Department of Medicine, Emory University School of Medicine, Atlanta, Georgia 30322

[4]Department of Biology, Emory University, Atlanta, Georgia 30322

[5]Department of Physics, Emory University, Atlanta, Georgia 30322

†Authors contributed equally

*Corresponding author: Brent Allman. Emory University, Department of Biology, O. Wayne Rollins Research Center, 1510 Clifton Road NE, Atlanta, GA 30322. Email: allmanbrent@gmail.com

5.1 Abstract

The within host evolution of SARS-CoV-2 is the primary setting where selection acts on the virus, and is ultimately the source of viral variants that are more transmissible, prone to immune escape, or altered COVID-19 pathology. In particular, immunocompromised hosts and hosts with chronic infections have been implicated as a source for the emergence of variants of concern because selection has more time to act on within host viral populations than in acute infections. Analyses of the diversity that is generated in these hosts have revealed large amounts of viral diversity, indeed, some of which confer immunologically relevant phenotypes. However, here we underscore the importance of considering genetic linkage when interpreting the dynamics of these intra-host single nucleotide variants (iSNVs). Using samples from an immunocompromised host, we present the conclusions that one might draw about the evolutionary dynamics within the host when assuming iSNVs are independent, in contrast to narratives that include observed and inferred genetic linkage.

5.2 Introduction

The evolution of viruses within their individual hosts is what gives rise to adaptations that can impact entire host populations. For emerging pathogens like SARS-CoV-2, the community is still working to understand how evolutionary forces within host affect the adaptation of the virus. Experimental work on SARS-CoV-2 has found that that mutations occur at a rate of 10^{-6} mutations/site/replication cycle, corresponding to 0.03 mutations per replication across the roughly 30 kb viral genome (Amicone et al., 2022). Inferred transmission bottlenecks between hosts of under 10 virions (Lythgoe et al., 2021, Martin and Koelle, 2021, Braun et al., 2021, San et al., 2021) and narrow bottlenecks between tissues at the within host level (Wang et al., 2021) impose strong genetic drift on the viral population. While selection pressure from the human immune system is generally weak over the course of an acute infection (Lythgoe et al., 2021, Braun et al., 2021), chronic infections in immunocompromised or immunosuppressed individuals are thought to allow more opportunity for mutations to arise and selection to act on them (Siqueira et al., 2021). Indeed, one prominent hypothesis for the emergence of variants of concern (VOCs) such as Alpha and Omicron is that they evolved in chronically infected individuals, where selection imposed by the immune system or drug treatments had more time to act (Ghafari et al., 2022). In these individuals, as well as in acute infections, multiple host tissues can be infected and the diversity of viral subpopulations can vary across tissues (Wang et al., 2021). This points towards the potential for compartmentalization that may occur within hosts as a source of genetic diversity in a sampled tissue. Finally, re-infection can be a potential source of additional genetic diversity and this phenomenon is more likely to occur for hosts experiencing a long-term infection.

To characterize patterns of within-host SARS-CoV-2 evolution, many studies have made use of repeated sampling of individuals over the course of their infection (Scherer et al., 2022, Tonkin-Hill et al., 2021, Valesano et al., 2021, Wu et al., 2021). The ma-

jority of these studies describe the dynamics of viral diversity by identifying intrahost single nucleotide variant (iSNVs) from these samples and examining their frequency dynamics over time. The within-host dynamics of iSNVs have been used to determine whether particular iSNVs evolve in parallel across epidemiologically unlinked hosts (Valesano et al., 2021) and to infer transmission clusters (Popa et al., 2020, San et al., 2021). These iSNV data have also been used to infer transmission bottleneck sizes (Popa et al., 2020, Martin and Koelle, 2021).

While identifying iSNVs and tracking their dynamics has greatly contributed to our understanding of SARS-CoV-2 evolution over the last two years, assuming that iSNVs evolve independently from one another can lead to erroneous inferences about the fitness effects of single point mutations. This is because genetic linkage can be present between loci, and selection acting on one locus can therefore impact iSNV frequency dynamics at another locus. This process of genetic hitchhiking occurs most commonly when iSNVs lie in close proximity to one another on the viral genome, such that recombination between iSNV loci is rare and linkage disequilibrium can thus persist over longer periods of time. Genetic linkage and the potential for hitchhiking underscores the importance of not relying solely on a panel of iSNV frequencies for evolutionary inference.

Some SARS-CoV-2 studies have gone further to look at genetic linkage. Most of these studies that utilize haplotypes have focused on quantifying transmission bottleneck sizes between hosts (Sekizuka et al., 2020, San et al., 2021), rather than using them to dissect the evolutionary dynamics of SARS-CoV-2 within individual hosts. Genetic linkage is also used for statistical inference of co-infection. Single nucleotide polymorphisms (SNPs) that are clade-defining at the epidemiological level (Manuto et al., 2022, Zhou et al., 2021) are utilized for constructing narratives around intra-host evolution since clade-defining SNPs (cdSNPs) often occur together. The assumption of cdSNPs being linked has also been used for detecting recombinant

SARS-CoV-2 genomes (VanInsberghe et al., 2021). Additional methods for detecting co-infection using genetic linkage use physical read data to identify co-occurring iSNVs (Francisco Junior et al., 2022), thus reconstructing haplotypes. Others have used haplotype analysis to refine analyses of within-host SARS-CoV-2 evolution, but even these can be imperfect. To determine haplotypes across the entire genome, statistical inference is used on iSNV frequencies. For example, Wu et al. (2021) assert that two of their patients were re-infected because the dominant haplotype in their first samples were replaced in their second samples. This was then confirmed with phylogenetic analysis. Had they only relied on iSNV frequencies, they could have attributed the presence of new haplotypes to *de novo* mutations on the original background sequences.

Here, we provide an example of how incorporating a haplotype perspective can fundamentally alter the interpretation of within-host viral evolutionary dynamics. From a study of immunocompromised patients with chronic SARS-CoV-2 infections (Scherer et al., 2022), we use short-read sequences from longitudinal samples to call iSNVs and to both identify and infer haplotypes, and offer interpretations of their frequency dynamics.

5.3 Methods

5.3.1 Data

We use nasopharyngeal swab samples from a single patient that were collected at Emory University Hospital in Atlanta, Georgia as part of a larger study of five immunocompromised individuals experiencing chronic SARS-CoV-2 infection and presenting with COVID-19 symptoms (Scherer et al., 2022). We chose Patient 2 as our focal patient because high frequency intrahost single nucleotide variants (iSNVs) called from this patient were close enough on the genome to observe physical haplo-

types, rather than relying solely on statistically inferred haplotypes.

The patient was a 46-year old woman who first tested positive for SARS-CoV-2 on January 4, 2021. We label this date as day 0 (d0) of their documented infection. The patient's course of treatment included monoclonal antibodies (bamlanivimab) on d4 of infection and two courses of antiviral medication (remdesivir), administered between d28 to d32 and again between d40 to d45 (Fig. 5.1A). The patient ultimately passed away on d86 from disease-related complications. A more detailed clinical course for this patient is available in the supplementary materials of (Scherer et al., 2022).

Samples for viral sequencing were collected on d28, d39, d53, and d75 of infection. Each of these samples had low SARS-CoV-2 PCR cycle threshold (Ct) values, indicative of high viral loads (Fig. 5.1A). Two technical replicates of each sample allowed for the creation of two duplicate libraries sequenced at high coverage using Illumina technology. Additional details on the sequencing methodology and summary statistics can be found in the supplementary materials of (Scherer et al., 2022).

Sequencing reads were then used to create consensus sequences using viral-ngs (version 2.1.19.0-rc119) for reference-based assembly against the Wuhan reference strain, NC_045512.1. Alignment of reads from each library against the consensus sequence from d28 was done using bbmap (`https://sourceforge.net/projects/bbmap/`). We used the d28 consensus sequence rather than the canonical Wuhan reference strain to detect evolutionary changes from the sequence presumed to be most closely related to the strain that initially infected the patient. We used the following parameters when implementing bbmap: minratio=0.8, maxindel=100, ambig=toss, minaveragequality=15, qin=33, maxlen=150.

5.3.2 Calling of intrahost single nucleotide variants

After aligning each library to the d28 consensus genome, the reads were then analyzed using LoFreq (Wilm et al., 2012) to detect iSNVs relative to the d28 consensus. We
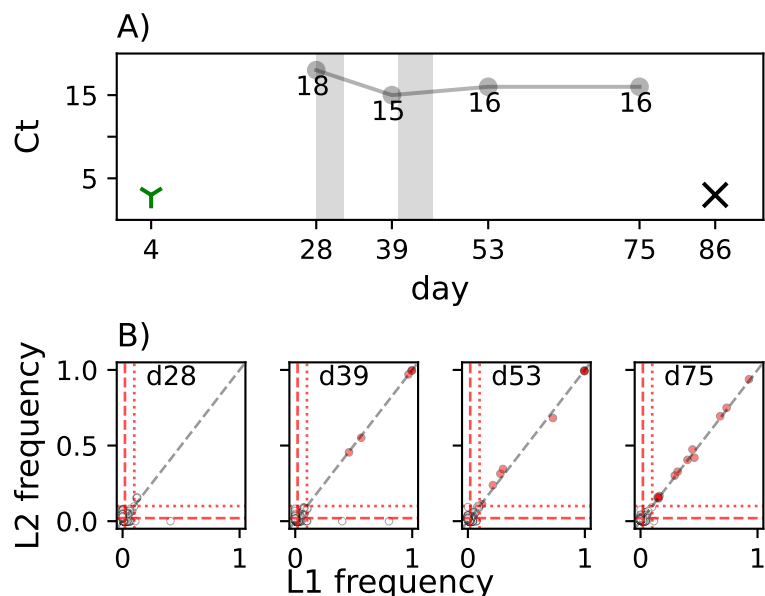
Figure 5.1: Throughout the duration of the patient's clinical course, four nasopharyngeal swabs were used to collect samples for next-generation sequencing. **(A)** The four samples collected from the patient that were sent for sequencing were collected on d28, d39, and d53, and had low Ct values, shown next to their respective points. The patient received two forms of treatment for their SARS-CoV-2 infection: monocolonal antibody treatment (bamlanivimab; mAb), and antiviral medication (remdesivir). mAb administered on d4 is denoted by the green Y-shaped icon. Remdesivir treatment from d28 to d32 and again from d40 to d45 is indicated by the gray shaded regions. The patient succumbed to the infection on d86, shown by the black X-shaped icon. **(B)** iSNV frequencies from the same sample are plotted by library. Red dashed lines show the 2% frequency cutoff for calling an iSNV. Red dotted lines show the 10% frequency cutoff for being considered high-frequency iSNVs. iSNVs close to the black dashed one-to-one line indicate frequencies called from each library are nearly equal. Red points are those that are included in the analysis within this manuscript. The white points are excluded for being below the described frequency thresholds or being designated as spurious.

compare the iSNVs called by LoFreq in each individual library and we consider iSNVs that are called in each library above a 2% threshold as validated iSNVs (Fig. 5.1B). The source of the discrepancies between libraries could be mismapped reads, stochasticity of the sequencing platform, or uneven coverage between libraries.

We also merged the two libraries for each respective sample, and called iSNVs from the merged set of reads using LoFreq. We further cleaned the data manually by looking at the loci detected above 10% in the merged library, visualized using Geneious Prime 2022.0.2. By library, we disposed of reads that were clearly mismapped, as

indicated by roughly 10 or more variant nucleotides in a row. Reads with this characteristic often had high homology elsewhere in the SARS-CoV-2 genome. Once these reads were preened from the respective libraries, we ran LoFreq on each individual library, and the merged libraries. Once again, iSNVs were validated only if detected above 2% in both libraries individually (Fig. 5.1B). The frequencies reported here are those from the merged lofreq calls. For this study, we further narrow the panel of iSNVs by only considering those that have a frequency > 10% in one or more samples. Amino acid changes were annotated using the software Nextclade (Aksamentov et al., 2021).

5.3.3   Reconstruction of haplotypes

We used the aligned reads from the merged libraries to detect haplotypes. Using bespoke scripts, we identify reads with more than one validated iSNV present. Among the reads that span these sites, we determine the number of reads that have each combination of variant and reference nucleotides. We only identified haplotypes among four sites (22999, 23027, 23029, 23050) because those were the only high frequency iSNVs close enough to be located on the same reads. We then use these physically observed haplotypes as the basis for evolutionary explanations of iSNV dynamics.

5.4   Results

Figure 5.1B shows the frequencies of called iSNVs by replicate library. While there is generally high congruence between iSNV frequencies, some iSNVs are called in one of the two libraries for a given sample. Most of the iSNVs called in only a single library are present in that library at very low frequencies. Exceptions to this are evident on d28 and d39, where iSNVs having frequencies of 40% (d28), 40% (d39) and 80% (d39) in the first library are not called in the second library. Two of these iSNVs occur in

the first 15 nucleotides of the alignment, which is prone to sequencing error. In the other, there is no read support in the second library. Therefore, despite being called at high frequency in one library, they did not meet our criteria for high quality iSNV calls and we do not consider them further in the analysis.

At the first time of sampling, there are very few iSNVs present (Fig. 5.1B), so we first compare the d28 consensus sequence to what is circulating in the population to determine how much genetic change may have occurred since d0. Because these sites become important later, we focus on the sites that we can observe physical linkage, 22999, 23027, 23029, 23050. The respective nucleotide identities from the consensus genome on d28 are GGTA. Using the consensus sequences collected in Georgia during the patient's infection period, we can see that there are two dominant haplotypes at our physically linked sites circulating at this time, GATA and GATT, with several others circulating at low frequency (Fig. 5.2). At the beginning of the infection, GATA is at high frequency, so it is feasible that a virus with these mutations initially infected the patient. Under this assumption, the viral population within the patient had at least one mutation sweep the population, since by d28, 23027G has fixed in the host (Fig. 5.3B). This site is implicated in an amino acid change within spike at site 493, which is a known target of bamlanivimab therapy (Guigon et al., 2022, Focosi et al., 2021), which this patient received on d4 of their infection.

5.4.1 iSNV dynamics appear to indicate multiple targets of selection

High-frequency iSNVs were identified across the SARS-CoV-2 genome, concentrated in the spike gene (Fig. 5.3A, sites 21557 and above). While the majority of these iSNVs were nonsynonymous, several were synonymous. Several iSNVs appear to reach fixation between d28 and d39: T22363C, G23027A, and T23029C (Fig. 5.3B). These three sites are all nonsynonymous, and so are likely to have phenotypic effects.

Figure 5.2: Observed consensus-level combinations of mutations at a subset of sites circulating in Georgia during the duration of the patient's infection. **(A)** Sequences here are taken from one week prior to symptom onset and first positive PCR test, to the final sampled time point of the infection. Alignments to the d28 consensus were done using Geneious. Complete Georgia consensus genomes were obtained from GISAID. Sites and nucleotide identities presented here the same as Fig. 5.4A, 22999, 23027, 23029, and 23050. The red dotted line indicates the first positive PCR test from the patient and each dashed gray line shows the dates for sequenced patient samples.

Their rapid rise between d28 and d39 indicates that these iSNVs may be beneficial, confer some fitness advantage within this immunocompromised host environment. Two additional iSNVs emerge and rise to high frequencies ($\sim$ 50%) between d28 and d39 (C7068T and G22999A). The fixation of these three iSNVs and the increase in frequency of the latter two iSNVs occurred in concert with remdesivir treatment administered from d28 to d32 of the infection period (Fig. 5.1A). With all of these iSNVs being nonsynonymous, with the exception of 7068T, and their presence in the spike region, it is likely that selection was imposed at these sites as a result of treatment. Additional high-frequency iSNVs appear by d53 and d75. The frequencies

of the iSNVs that are first detected on d58 rise by d75 (Fig. 5.3B). Together, the rapid frequency increases of the 12 iSNVs shown in Fig. 5.3 indicates that positive selection is likely acting on at least a subset of these iSNVs.

Between d53 and d75, the three iSNVs that previously appeared fixed each decreased in frequency. These frequency decreases were each accompanied by the reappearance of the reference nucleotides at these sites (rather than the emergence of a third nucleotide). Under the assumption of iSNV independence, their decline may reflect changes in the within-host environment that would now favor the reference nucleotides. Together, the detection and analysis of individual iSNVs in patient 2 indicates that at least 12 iSNVs are likely to confer a fitness advantage within the context of this individual. Additionally, one could surmise that the patient may have become reinfected with circulating SARS-CoV-2 virus, and that the drop in iSNV frequencies at sites 22363, 23027, and 23029 resulted from a coinfection on d75.

5.4.2 Haplotype reconstruction casts doubts on independent selection on individual iSNVs and points towards the role of within-host reservoirs

Four of the high-frequency iSNVs shown in Fig. 5.3 (G22999A, G23027A, T23029C, A23050T) lie within 51 nucleotides of one another. As such, reads spanning these four sites could be used to determine haplotype frequencies across this region of the genome. Based on these reads, we found that five distinct haplotypes were circulating at appreciable levels within the patient (Table 5.1). Longitudinal dynamics of these haplotype frequencies are visualized in Fig. 5.4A. Haplotype GGTA (present in the consensus sequence of d28) is fixed on d28 but does not appear present 11 days later, on d39 (Fig. 5.4A). On d39, there are instead two unique haplotypes detected (GACA and AACA), which differ from one another by a single nucleotide (at site 22999), but
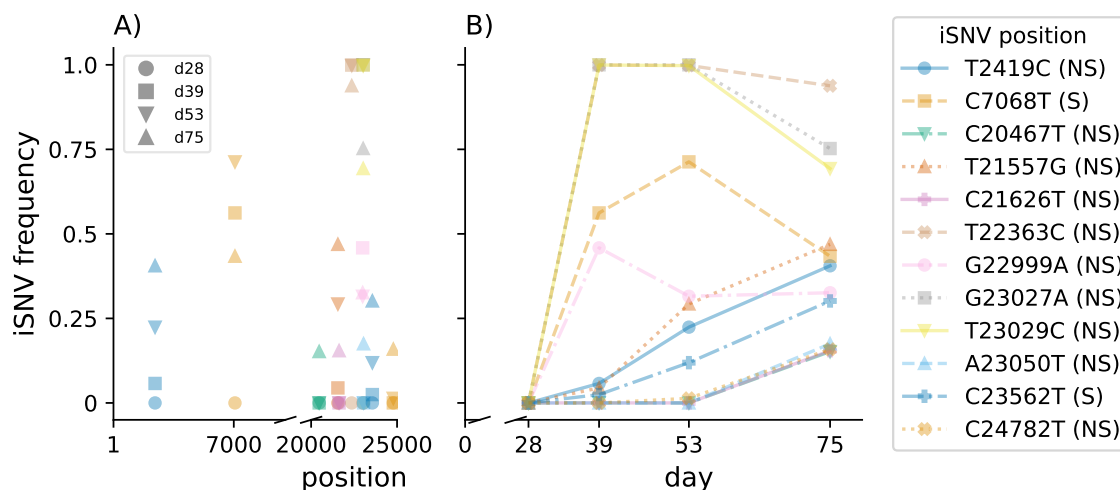
Figure 5.3: iSNV frequencies were inferred using LoFreq, and high frequency iSNVs are largely clustered in the spike protein, and frequency dynamics over time are shown. **(A)** The frequencies of iSNVs called from merged libraries and reach at least a 10% frequency during the infection are presented along their position in the genome. Different shapes are used to denote which day the iSNV was observed. **(B)** iSNV dynamics over time where each iSNV has a unique color, marker, and line style. The colors used for each iSNV coordinate with those seen in (A). The nucleotide changes were annotated using Nextclade (Aksamentov et al., 2021) as follows: 2419: S723P; 7068: synonymous; 20467: S2338L; 21557: V3G; 21626: P26L; 22363: S272P; 22999: E484K; 23027: Q493R; 23029: S494P; 23050: N501Y; 23562: synonymous; 24782: A1078V. Nucleotide identities are shown in the legend such that the letter preceding the locus is the d28 consensus nucleotide, while the letter following the locus is the observed variant nucleotide. Nonsynonymous (NS) and synonymous (S) amino acid changes are indicated in parentheses.

each differ from the d28 GGTA haplotype by 2-3 nucleotides (for GACA, at sites 23027 and 23029; for AACA, at sites 22999, 23027, and 23029). One explanation for these observed dynamics is that the G→A mutation at site 23027 and the T→C mutation at site 23029 fixed shortly following d28, and that a third mutation (G→A at site 22999) arose thereafter, and rose in frequency until d39. From d39 to 53, GACA and AACA remain the only two haplotypes in circulation, with GACA increasing in frequency and AACA decreasing. It is possible that the GACA and AACA haplotypes were more fit under the selection regime imposed by the two courses of remdesivir treatment (Fig. 5.1A), while GGTA is postulated to have been more fit under mAb treatment. This is evidenced by the sera from this patient sampled between days 33

and 77 being unable to neutralize virus containing mutations that were fixed by d28 (Scherer et al., 2022)

	d28	d39	d53	d75
AACA	2 (0.001)	1799 (0.46)	625 (0.327)	1772 (0.265)
AACT	0	4 (0.001)	1 (0.001)	1 (0.0)
AATA	0	0	0	425 (0.064)
AATT	0	0	0	0
AGCA	0	0	0	0
AGCT	0	0	0	0
AGTA	0	1 (0.0)	0	0
AGTT	0	0	0	0
GACA	1 (0.001)	1934 (0.495)	1247 (0.653)	2732 (0.409)
GACT	0	5 (0.001)	2 (0.001)	3 (0.0)
GATA	1 (0.001)	0	2 (0.001)	3 (0.0)
GATT	0	0	0	2 (0.0)
GGCA	0	0	0	2 (0.0)
GGCT	0	0	0	1 (0.0)
GGTA	1800 (0.97)	0	0	461 (0.069)
GGTT	2 (0.001)	0	0	1155 (0.173)

Table 5.1: Observed haplotypes among sites 22999, 23027, 23029, and 23050 on sequenced reads for each sample. For reads that span the four sites, we count the occurrence of each possible haplotype, of which there are sixteen. Counts are shown here, with the calculated frequency rounded to the nearest thousandth in parentheses.

Finally, two new haplotypes arise between d53 and d75, as well as the return of the GGTA haplotype observed at d28 (Table 5.1, Fig. 5.4A). The GGTT haplotype is only one mutation away from GGTA, while it is two and three mutations away from the two dominant haplotypes on d39 and d53 (GACA and AACA, respectively). In contrast, the other new haplotype on d75, AATA, is two mutations away from GGTA and GACA, and only one mutation away from AACA. The most parsimonious explanation for the emergence of GGTT and AATA on d75 is that GGTT is a direct descendant from the wild-type GGTA while AATA is a descendant from AACA.

However, it is curious that both the wild-type would return after being undetected for nearly 50 days. For this reason, we investigated the possibility of re-infection explaining the influx of haplotypes on d75 (GGTA, GGTT, and AATA).

Above, we presented SARS-CoV-2 variants circulating at the population level in Georgia, focusing on the early phase of the infection and consensus-level differences. However, we now want to determine whether the patient was re-infected by a virus circulating during the latter portion of the infection. To do this, haplotypes can be useful. Recall that the dominant haplotypes circulating during the infection are GATA and GATT (Fig. 5.2A). Two of the three haplotypes that arise in the patient on d75, GGTA and GGTT, are both one mutation away from GATA and GATT, respectively. Were we to only focus on iSNVs, we would note that 23029T is absent in the host on d53, but at very high frequency at the population level, and is the common nucleotide between the invading d75 haplotypes, GGTA, GGTT, and AATA. This may lead us to conclude that a virus with 23029T re-infected the host. Further, two of these haplotypes have the 23027G variant, which is not circulating in the population, apart from the patient sequence from d28. To produce a 23027G with 23029T haplotype via recombination between a re-infecting virus and an existing AACA or GACA haplotype would be highly improbable since they are only two nucleotides away from one another. Alternatively, back-mutation at these same sites after re-infecting the host is another explanation with no observable evidence. Thus, it is unlikely that re-infection can explain the arrival of the closely related GGTT and GGTA haplotypes within our host since we would expect the middle two sites to be linked and their combination is not observed in the population, despite one of the loci being nearly fixed at the population level. We return to the most parsimonious explanation, which is that GGTA was circulating below our limit of detection – or in some reservoir tissue – and gave rise to the GGTT haplotype, while AATA descended from the high-frequency AACA haplotype. We cannot rule out that AATA was

the result of a re-infection since it was observed at the population level, but it was circulating at very low frequencies.

Clearly a combination of haplotype and iSNV analysis can give us more information to discern evolutionary patterns, so we now consider iSNV dynamics in concert with our observed haplotypes to infer finer resolution haplotypes within the host (Fig. 5.4B).

Between d28 and d39, three iSNVs reach fixation, and two of them (23027A and 23029C) are a part of observable haplotypes. The other is 22363C. It is difficult at this point to discern what order the mutations fixed, but it may be possible that 23027A and 23029C were a part of a single multi-mutation event since they are so close together. For now we assume 22363C fixed first. Following these fixation events, 7068T and 22999A reach approximately 50% frequency, with 7068T having slightly higher frequency.

In the following time point, d53, the frequency of 22999A goes down while 7068T goes up in frequency, along with the rise of several other iSNVs at other loci. It is unlikely that iSNVs on that same background would rise and fall in frequency concurrently, so we can infer that the variants at site 7068 and 22999 are on different haplotypes. Similar arguments can follow for sites 2419 and 21557, where their very similar iSNV frequencies from d39 to d53 rise while 22999 falls. For this reason, variants at sites 2419 and 21557 likely evolved after 7068, but on the same background. That background would have been GACA since 22999A is part of the AACA observed haplotype. The variant at site 23562 may have also evolved on this new background with 2419C and 21577G since it follows along the same trajectory but at a lower frequency.

Finally, the two new observed haplotypes, GGTT and AATA, arise between d53 and d75, with the return of the wild-type haplotype GGTA. Along with the rise of these haplotype frequencies is a continued rise in frequency of the remaining iSNVs at

(a)

(b)
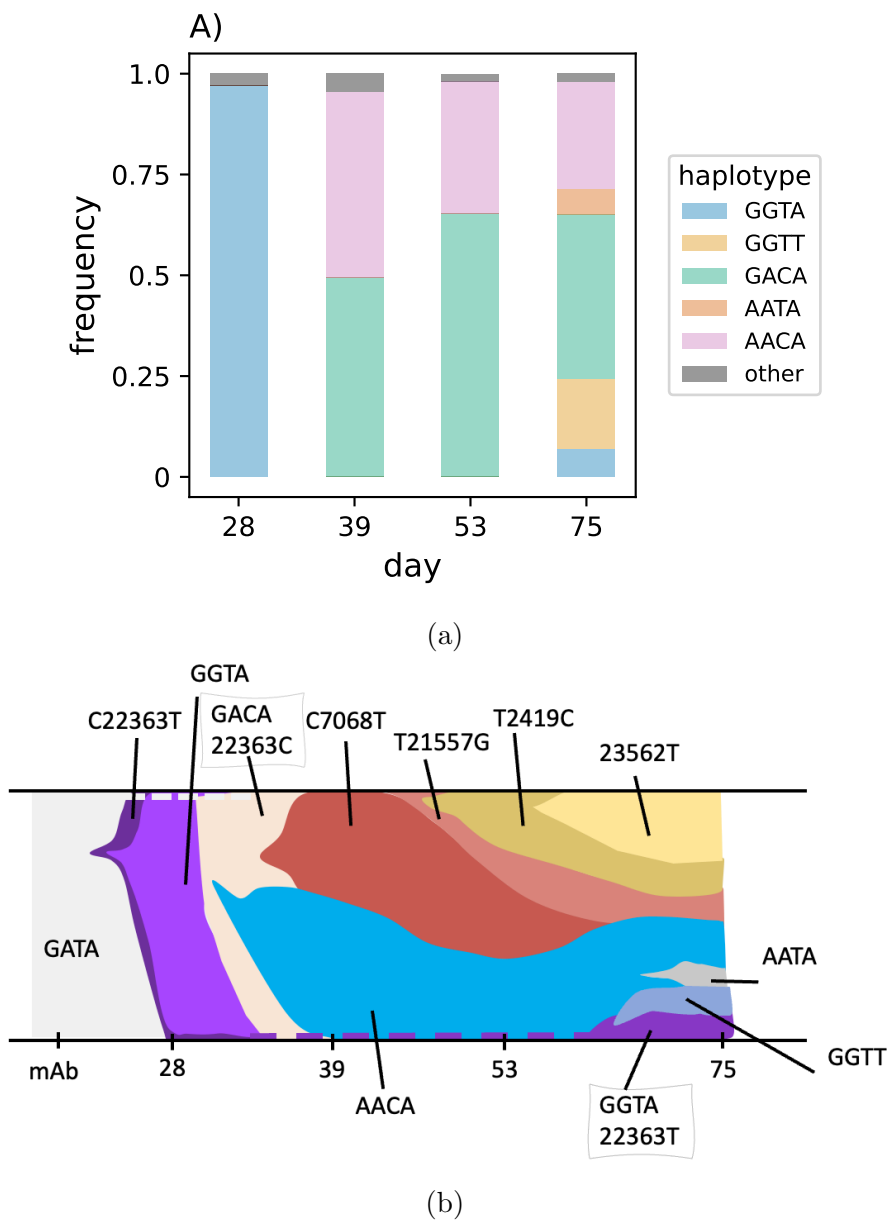
Figure 5.4: Observed and inferred haplotype frequencies. **(A)** Physical haplotypes observed from short-read data (Table 5.1) shows there are at least five haplotypes circulating within this patient during their infection. Here each color represents a different haplotype as indicated in the legend at sites 22999, 23027, 23029, 23050. The height that each color fills is the frequency of the corresponding haplotype. The "other" category was given by the haplotypes that fell below the limit of detection individually. **(B)** Inferred haplotypes were created by combining the observed haplotypes with iSNV frequency data. Different colors indicate different haplotypes. Pointed edges from left to right indicate what background the new haplotype evolved on. Dashed gray (top) and dark purple (bottom) lines show putative reservoirs from which the next haplotype evolves or re-emerges.

sites 2419, 20467, 21557, 21626, 23562, and 24782. Additionally, the fixed iSNVs at sites 23027 and 23029 decrease in frequency at the same magnitude as 7068. Simultaneously, the iSNV at site 23050 rises in frequency, defining the GGTT haplotype.

Since we established earlier that re-infection is an unlikely explanation for the arrival of the GGTT and AATA haplotypes, along with the return of GGTA (Fig. 5.2A), we propose an alternative explanation. Given that SARS-CoV-2 is capable of infecting many different tissues, the variant 22363T with the GGTA background may have sequestered in a reservoir tissue that was unsampled during the infection period and migrated back into the upper respiratory tract (Fig. 5.4B, purple dashed line). Meanwhile, while 22363C was fixing, we propose that GGTA was sequestered in a reservoir before returning to detectable frequencies by d75. It would have brought along with it the 22363T mutation and been a viable background for the evolution of the GGTT haplotype.

The rise in frequency of these unique iSNV and haplotype combinations may have been facilitated by the amount of time that remdesivir treatment had been halted. Earlier we suggested that GGTA was less fit than the two haplotypes that replaced it once remdesivir treatment commenced. Since there were 30 days between d75 and when the antiviral treatment had stopped, it is possible that GGTA was then able to invade from its reservoir. Alternatively, these genotype combinations were circulating in the sampled area but were simply below our limit of detection.

Further interpretation that considers the clinical course for this patient can provide more context for why selection may be responsible for iSNV dynamics. For example: monoclonal antibodies were administered early on in the infection and by 4 weeks later the population became relatively monomorphic from the strong selective force induced by treatment. However, low frequency variants were percolating. Remdesivir treatment was administered which induced competition among several existing haplotypes, one that remained relatively constant in frequency, and another

that spawned two additional haplotypes. We know that remdesivir can inhibit binding on the spike protein in the receptor binding domain (RBD) (Szemiel et al., 2021, Uddin et al., 2022), so it is possible that remdesivir treatment simultaneously selected for the AACA and GACA haplotypes because all of these sites are within the RBD. Continued selection from treatment may have targeted other loci, allowing them to rise in frequency. However, they would have been in competition with one another if they evolved on different haplotype backgrounds. This is evidenced by the rise in frequency of some haplotypes with concomitant changes in iSNV frequencies.

5.5   Discussion

Chronic SARS-CoV-2 infections may be important sources of new variants of concern, and thus be a driver of viral adaptation observed at the population level. Here we examined the evolutionary dynamics of iSNVs and haplotypes independently, and then considered their joint dynamics within a single immunocompromised patient. We found that iSNV analysis revealed the fixation of multiple nonsynonymous mutations in the spike region, with continued rises in frequency of additional nonsynonymous iSNVs throughout the infection. Haplotype analysis revealed that despite the fixation of multiple iSNVs, the population was likely not monomorphic at any point after the first treatment of remdesivir administered to the patient. The timing of remdesivir treatment with the appearance and disappearance of some haplotypes is suggestive of an altered selection environment while the patient underwent the anti-viral treatment. While iSNVs and consensus-level mutations compared to population-level sequences provide some evidence that re-infection was unlikely to explain new and recurrent iSNVs later on in the infection, haplotypes helped to confirm this, and further suggest that migration from a within-host reservoir explains the appearance and reappearance of iSNVs at low frequency.

As we have shown, even a simple haplotype analysis can be useful in interpreting the evolution of within-host variants. Others have used haplotypes to discern co-infection events (Francisco Junior et al., 2022, VanInsberghe et al., 2021, Wu et al., 2021), which singular iSNV data cannot do as reliably, particularly at low and intermediate frequencies. Haplotype reconstruction allowed us to identify whether re-infection was an explanation for the return of a genotype that had not been observed since much earlier on in the infection. Further, iSNVs occurring together makes it more challenging to attribute a narrative of selection acting on individual iSNVs. For example, the mutations we describe at sites 23027 and 23029 occur together almost exclusively and each confer nonsynonymous amino acid changes. For this reason, we cannot resolve the individual selective pressures on the two iSNVs, just the selective pressure on the pair. This is often a limitation of observational studies such as these (Scherer et al., 2022), because we must not only infer linkage among variants where linkage cannot be observed directly, but the iSNVs and their linked pairs may differ in their dynamics across hosts. So while we can make suggestive claims about the source of selection and its outcomes, further study is needed to parse out selective advantages of individual iSNVs.

While infection studies and immunological assays can assess the roles that treatments play on particular mutations (Guigon et al., 2022, Focosi et al., 2021), and some population studies can show us where mutations tend to recur (Lythgoe et al., 2021, van Dorp et al., 2020) comprehensive analysis of mutation combinations rather than individual mutations may present a higher resolution picture of the adaptive advantages among immunologically relevant variants across the SARS-CoV-2 genome.

Data Availability

The code used to reproduce the analysis shown in this paper is available at `https://github.com/allmanbrent/SARS-CoV-2-haplotypes/settings`. The data from the patient are attributed to Scherer et al. (2022).

Acknowledgments

Funding

Conflicts of Interest

The authors report no conflicts of interest.

Chapter 6

Conclusion

To conclude, we have presented multiple vignettes of within-host evolution of RNA viruses, each contributing to our understanding of viral adaptation which has implications for their pandemic potential. Two major themes have emerged from our work: (i) cellular coinfection can reduce the efficacy of selection on mutations, and (ii) genetic linkage reduces the efficacy of selection on single mutations, but provides additional information about evolutionary dynamics that individual mutations cannot.

In Chapter 2, we explored the role that heterogeneity plays in deleterious mutation accumulation in the context of cellular coinfection. While previous work has shown that cellular coinfection can reduce the efficacy of selection on individual mutations (Wilke and Novella, 2003b), our work also incorporates an infinite sites model where many mutations contribute to viral fitness. As such, we are able to show that genetic linkage leads to the accumulation of deleterious mutations, particularly when selection is relaxed due to phenotypic hiding or reduced effective population sizes. However, deleterious mutation accumulation can be mitigated when viral genomes are segmented. Viral sex through recombination or reassortment reduces selection interference between sites by creating progeny that aren't clonal; beneficial mutations

on different backgrounds can be brought together. In our study, this simply meant that genes with fewer deleterious mutations can be inherited together if the the viral parents coinfect the same cell.

We also extended our understanding of phenotypic hiding and the efficacy of selection by fitting model parameters to allele frequency data. In Chapter 3, we developed a model that described the frequency trajectory of a viral variant in a Wright-Fisher population where cellular coinfection was possible. We showed the utility of considering phenotypic hiding, since we concluded that fitness estimation within hosts that does not consider cellular coinfection is likely underestimating the magnitude of variant fitness. While our model needed a strong prior on MOI to get a bounded range of variant fitness values, these data are available in many *in vivo* systems and would almost always be available in *in vitro* settings.

Taken together, Chapters 2 and 3 contribute to the growing literature on sociovirology because they consider the consequences of viruses of differing genotypes interacting through coinfection, and the unique impacts these interactions can have on viral progeny fitness. However, Chapter 2 also included considerations of genetic linkage, which we demonstrated as being important for discerning selection and gene flow in Chapters 4 and 5.

When censusing the diversity of within host viral populations, identifying mutations that are driving evolutionary dynamics can be a challenge. In Chapter 4, experiments were conducted to show that SARS-CoV-2 mutations that rose in frequency after monoclonal antibody treatment did in fact confer a fitness advantage by escaping immune pressure. In Chapter 5, haplotypes were utilized to help discern whether mutations may be favored by selection or arising through gene flow, confounding inference on selective pressures. Each of these works used secondary analyses on the same data to better inform adaptationist narratives of SARS-CoV-2 evolution within immunocompromised hosts.

Future work in these areas should consider the role that spatial structure and population dynamics have in the evolution of viral variants within hosts. In particular, if we want to further understand how cellular coinfection and phenotypic hiding can relax selection, population expansion through space will be crucial for modeling realistic evolutionary dynamics. The dispersion kernel associated with spread will also be a key consideration. Viral populations that spread through small jumps in space are more likely to encounter high MOI contexts. So under our model assumptions, relaxed selection would be most prevalent if there was strong spatial structure within viral hosts. However, others have suggested that coinfection can be beneficial for viral fitness and diversity (Leeks et al., 2018). Additionally, we know that coinfection can provide benefits such as genetic complementation for incomplete viral genomes, increased production of viral progeny, and providing opportunities for reassortment or recombination. The vast possibilities of interactions among these differing forces provides rich lines of questioning from both experimentalists and modelers.

Bibliography

A. F. Agrawal and M. C. Whitlock. Mutation load: the fitness of individuals in populations where deleterious alleles are abundant. *Annual Review of Ecology, Evolution, and Systematics*, 43:115–135, 2012.

E. R. Aguilera and J. K. Pfeiffer. Strength in numbers: Mechanisms of viral co-infection. *Virus Research*, 2019.

I. Aksamentov, C. Roemer, E. Hodcroft, and R. Neher. Nextclade: clade assignment, mutation calling and quality control for viral genomes. *Journal of Open Source Software*, 6(67):3773, 2021.

M. Amicone, V. Borges, M. J. Alves, J. Isidro, L. Zé-Zé, S. Duarte, L. Vieira, R. Guiomar, J. P. Gomes, and I. Gordo. Mutation rate of SARS-CoV-2 and emergence of mutators during experimental evolution. *Evolution, Medicine, and Public Health*, 10(1):142–155, 2022.

J. P. Anderson, R. Daifuku, and L. A. Loeb. Viral error catastrophe by mutagenic nucleosides. *Annu. Rev. Microbiol.*, 58:183–205, 2004.

R. Andino and E. Domingo. Viral quasispecies. *Virology*, 479:46–51, 2015.

I. Andreu-Moreno and R. Sanjuán. Collective infection of cells by viral aggregates promotes early viral proliferation and reveals a cellular-level allee effect. *Current Biology*, 28(20):3212–3219, 2018.

P. Baccam, C. Beauchemin, C. A. Macken, F. G. Hayden, and A. S. Perelson. Kinetics of Influenza A virus infection in humans. *Journal of Virology*, 80(15):7590–7599, 2006.

C. Bank, N. Renzette, P. Liu, S. Matuszewski, H. Shim, M. Foll, D. N. Bolon, K. B. Zeldovich, T. F. Kowalik, R. W. Finberg, et al. An experimental evaluation of drug-induced mutational meltdown as an antiviral treatment strategy. *Evolution*, 70(11):2470–2484, 2016.

N. H. Barton and S. P. Otto. Evolution of recombination due to random drift. *Genetics*, 169(4):2353–2370, 2005.

G. Bell. Recombination and the immortality of the germ line. *Journal of Evolutionary Biology*, 1(1):67–82, 1988.

A. V. Bordería, O. Isakov, G. Moratorio, R. Henningsson, S. Agüera-González, L. Organtini, N. F. Gnädig, H. Blanc, A. Alcover, S. Hafenstein, et al. Group selection and contribution of minority variants during virus adaptation determines virus fitness and phenotype. *PLoS Pathogens*, 11(5):e1004838, 2015.

K. M. Braun, G. K. Moreno, C. Wagner, M. A. Accola, W. M. Rehrauer, D. A. Baker, K. Koelle, D. H. O'Connor, T. Bedford, T. C. Friedrich, et al. Acute SARS-CoV-2 infections harbor limited within-host diversity and transmit via tight transmission bottlenecks. *PLoS pathogens*, 17(8):e1009849, 2021.

C. B. Brooke, W. L. Ince, J. Wrammert, R. Ahmed, P. C. Wilson, J. R. Bennink, and J. W. Yewdell. Most Influenza A virions fail to express at least one essential viral protein. *Journal of Virology*, 87(6):3155–3162, 2013.

L. Chao. Fitness of RNA virus decreased by Muller's ratchet. *Nature*, 348(6300):454, 1990.

L. Chao, T. T. Tran, and T. T. Tran. The advantage of sex in the RNA virus $\varphi 6$. *Genetics*, 147(3):953–959, 1997.

D. Charlesworth, M. Morgan, and B. Charlesworth. Mutation accumulation in finite outbreeding and inbreeding populations. *Genetics Research*, 61(1):39–56, 1993.

P. P. Cheung, S. J. Watson, K.-T. Choy, S. F. Sia, D. D. Wong, L. L. Poon, P. Kellam, Y. Guan, J. M. Peiris, and H.-L. Yen. Generation and characterization of Influenza A viruses with altered polymerase fidelity. *Nature Communications*, 5:4794, 2014.

D. K. Clarke, E. A. Duarte, A. Moya, S. F. Elena, E. Domingo, and J. Holland. Genetic bottlenecks and population passages cause profound fitness differences in RNA viruses. *Journal of Virology*, 67(1):222–228, 1993.

L. L. Coffey, Y. Beeharry, A. V. Bordería, H. Blanc, and M. Vignuzzi. Arbovirus high fidelity variant loses fitness in mosquitoes and mice. *Proceedings of the National Academy of Sciences*, 108(38):16038–16043, 2011.

E. Cohen, D. A. Kessler, and H. Levine. Analytic approach to the evolutionary effects of genetic exchange. *Physical Review E*, 73(1):016113, 2006.

J. F. Crow. Some possibilities for measuring selection intensities in man. *Human Biology*, 30(1):1–13, 1958.

J. Damas, G. M. Hughes, K. C. Keough, C. A. Painter, N. S. Persky, M. Corbo, M. Hiller, K.-P. Koepfli, A. R. Pfenning, H. Zhao, D. P. Genereux, R. Swofford, K. S. Pollard, O. A. Ryder, M. T. Nweeia, K. Lindblad-Toh, E. C. Teeling, E. K. Karlsson, and H. A. Lewin. Broad host range of SARS-CoV-2 predicted by comparative and structural analysis of ACE2 in vertebrates. *Proceedings of the National Academy of Sciences*, 117(36):22311–22322, 2020.

S. L. Díaz-Muñoz, R. Sanjuán, and S. West. Sociovirology: conflict, cooperation, and communication among viruses. *Cell Host & Microbe*, 22(4):437–441, 2017.

S. F. Elena, M. Davila, I. S. Novella, J. J. Holland, E. Domingo, and A. Moya. Evolutionary dynamics of fitness recovery from the debilitating effects of Muller's ratchet. *Evolution*, 52(2):309–314, 1998.

C. Escarmís, M. Dávila, N. Charpentier, A. Bracho, A. Moya, and E. Domingo. Genetic lesions associated with Muller's ratchet in an RNA virus. *Journal of Molecular Biology*, 264(2):255–267, 1996.

W. Ewens. On the concept of the effective population size. *Theoretical Population Biology*, 21(3):373–378, 1982.

R. Fisher. The genetical theory of natural selection, 1930.

D. Focosi, F. Novazzi, A. Genoni, F. Dentali, D. D. Gasperina, A. Baj, and F. Maggi. Emergence of SARS-COV-2 Spike Protein Escape Mutation Q493R after Treatment for COVID-19. *Emerging Infectious Diseases*, 27(10):2728–2731, 2021.

S. Y. Folimonova. Superinfection exclusion is an active virus-controlled function that requires a specific viral protein. *Journal of Virology*, 86(10):5554–5561, 2012.

R. d. S. Francisco Junior, L. G. P. d. Almeida, A. P. Lamarca, L. Cavalcante, Y. Martins, A. L. Gerber, A. P. d. C. Guimarães, R. B. Salviano, F. L. dos Santos, T. H. de Oliveira, I. V. de Souza, E. M. de Carvalho, M. S. Ribeiro, S. Carvalho, F. D. da Silva, M. H. d. O. Garcia, L. M. de Souza, C. G. da Silva, C. L. P. Ribeiro, A. C. Cavalcanti, C. M. B. de Mello, A. Tanuri, and A. T. R. Vasconcelos. Emergence of Within-Host SARS-CoV-2 Recombinant Genome After Coinfection by Gamma and Delta Variants: A Case Report. *Frontiers in Public Health*, 10:849978, 2022.

R. Froissart, C. O. Wilke, R. Montville, S. K. Remold, L. Chao, and P. E. Turner. Co-infection weakens selection against epistatic mutations in RNA viruses. *Genetics*, 168(1):9–19, 2004.

W. H. Frost. Statistics of Influenza Morbidity: With Special Reference to Certain Factors in Case Incidence and Case Fatality. *Public Health Reports (1896-1970)*, 35(11):584, 1920.

M. E. Gallagher, C. B. Brooke, R. Ke, and K. Koelle. Causes and consequences of spatial within-host viral spread. *Viruses*, 10(11):627, 2018.

J. García-Arriaza, E. Domingo, and C. Escarmís. A segmented form of foot-and-mouth disease virus interferes with standard virus: a link between interference and competitive fitness. *Virology*, 335(2):155–164, 2005.

E. Gazave, D. Chang, A. G. Clark, and A. Keinan. Population growth inflates the per-individual number of deleterious mutations and reduces their mean effect. *Genetics*, 195(3):969–978, 2013.

M. Ghafari, C. K. Lumby, D. B. Weissman, and C. J. Illingworth. Inferring transmission bottleneck size from viral sequence data using a novel haplotype reconstruction method. *Journal of Virology*, 94(13):e00014–20, 2020.

M. Ghafari, Q. Liu, A. Dhillon, A. Katzourakis, and D. B. Weissman. Investigating the evolutionary origins of the first three SARS-CoV-2 variants of concern. *bioRxiv*, 2022. doi: 10.1101/2022.05.09.491227.

M. Golumbeanu, S. Cristinelli, S. Rato, M. Munoz, M. Cavassini, N. Beerenwinkel, and A. Ciuffi. Single-cell rna-seq reveals transcriptional heterogeneity in latent and reactivated hiv-infected cells. *Cell Reports*, 23(4):942–950, 2018.

I. Gordo and B. Charlesworth. The degeneration of asexual haploid populations and the speed of Muller's ratchet. *Genetics*, 154(3):1379–1387, 2000.

A. Guigon, E. Faure, C. Lemaire, M.-C. Chopin, C. Tinez, A. Assaf, M. Lazrek, D. Hober, L. Bocket, I. Engelmann, and E. K. Alidjinou. Emergence of Q493R mutation in SARS-CoV-2 spike protein during bamlanivimab/etesevimab treatment and resistance to viral clearance. *Journal of Infection*, 84(2):248–288, 2022.

J. Haigh. The accumulation of deleterious genes in a population—Muller's ratchet. *Theoretical Population Biology*, 14(2):251–267, 1978.

F. S. Heldt, S. Y. Kupke, S. Dorl, U. Reichl, and T. Frensing. Single-cell analysis and stochastic modelling unveil large cell-to-cell variability in Influenza A virus infection. *Nature Communications*, 6:8938, 2015.

M. G. Hossain, A. Javed, S. Akter, and S. Saha. SARS-CoV-2 host diversity: An update of natural infections and experimental evidence. *Journal of Microbiology, Immunology and Infection*, 54(2):175–181, 2021.

N. P. A. S. Johnson and J. Mueller. Updating the Accounts: Global Mortality of the 1918-1920 "Spanish" Influenza Pandemic. *Bulletin of the History of Medicine*, 76(1):105–115, 2002.

M. Kimura, T. Maruyama, and J. F. Crow. The mutation load in small populations. *Genetics*, 48(10):1303, 1963.

A. Leeks, E. A. Segredo-Otero, R. Sanjuán, and S. A. West. Beneficial coinfection can promote within-host viral diversity. *Virus Evolution*, 4(2), 2018.

S. Leviyang and I. Griva. Investigating Functional Roles for Positive Feedback and Cellular Heterogeneity in the Type I Interferon Response to Viral Infection. *Viruses*, 10(10):517, 2018.

J. O. Lloyd-Smith, S. J. Schreiber, P. E. Kopp, and W. M. Getz. Superspreading and the effect of individual variation on disease emergence. *Nature*, 438(7066):355, 2005.

M. Lynch, J. Conery, and R. Burger. Mutation accumulation and the extinction of small populations. *The American Naturalist*, 146(4):489–518, 1995.

K. A. Lythgoe, M. Hall, L. Ferretti, M. de Cesare, G. MacIntyre-Cockett, A. Trebes, M. Andersson, N. Otecko, E. L. Wise, N. Moore, et al. SARS-CoV-2 within-host diversity and transmission. *Science*, 372(6539):eabg0821, 2021.

L. Manuto, M. Grazioli, A. Spitaleri, P. Fontana, L. Bianco, L. Bertolotti, M. Bado, G. Mazzotti, F. Bianca, F. Onelia, G. Lorenzin, F. Simeoni, D. Lazarevic, E. Franchin, C. D. Vecchio, I. Dorigatti, G. Tonon, D. M. Cirillo, E. Lavezzo, A. Crisanti, and S. Toppo. Rapid SARS-CoV-2 Intra-Host and Within-Household Emergence of Novel Haplotypes. *Viruses*, 14(2):399, 2022.

B. E. Martin, J. D. Harris, J. Sun, K. Koelle, and C. B. Brooke. Cellular co-infection can modulate the efficiency of Influenza A virus production and shape the interferon response. *PLoS Pathogens*, 16(10):e1008974, 2020.

M. A. Martin and K. Koelle. Comment on "genomic epidemiology of superspreading events in Austria reveals mutational dynamics and transmission properties of SARS-CoV-2". *Science Translational Medicine*, 13(617):eabh1803, 2021.

Y. Michalakis and S. Blanc. The Curious Strategy of Multipartite Viruses. *Annual Review of Virology*, 7(1):203–218, 2020.

H. J. Muller. The relation of recombination to mutational advance. *Mutation Research/Fundamental and Molecular Mechanisms of Mutagenesis*, 1(1):2–9, 1964.

I. S. Novella, D. D. Reissig, and C. O. Wilke. Density-dependent selection in vesicular stomatitis virus. *Journal of Virology*, 78(11):5799–5804, 2004.

M. D. Pauly and A. S. Lauring. Effective lethal mutagenesis of influenza virus by three nucleoside analogs. *Journal of Virology*, 89(7):3584–3597, 2015.

J. K. Pfeiffer and K. Kirkegaard. A single mutation in poliovirus RNA-dependent RNA polymerase confers resistance to mutagenic nucleotide analogs via increased fidelity. *Proceedings of the National Academy of Sciences*, 100(12):7289–7294, 2003.

K. L. Phipps, K. Ganti, N. T. Jacobs, C.-Y. Lee, S. Carnaccini, M. C. White, M. Manandhar, B. E. Pickett, G. S. Tan, L. M. Ferreri, et al. Collective interactions augment Influenza A virus replication in a host-dependent manner. *Nature Microbiology*, 5(9):1158–1169, 2020.

A. Poon and L. Chao. Drift increases the advantage of sex in RNA bacteriophage φ6. *Genetics*, 166(1):19–24, 2004.

A. Popa, J.-W. Genger, M. D. Nicholson, T. Penz, D. Schmid, S. W. Aberle, B. Agerer, A. Lercher, L. Endler, H. Colaço, et al. Genomic epidemiology of superspreading events in austria reveals mutational dynamics and transmission properties of SARS-CoV-2. *Science Translational Medicine*, 12(573):eabe2555, 2020.

A. H. Reid, J. K. Taubenberger, and T. G. Fanning. Evidence of an absence: the genetic origins of the 1918 pandemic influenza virus. *Nature Reviews Microbiology*, 2(11):909–914, 2004.

A. B. Russell, C. Trapnell, and J. D. Bloom. Extreme heterogeneity of influenza virus infection in single cells. *eLife*, 7:e32303, 2018.

J. E. San, S. Ngcapu, A. M. Kanzi, H. Tegally, V. Fonseca, J. Giandhari, E. Wilkinson, C. W. Nelson, W. Smidt, A. M. Kiran, et al. Transmission dynamics of SARS-CoV-

2 within-host diversity in two major hospital outbreaks in South Africa. *Virus Evolution*, 7(1):veab041, 2021.

R. Sanjuán. Collective infectious units in viruses. *Trends in Microbiology*, 25(5): 402–412, 2017.

R. Sanjuán, A. Moya, and S. F. Elena. The distribution of fitness effects caused by single-nucleotide substitutions in an RNA virus. *Proceedings of the National Academy of Sciences*, 101(22):8396–8401, 2004.

R. Sanjuán, M. R. Nebot, N. Chirico, L. M. Mansky, and R. Belshaw. Viral Mutation Rates. *Journal of Virology*, 84(19):9733, 2010.

T. Schaller, N. Appel, G. Koutsoudakis, S. Kallis, V. Lohmann, T. Pietschmann, and R. Bartenschlager. Analysis of hepatitis C virus superinfection exclusion by using novel fluorochrome gene-tagged viral genomes. *Journal of Virology*, 81(9): 4591–4603, 2007.

E. M. Scherer, A. Babiker, M. W. Adelman, B. Allman, A. Key, J. M. Kleinhenz, R. M. Langsjoen, P.-V. Nguyen, I. Onyechi, J. D. Sherman, T. W. Simon, H. Soloff, J. Tarabay, J. Varkey, A. S. Webster, D. Weiskopf, D. B. Weissman, Y. Xu, J. J. Waggoner, K. Koelle, N. Rouphael, S. M. Pouch, and A. Piantadosi. SARS-CoV-2 Evolution and Immune Escape in Immunocompromised Patients. *New England Journal of Medicine*, 2022.

M. B. Schulte and R. Andino. Single-cell analysis uncovers extensive biological noise in poliovirus replication. *Journal of Virology*, 88(11):6205–6212, 2014.

T. Sekizuka, K. Itokawa, T. Kageyama, S. Saito, I. Takayama, H. Asanuma, N. Nao, R. Tanaka, M. Hashino, T. Takahashi, et al. Haplotype networks of SARS-CoV-2 infections in the diamond princess cruise ship outbreak. *Proceedings of the National Academy of Sciences*, 117(33):20198–20201, 2020.

J. D. Siqueira, L. R. Goes, B. M. Alves, P. S. d. Carvalho, C. Cicala, J. Arthos, J. P. Viola, A. C. De Melo, and M. A. Soares. SARS-CoV-2 genomic analyses in cancer patients reveal elevated intrahost genetic diversity. *Virus Evolution*, 7(1):veab013, 2021.

G. J. D. Smith, D. Vijaykrishna, J. Bahl, S. J. Lycett, M. Worobey, O. G. Pybus, S. K. Ma, C. L. Cheung, J. Raghwani, S. Bhatt, J. S. M. Peiris, Y. Guan, and A. Rambaut. Origins and evolutionary genomics of the 2009 swine-origin H1N1 influenza A epidemic. *Nature*, 459(7250):1122–1125, 2009.

J. Sun and C. B. Brooke. Influenza A virus superinfection potential is regulated by viral genomic heterogeneity. *MBio*, 9(5):e01761–18, 2018.

J. Sun, J. C. Vera, J. Drnevich, Y. T. Lin, R. Ke, and C. B. Brooke. Single cell heterogeneity in Influenza A virus gene expression shapes the innate antiviral response to infection. *PLoS Pathogens*, 16(7):e1008671, 2020.

A. M. Szemiel, A. Merits, R. J. Orton, O. A. MacLean, R. M. Pinto, A. Wickenhagen, G. Lieber, M. L. Turnbull, S. Wang, W. Furnon, N. M. Suarez, D. Mair, A. da Silva Filipe, B. J. Willett, S. J. Wilson, A. H. Patel, E. C. Thomson, M. Palmarini, A. Kohl, and M. E. Stewart. In vitro selection of Remdesivir resistance suggests evolutionary predictability of SARS-CoV-2. *PLOS Pathogens*, 17 (9):e1009929, 2021.

N. S.-O. I. A. H. V. I. Team. Emergence of a novel swine-origin influenza A (H1N1) virus in humans. *New England Journal of Medicine*, 360(25):2605–2615, 2009.

G. Tonkin-Hill, I. Martincorena, R. Amato, A. R. Lawson, M. Gerstung, I. Johnston, D. K. Jackson, N. Park, S. V. Lensing, M. A. Quail, et al. Patterns of within-host genetic diversity in SARS-CoV-2. *Elife*, 10:e66857, 2021.

P. E. Turner. Searching for the advantages of virus sex. *Origins of Life and Evolution of the Biosphere*, 33(1):95–108, 2003.

P. E. Turner, C. L. Burch, K. A. Hanley, and L. Chao. Hybrid frequencies confirm limit to coinfection in the RNA bacteriophage φ6. *Journal of Virology*, 73(3): 2420–2424, 1999.

M. B. Uddin, E. H. Sajib, S. F. Hoque, M. N. I. Bappy, F. Elahi, A. Ghosh, S. Muhit, M. M. Hassan, M. Hasan, R. Chelliah, S. J. Park, T. J. Mony, D.-H. Oh, and S. S. U. Ahmed. Genomic diversity and molecular dynamics interaction on mutational variances among RB domains of SARS-CoV-2 interplay drug inactivation. *Infection, Genetics and Evolution*, 97:105128, 2022.

A. L. Valesano, K. E. Rumfelt, D. E. Dimcheff, C. N. Blair, W. J. Fitzsimmons, J. G. Petrie, E. T. Martin, and A. S. Lauring. Temporal dynamics of SARS-CoV-2 mutation accumulation within and across infected hosts. *PLoS Pathogens*, 17(4): e1009499, 2021.

L. van Dorp, M. Acman, D. Richard, L. P. Shaw, C. E. Ford, L. Ormond, C. J. Owen, J. Pang, C. C. Tan, F. A. Boshier, A. T. Ortiz, and F. Balloux. Emergence of genomic diversity and recurrent mutations in SARS-CoV-2. *Infection, Genetics and Evolution*, 83:104351, 2020.

D. VanInsberghe, A. S. Neish, A. C. Lowen, and K. Koelle. Recombinant SARS-CoV-2 Genomes Circulated at Low Levels Over The First Year of The Pandemic. *Virus Evolution*, page veab059, 2021.

M. Vignuzzi, J. K. Stone, J. J. Arnold, C. E. Cameron, and R. Andino. Quasispecies diversity determines pathogenesis through cooperative interactions in a viral population. *Nature*, 439(7074):344, 2006.

Y. Wang, D. Wang, L. Zhang, W. Sun, Z. Zhang, W. Chen, A. Zhu, Y. Huang, F. Xiao, J. Yao, et al. Intra-host variation and evolutionary dynamics of SARS-CoV-2 populations in covid-19 patients. *Genome Medicine*, 13(1):1–13, 2021.

C. O. Wilke and I. S. Novella. Phenotypic mixing and hiding may contribute to memory in viral quasispecies. *BMC Microbiology*, 3(1):11, 2003a.

C. O. Wilke and I. S. Novella. Phenotypic mixing and hiding may contribute to memory in viral quasispecies. *BMC Microbiology*, page 10, 2003b.

P. R. Wilker, J. M. Dinis, G. Starrett, M. Imai, M. Hatta, C. W. Nelson, D. H. O'Connor, A. L. Hughes, G. Neumann, Y. Kawaoka, and T. C. Friedrich. Selection on haemagglutinin imposes a bottleneck during mammalian transmission of reassortant H5N1 influenza viruses. *Nature Communications*, 4(1):2636, 2013.

A. Wilm, P. P. K. Aw, D. Bertrand, G. H. T. Yeo, S. H. Ong, C. H. Wong, C. C. Khor, R. Petric, M. L. Hibberd, and N. Nagarajan. LoFreq: a sequence-quality aware, ultra-sensitive variant caller for uncovering cell-population heterogeneity from high-throughput sequencing datasets. *Nucleic Acids Research*, 40(22):11189–11201, 2012.

W. World Health Organization. WHO Coronavirus (COVID-19) Dashboard, accessed 2022-06-02. URL `https://covid19.who.int`.

S. Wright. Evolution in mendelian populations. *Genetics*, 16(2):97, 1931.

L. Wu, Q. Chen, K. Liu, J. Wang, P. Han, Y. Zhang, Y. Hu, Y. Meng, X. Pan, C. Qiao, S. Tian, P. Du, H. Song, W. Shi, J. Qi, H.-W. Wang, J. Yan, G. F. Gao, and Q. Wang. Broad host range of SARS-CoV-2 and the molecular basis for SARS-CoV-2 binding to cat ACE2. *Cell Discovery*, 6(1):1–12, 2020.

Y. Wu, S. Zheng, T. Liu, X. Liu, H. Tang, Y. He, W. Xu, L. Li, W. Yu, K. Xing, and X. Xia. Viral Haplotypes in COVID-19 Patients Associated With Prolonged Viral Shedding. *Frontiers in Cellular and Infection Microbiology*, 11:715143, 2021.

X. Xin, H. Wang, L. Han, M. Wang, H. Fang, Y. Hao, J. Li, H. Zhang, C. Zheng, and C. Shen. Single-cell analysis of the impact of host cell heterogeneity on infection with foot-and-mouth disease virus. *Journal of Virology*, 92(9):e00179–18, 2018.

J. Zavada. Viral pseudotypes and phenotypic mixing. *Archives of Virology*, 50(1-2): 1–15, 1976.

H.-Y. Zhou, Y.-X. Cheng, L. Xu, J.-Y. Li, C.-Y. Tao, C.-Y. Ji, N. Han, R. Yang, Y. Li, and A. Wu. Genomic evidence for divergent co-infections of SARS-CoV-2 lineages. *medRxiv*, 2021.